

## Copyright Warning & Restrictions

The copyright law of the United States (Title 17, United States Code) governs the making of photocopies or other reproductions of copyrighted material.

Under certain conditions specified in the law, libraries and archives are authorized to furnish a photocopy or other reproduction. One of these specified conditions is that the photocopy or reproduction is not to be “used for any purpose other than private study, scholarship, or research.” If a user makes a request for, or later uses, a photocopy or reproduction for purposes in excess of “fair use” that user may be liable for copyright infringement,

This institution reserves the right to refuse to accept a copying order if, in its judgment, fulfillment of the order would involve violation of copyright law.

**Please Note: The author retains the copyright while the New Jersey Institute of Technology reserves the right to distribute this thesis or dissertation**

Printing note: If you do not wish to print this page, then select “Pages from: first page # to: last page #” on the print dialog screen



The Van Houten library has removed some of the personal information and all signatures from the approval page and biographical sketches of theses and dissertations in order to protect the identity of NJIT graduates and faculty.

## ABSTRACT

### UNDERSTANDING THE ORIGIN OF THE RECOVERY OF SUPERCONDUCTIVITY IN HALOGENATED YBCO SINGLE CRYSTAL: ATOMIC STRUCTURE STUDY

by

**Lamine Mohamed Kollakoye Dieng**

The recovery of superconductivity in underdoped  $\text{YBa}_2\text{Cu}_3\text{O}_{6+y}$  (YBCO) by exposure to bromine, iodine, chlorine and fluorine is a long-standing problem which has not been clearly resolved. The key question concerns the role of these halogens in the lattice. In order to shed light to this problem, we have performed multiple-edge x-ray absorption fine structure (XAFS) measurements about the Y  $K$ , Ba  $L_3$ , I  $L_3$ , Cu  $K$  and Br  $K$ -edges at room temperature on brominated (non-brominated) and iodinated (non-iodinated) YBCO single crystals. Our XAFS results at the Br  $K$  (brominated) and I  $L_3$  -edges (iodinated) reveal that bromine and iodine do not enter the perfect YBCO lattice.

However, the XAFS fitting results at the Br  $K$  and I  $L_3$ -edges reveal that Br and I do occupy the Cu(1) sites of the oxygen deficient YBCO in nanoclusters. From the polarized x-ray absorption near edge measurements (XANES) at the Cu  $K$ -edge, the nanoclusters were found to be randomly oriented with respect to the “host” crystal and with respect to the polarization vector.

**UNDERSTANDING THE ORIGIN OF THE RECOVERY OF  
SUPERCONDUCTIVITY IN HALOGENATED YBCO SINGLE CRYSTAL:  
ATOMIC STRUCTURE STUDY**

by  
**Lamine Mohamed Kollakoye Dieng**

**A Dissertation  
Submitted to the Faculty of the New Jersey Institute of Technology and  
Rutgers, The State University of New Jersey - Newark  
In Partial Fulfillment of the Requirements for the Degree of  
Doctor of Philosophy in Applied Physics**

**Federated Physics Department**

**May 2004**

**Copyright © 2004 by Lamine Mohamed Kollakoye Dieng**

**ALL RIGHTS RESERVED**

## APPROVAL PAGE

### UNDERSTANDING THE ORIGIN OF THE RECOVERY OF SUPERCONDUCTIVITY IN HALOGENATED YBCO SINGLE CRYSTAL: ATOMIC STRUCTURE STUDY

**Lamine Mohamed Kollakoye Dieng**

Dr. Trevor A. Tyson, Dissertation Advisor  
Professor, Department of Physics, NJIT

Date

Dr. Mark Croft, Committee Member  
Professor, Department of Physics and Astronomy, Rutgers University

Date

Dr. Daniel E. Murrhick, Committee Member  
Professor, Department of Physics, Rutgers University

Date

~~Dr.~~ John F. Federici, Committee Member  
Professor, Department of Physics, NJIT

Date

Dr. Anthony Fiory, Committee Member  
Research Professor, Department of Physics, NJIT and Lucent Technology

Date

## BIOGRAPHICAL SKETCH

**Author:** Lamine Mohamed Kollakoye Dieng  
**Degree:** Doctor of Philosophy  
**Date:** May 2004

### Undergraduate and Graduate Education:

- Doctor of Philosophy in Applied Physics, Federated Physics Department, New Jersey Institute of Technology, Newark, NJ, and Rutgers, The State University of New Jersey-Newark, Newark, NJ, 2004
- Masters of Arts in Physics  
City College of the City University of New York, NY, 1995
- B.S/M.S in Theoretical Physics and Mathematics  
Kharkov State University, Ukraine, 1992

**Major:** Applied Physics

### Publications and Presentations:

A.Yu. Ignatov, L. M. Dieng, T.A. Tyson, T. He and R. Cava, (2003). Observation of low symmetry crystal structure of superconducting  $\text{MgCNi}_3$  by Ni *K*-edge X-ray absorption measurements. *Physical Review B* 67, 064509.

L. M. Dieng, A. Yu. Ignatov, T.A. Tyson, M. Croft, F. Dogan, J. Woicick and J. Grow. (2002). Observation of changes in the atomic and electronic structure of YBaCuO single crystals accompanying bromination, *Phys. Rev. B* 66, 014508.

N. M. Ravindra, A. Fiory, L. M. Dieng (2002). Electronical and compositional properties of TaSi<sub>2</sub> films. *Journal of Electronic Materials* vol. 31, No 10.

L. M. Dieng, A. Yu. Ignatov, T. A. Tyson, M. Croft, W. Caliebe and S. Khalid, (2002). Local structure about the I atoms in iodinated YBCO single crystals determined by I *L*<sub>3</sub>-edge EXAFS. Brookhaven National Laboratory Activity Report.

T. A. Tyson, H. Woo and L. M. Dieng (1995-1999). Local electronic and structural studies of transition metal oxides, MHATT-CAT, Advanced Photon Source Activity Report.

L. M. Dieng, T. A. Tyson, M. Croft and Fatih Dogan. Recovery of superconductivity in brominated YBCO single crystals, Materials Research Society Meeting/1999, Boston, MA.

L. M. Dieng, T. A. Tyson, M. Croft and Fatih Dogan. XAS studies on brominated and chlorinated YBCO single crystals, American Physical Society Meeting/2001, Seattle, WA.

L. M. Dieng, A. Yu. Ignatov, T.A. Tyson, T. He and R. Cava. Lowering of symmetry of  $\text{MgCNi}_3$  at the Ni  $K$ -Edge, American Physical Society Meeting/2002, Indianapolis, IN.



**To my mother, Fatoumata Binta Diallo and to my father, Amadou Oury Dieng.  
Especially to my hard working mother who replaced my father for several good years and was able to provide for us without any expectations, when we needed help and assistance while my father was going through hardships. When I was a kid I always used to see my mother coming late about 2:30 am from her owned restaurant business. From about 2:30 to 5:00 am was her nap time and at about 6:00 am she is ready to work until the next day. God Bless her**

## ACKNOWLEDGMENT

I would like to recognize and thank my dissertation advisor Professor Trevor. A. Tyson for his help, assistance and good advice throughout the program. Also I would like to thank Professor Mark Croft who I will call my second advisor for his advice and participation in many useful suggestions. My thanks goes to my friend Dr. Alex Ignatov from whom I learnt a great deal of XAFS techniques “Cpocibo Bolshoe”

I would like to thank Professor Daniel Murnick, Professor John Federici, and Professor Anthony Fiory for accepting to be members of my committee and for their useful comments. From the NJIT Physics Department, my thanks goes to Professor Anthony Johnson for his warm words and to Mrs. Renee Crawley, Leslie Williams-Haynes for their assistance anytime I needed help. Also I would like to thank Professor Jolie Cizewski graduate director Physics and Astronomy Department, Rutgers University, Piscataway for helping me choose graduate courses, Professor Lev Ioffe Physics and Astronomy Department, Rutgers University, Piscataway for making Many Body Theory understandable. My gratitudes to Mrs. Kathy DiMeo Physics and Astronomy Department, Rutgers University, Piscataway, and to Mrs. Elizabeth Wheeler Physics Department, Rutgers University, Newark for their help and assistance.

From the graduate studies office at NJIT, I would like to thank Dr. Ronald Kane, Dean of Graduate Studies and his staff for their support and for being able to provide solid answers to all my academic related issues. I also thank Professor Cheikhna Sylla from the School of Management at NJIT and his family for their assistance and help. Thanks to Dr. Hyungje Woo and to Dr. Congwu Cui former fellow graduate students for useful discussions. At last I would like to thank my friend Mamadou Conte for his support.

## TABLE OF CONTENTS

Chapter	Page
1 INTRODUCTION .....	1
1.1 Discovery of Superconductivity and its Applications .....	1
1.1.1 Discovery of Superconductivity .....	1
1.1.2 Perfect Diamagnetism .....	1
1.1.3 Energy Gap .....	2
1.1.4 Isotope Effects .....	4
1.2 Applications of Superconductivity .....	10
1.2.1 Power Quality Conditioning in Factories .....	10
1.2.2 Magnetic Separation .....	10
1.2.3 Medical Applications .....	11
1.2.4 Levitation .....	11
2 HIGH TEMPERATURE COPPER-OXIDE SUPERCONDUCTORS .....	12
2.1 History of Copper-Oxide Superconductors .....	12
2.2 Properties of High Temperature Superconductors .....	18
2.2.1 Structure of High Temperature Superconductors .....	18
2.2.2 Perovskite Structure .....	19
2.3 Properties of $\text{YBCO}_{6+x}$ .....	21
2.3.1 Orthorhombic Structure of $\text{YBCO}_{6+x}$ .....	22
2.3.2 Tetragonal Structure of $\text{YBCO}_{6+x}$ .....	24

**TABLE OF CONTENTS**  
(Continued)

<b>Chapter</b>	<b>Page</b>
3 EFFECT OF DOPING OF YBCO SAMPLES AND STRUCTURAL ORDER ..	26
3.1 Chemical Doping of an Orthorhombic Superconducting or of an Insulating Non-Superconducting YBCO .....	26
3.1.1 Oxygen Doping of an Insulating Tetragonal YBCO System.....	26
3.1.2 Doping with Rare Earth and 3d Elements.....	26
3.1.3 Pr Doped Orthorhombic Superconducting YBCO (123) Samples .....	27
3.2 Photodoping Semiconducting YBCO Samples .....	29
3.3 Pressure Effects on Superconductivity .....	31
3.4 Effect of Defects on Superconductivity.....	32
3.5 Halogenation of YBCO samples.....	33
3.6 Influence of Local Structure on Superconductivity.....	34
3.6.1 Purpose of Studying Local Atomic Structure Using XAFS .....	34
3.6.2 Long Range Structural Anomalies (X-ray Diffraction).....	34
3.6.3 Short Range Structural Anomalies (XAFS).....	35
3.7 Other Type of Transport Measurements and Existence of Anisotropy in Superconducting YBCO Samples.....	38
4 THEORY OF SUPERCONDUCTIVITY.....	39
4.1 Background of Theory of Superconductivity .....	39
4.2 BCS Theory and Ground State Energy.....	40
4.3 Models of Superconductivity.....	48

**TABLE OF CONTENTS**  
**(Continued)**

<b>Chapter</b>	<b>Page</b>
4.3.1 Model I.....	48
4.3.2 Model II .....	50
4.3.3 Model III.....	54
4.3.4 Model IV .....	57
<b>5 X-RAY ABSORPTION FINE STRUCTURE (XAFS) SPECTROSCOPY .....</b>	<b>59</b>
5.1 Theory of XAFS .....	59
5.1.1 Theory of Extended X-ray Absorption Fine Structure (XAFS).....	59
5.1.2 Multiple Scattering Approximation.....	60
5.1.3 The Photoemission Cross Section and the Multiple-Scattering Function .....	67
5.2 XAFS Data Analysis.....	70
5.2.1 Normalization .....	71
5.2.2 Conversion to k-Space.....	72
5.2.3 Background Subtraction.....	73
5.2.4 Fourier Transform and Filtering .....	75
5.2.5 Fitting EXAFS Data.....	77
<b>6 X-RAY ABSORPTION FINE STRUCTURE SPECTROSCOPY OF HALOGENATED YBCO SINGLE CRYSTALS.....</b>	<b>79</b>
6.1 X-ray Absorption Fine Structure of Brominated (non-brominated) YBCO <sub>6+x</sub> (x~0.6) Single Crystals .....	79
6.1.1 Introduction.....	79

**TABLE OF CONTENTS**  
**(Continued)**

<b>Chapter</b>	<b>Page</b>
6.1.2 Experimental Procedure and Data Reduction .....	83
6.1.3 Experimental Results and Data Analysis.....	89
6.1.3.1 Br <i>K</i> -edge of the Brominated YBCO single Crystals .....	90
6.1.3.2 C-axis Polarized Cu <i>K</i> -edge EXAFS of Brominated (non-brominated) YBCO Single Crystals.....	97
6.1.3.3 Polarized Cu <i>K</i> -edge XANES for Brominated and Normal YBCO Single Crystals .....	102
6.1.3.4 Ba <i>L</i> <sub>3</sub> -edge XAFS of Brominated and Normal YBCO Single Crystals .....	105
6.1.3.5 Y <i>K</i> -edge XAFS of Brominated and Normal YBCO Single Crystals .....	107
6.2 Discussion.....	109
6.3 Conclusions.....	115
6.4 X-ray Absorption Fine Structure of Iodinated YBCO <sub>6+x</sub> ( <i>x</i> ~0.27) Single Crystals, Experimental Procedure and Data Reduction.....	117
6.5 Experimental Results and Data Analysis for Iodinated YBCO( <i>x</i> ~0.27) Single Crystals, I <i>L</i> <sub>3</sub> -edge of the Iodinated YBCO Single Crystal.....	119
6.6 Conclusions.....	121

**TABLE OF CONTENTS**  
**(Continued)**

<b>Chapter</b>	<b>Page</b>
7 SUMMARY AND PROPOSED FUTURE WORK.....	123
7.1 Summary of the Background of Superconductivity and of Copper-Oxide Based Superconductors.....	123
7.2 Summary of Doping and Structural Disorder in the YBCO Compound .....	126
7.3 Summary of Pressure and of Defect Effects on Superconductivity.....	127
7.4 Summary of Brominated (non-brominated) and Iodinated (non-iodinated) YBCO Single Crystals Using XAFS Spectroscopy.....	128
7.5 Future Work.....	129
References.....	131

## LIST OF TABLES

Table	Page
1.1 Few type I superconductors with their respective $T_C$ .....	7
1.2 Some type II superconductors listed with their respective descending $T_C$ .....	8
1.2 Some type II superconductors listed with their respective descending $T_C$ .....	9
2.1 A partial list of few HTSC compounds with their crystal structures and transition temperature greater than liquid nitrogen temperature, 77 K.....	16
2.1 A partial list of few HTSC compounds with their crystal structures and transition temperature greater than liquid nitrogen, 77 K.....	17
2.1 A partial list of few HTSC compounds with their crystal structures and transition temperature greater than liquid nitrogen, 77 K.....	18
2.2 Structural parameters for the orthorhombic phase ( $YBa_2Cu_3O_{6+x}$ ) with space group $Pmmm$ .....	24
2.3 Structural parameters for the tetragonal phase ( $YBa_2Cu_3O_{6+x}$ ) with space group $P4/mmm$ .....	25
6.1 Local structural parameters obtained from the constrained fit of the Fourier filtered Br $K$ -edge $k\chi(k)$ data. $S_o^2$ was estimated to be 0.72 from the first peak fit. Neutron-diffraction results on YBCO( $x=0.51$ ) [67] are given for comparison of Cu(1)-X interatomic distances and number of neighbors. Parameters for conventional CuBr powder are taken from [68]. Errors in the parameters were estimated from the covariance matrix generated from the fit and should be taken as relative errors corresponding to the reproducibility of the XAFS data.....	96
6.2 Local structural parameters obtained from the constrained fit of the Fourier filtered Cu $K$ -edge $k\chi(k)$ data. $S_o^2 = 0.8$ for all Cu-O bonds and 0.9 for all other bonds. Three models (S1-S3) of Cu-O pair distribution are constructed as described in the text. Reduced agreement factor, $R_a = 1/(\gamma M) \sum_i^M k(\chi_i^{exp} - \chi_i^{calc})$ , where $M$ is the number of data points, and $\gamma$ is the number of degrees of freedom in the fit. S1-model does not pass the $\chi^2$ -test for the quality of the fit to the filtered data, while both S2 and S3 do. Neutron-diffraction results on YBCO( $x=0.51$ ) [67] are given for comparison of Cu(1)-X interatomic distances and the number of neighbors.....	101



**LIST OF TABLES**  
(Continued)

<b>Table</b>	<b>Page</b>
<p>6.3 Results of Ba <math>L_3</math>-edge XAFS analysis of the decomposed phase. <math>S_o^2 = 0.95</math>. Errors in numbers of Ba neighbor are below 25%. The constrained parameters are taken from neutron-diffraction results on YBCO (<math>x=0.51</math>). The loss of the XAFS signal in the medium-to-long range pair correlations (<math>R &gt; 4 \text{ \AA}</math>) is probably due to cancellations of these contributions in the aperiodic media .....</p>	106
<p>6.4 Local structural parameters for the oxygen and copper shells about the yttrium in normal and brominated YBCO(<math>x \sim 0.6</math>). Parameters are derived from the non-linear least square fit to the Fourier filtered <math>k\chi(k)</math> data. Back FT ranges were 1.4-2.2 and 2.3-3.1 <math>\text{\AA}</math>, respectively. From the fit of normal YBCO the <math>S_o^2</math> was estimated to be 0.9 and was fixed in the refinement of Br_YBCO. Only parameters referring to the distorted (decomposed) phase are listed for the two-phase model since the parameters for the undistorted phase were constrained to those in normal YBCO (first two rows in this Table). Neutron-diffraction results on YBCO(<math>x=0.51</math>) [67] are given for comparison.....</p>	109
<p>6.5 I <math>L_3</math>-edge XAFS data for I-YBCO. The local structural parameters are obtained by using the structural parameters at Br <math>K</math>-edge for Br-YBCO. <math>S_o^2</math> was estimated to be 0.82. Errors in the extracted parameters were estimated from the covariance matrix generated from the fit and should be considered as relative errors. ....</p>	121
<p>6.6 Comparison of I-YBCO with Br-YBCO XAFS data. The XAFS data for Br YBCO were taken from Table 6.1.....</p>	122

## LIST OF FIGURES

Figure	Page
<p>2.1 Crystal structures of TI based superconductors of the series compounds <math>Tl_2Ba_2Ca_{n-1}CuO_{4+2n}</math>, for <math>n=1</math> (a), for <math>n=2</math> (b). They differ by additional <math>CuO_2</math> layers separated by Ca ions [92, 94].....</p>	13
<p>2.1 Crystal structures of TI based superconductors of the series compounds <math>Tl_2Ba_2Ca_{n-1}CuO_{4+2n}</math>, for <math>n=3</math> (a), for <math>n=2</math> (b). They differ by additional <math>CuO_2</math> layers separated by Ca ions [92, 94].....</p>	14
<p>2.2 Basic structural unit of perovskite is a cube (a). One metallic atom A lies at the center. Eight smaller metallic atoms B occupy the corners and 12 nonmetallic atoms X are at the midpoint of the edges. The A and B atoms are cations (positively charged ions and the X atoms are negatively charged anions). (b). The six X anions that surround each B cation and are closely bound to it form the point of an octahedron. In such a model the basic structural unit becomes a group of eight corner linked octahedrons around an A cation [Ref. 8(a)].....</p>	19
<p>2.3 The tetragonal structure of <math>YBa_2Cu_3O_{6+x}</math>. For <math>x=0</math>, the oxygen atoms on sites denoted by the dashed ellipsoids are missing, leaving <math>Cu(O_4)_2</math> dumbbells oriented along the c-axis (above). The orthorhombic unit cell for <math>x=1</math> is given below (Fig. 2.4).....</p>	23
<p>2.5 Phase diagram of <math>T_C</math> as a function of oxygen concentration (x).....</p>	21
<p>3.1 Crystal structure of Pr doped YBCO. (a) <math>PrBa_2CuO_7</math> and (b) <math>Pr_2Ba_4Cu_8O_{16}</math> which is the double layer compound. The unit cell for (b) is twice as large as the formula unit, with chemical composition <math>Pr_2Ba_4Cu_8O_{16}</math> [94].....</p>	28
<p>4.1 Phase diagram for the electron-electron and electron-phonon interaction parameters at <math>T=0</math> and hole occupation <math>x=0.1</math>. Coexistence and annihilation of superconductivity (SC) and SDW is shown. The phase P is the paramagnetic phase produced by the annihilation of superconductivity by the electron-electron interaction [43].....</p>	58
<p>5.1 Schematic of backscattering process, atom-A is the absorbing atom and atom-B the backscattering neighboring atom (above). Extended X-ray Absorption Fine Structure (EXAFS) of <math>BaBr_2</math> powder sample, normalized and background subtracted (below).....</p>	61
<p>5.2 EXAFS at Br <math>K</math>-edge (<math>E_0=13474</math> eV) for <math>BaBr_2</math> powder sample, normalized and background subtracted (above). From the above EXAFS graph, <math>\chi(k)</math> was extracted and weighted by <math>k^2</math> (<math>k^2\chi(k)</math>) below.....</p>	74

**LIST OF FIGURES**  
(Continued)

Figure	Page
6.1 Experimental set up for halogenation of YBCO single crystals. YBCO single crystals were placed inside the tube furnace under nitrogen gas flow for bromination and argon gas flow for iodination experiments .....	84
6.1 (a). Kinetics of oxygen uptake of YBCO <sub>6+x</sub> sample heated in O <sub>2</sub> at 1°C/min. Numbers on the plot refer to oxygen content [Goodenough <i>et. al.</i> ].....	84
6.2 Zero-field-cooled magnetization vs. temperature in a 20 Oe magnetic field for brominated (diamonds) and normal (open circles) YBCO( <i>x</i> ~0.6). Spectra are not corrected for the demagnetization factor. <i>T</i> <sub>C</sub> is taken at the onset for superconductivity. The untreated sample has a minor component (~ 15%) with <i>T</i> <sub>C</sub> ~ 88 K and major component with <i>T</i> <sub>C</sub> ~ 63 K. Bromination produces samples with <i>T</i> <sub>C</sub> ~ 89 K .....	85
6.3 (a) Br <i>K</i> -edge <i>k</i> χ( <i>k</i> ) vs <i>k</i> for brominated YBCO with x-ray polarization at 45 Deg to the <i>c</i> -axis. (b) Cu <i>K</i> -edge <i>k</i> χ( <i>k</i> ) vs <i>k</i> for brominated (solid line) and pristine YBCO( <i>x</i> ~0.6) (dashed line) with x-ray polarization parallel to <i>c</i> -axis. Cu <i>K</i> edge data were corrected for self-absorption as described in Ref. [59] .....	86
6.4 The Fourier transform (FT) of brominated YBCO. The oscillating curve (dashed line) is the imaginary part of the FT. The envelope (solid curve) is the magnitude of the FT. The data are transformed with a square window between 2.9-11.4 Å <sup>-1</sup> . Peak assignment is based on the multiple-shell model .....	91
6.5 Comparison of the Fourier-filtered data (solid line) with model involving Br – [O(4), Ba, Cu(1,2)] pairs (dashed line). Structural parameters extracted From the non-linear least square fit are provided in Table 6.1 .....	92
6.6 Polarized Br <i>K</i> -edge XANES spectra of BrYBCO, measured at φ=45° (solid line) and φ=90° (dotted line). Notice that no polarization dependence is observed implying that Br-O(4)-Ba-Cu(2) <sub>2</sub> Cu <sub>1</sub> -... nanoclusters are randomly distributed with respect to x-ray polarization and, therefore, with respect to host YBCO lattice. Br <i>K</i> -edge XANES of powder BaBr <sub>2</sub> .2H <sub>2</sub> O (dashed line) is to show that the formal Br valence in brominated YBCO is close to -1 .....	94
6.7 FT of Cu <i>K</i> -edge <i>k</i> <sup>2</sup> χ( <i>k</i> ) of untreated (solid line) and brominated (dashed line) YBCO ( <i>x</i> ~0.6). The data are transformed with a square window between 2.5-13.0 Å <sup>-1</sup> . The origin of the peaks is described in the text.....	95

**LIST OF FIGURES**  
(Continued)

<b>Figure</b>	<b>Page</b>
<p>6.8 Comparison of the Fourier-filtered Cu-O contribution to c-axis polarized with three structural models for the Cu-O pair distribution in BrYBCO. The back FT range is 1-2.1 Å, using a square window. A three-shell model providing the best fit to the filtered data assumes two Cu-O distances resembling to Cu(1)-O(4) and Cu(2)-O(4) in optimally doped single-crystal YBCO (x~0.9-1) and more Cu-O distance (1.95 Å) due to the decomposed phase. The latter distance is mostly responsible for the increase of the Cu-O peak intensity seen in Fig. 6.7 for the brominated YBCO sample.....</p>	99
<p>6.9 Effect of bromination on the Cu K-edge XANES of YBCO (x~0.6) measured with x-ray polarization vector parallel to the c-axis (E  C) and parallel to the ab-plane (E  ab). Cu K-edge XANES spectrum of the CuO powder (dot-dashed line) and (E  ab) spectra are offset for clarity .....</p>	100
<p>6.10 Contribution to the Cu K-edge XANES from the decomposed phase. The residual Cu K-edge polarization dependence implies that domains forming the decomposed phase are differently ordered with respect to the polarization vector whereas the impurities domains Br-O-Ba-Cu-... and Br-Cu are randomly oriented. The XANES spectrum of the powder CuO is shown by the dot dashed line for comparison.....</p>	104
<p>6.11 Fourier transform at the Ba L<sub>3</sub>-edge <math>k\chi(k)</math> (a) Magnitude and imaginary parts of Normal and brominated YBCO single crystals. The Fourier Transform range is 1.8-9 Å<sup>-1</sup> with a square window. (b) Fit to the FT of <math>k\chi(k)</math> Performed in r-space for 1.7-3.7 Å. The constrained fit includes Ba-O,-Cu(1,2) Y and Ba-Ba shells.....</p>	105
<p>6.12 FT of Y K-edge <math>k\chi(k)</math> of untreated (solid line) and brominated (dashed line) YBCO (x~0.6). The data are transformed with a square window between 1.9-14.7 Å<sup>-1</sup> .....</p>	108
<p>6.13 Polarized Cu K, Y K, Ba L<sub>3</sub> and Br K-edge measurements are consistent with nanoscale heterogeneity in brominated YBCO (x~0.6). Well ordered undistorted YBCO lattice hosts differently and heavily distorted decomposed inclusions (gray regions) which account for about 1/3 of the volume. The decomposed phase consists of nano-fragments (nano-domains) formed as a result of truncation of the YBCO lattice predominantly along the Cu(1)-O(1) planes. The typical size of the decomposed areas is unknown but is expected to be no less than 7-8 Å since bromine enters the Cu(1) site forming impurity phases (small black regions inside the gray ones) causing at least 8 unit cells to decompose. The local structure of the host lattice coincides with the fully oxygenated YBCO one, presumably due to reoxygenation of the YBCO</p>	

**LIST OF FIGURES**  
(Continued)

<b>Figure</b>	<b>Page</b>
(x~0.6) by O(1) diffusing from the decomposed regions. The decomposed and impurity phases are given in terms of cluster expansion .....	108
6.14 Fourier transform of $k^2\chi(k)$ in $r$ -space for the iodinated YBCO(x~0.27) single crystal at the $IL_3$ -edge. Notice the first peak between 1-1.9 Å in the Fourier transform corresponds to the I-O(4).....	118
6.15 The Fourier transform (FT) of iodinated YBCO at the $IL_3$ - edge. The oscillating curve (dashed line) is the imaginary part of the FT. The envelope (solid curve) is the magnitude of the FT. The data are transformed with a square window between 3.75-8.66 Å <sup>-1</sup> .....	119

# CHAPTER 1

## INTRODUCTION

### 1.1 Discovery of Superconductivity and its Applications

#### 1.1.1 Discovery of Superconductivity

Materials that have no resistance to the flow of electricity are called superconductors. Not only have the limits of superconductivity not yet been reached, but the theories that explain superconductor behavior seem to be constantly under review (see ref. in Chapter 4). In 1911 superconductivity was first observed by Dutch physicist Heike Kamerlingh Onnes of Leiden University [1(a)]. When he cooled mercury to the temperature of liquid helium which is 4 K (Kelvin), its resistance suddenly disappeared. It was necessary for Onnes to come up with 4 degrees of the coldest temperature that is theoretically attainable to witness the phenomenon of superconductivity. Later in 1913, he won a Nobel Prize in Physics for his research in this area. After his discovery of superconductivity in mercury (Hg), scientists dreamed of investigating this unusual behavior of matter at low temperatures. Few decades later, one of the greatest investigations in understanding this unusual behavior of matter at low temperatures occurred in 1933 when Walter Meissner and Robert Ochsenfeld discovered that a superconducting material will repel a magnetic field [1(b)]. This phenomenon is called the Meissner Effect (ME)

#### 1.1.2 Perfect Diamagnetism

For weak magnetic fields, the magnetic susceptibility of a superconductor (in gaussian units) is given by:

$$\chi_m = -\frac{1}{4\pi} \quad (1.1)$$

This means that the magnetic flux lines are completely expelled from the superconductor and that there is a force pushing away superconductors from magnetic fields. Thus ideal superconductors are perfect diamagnets which exhibit zero magnetic field in the interior of bulk samples.

It is natural to wonder why superconductivity represented such a difficult problem in physics that forty-six years had to pass before a quantitative quantum mechanical model was developed. For almost twenty years, the physics community did not have the basic building blocks needed to formulate a solution to the quantum theory of normal metals. The ME discovered in 1933 was one of the fundamental observations. Once the building blocks were in place, it quickly became clear that the characteristic energy associated with the formation of the superconducting state is tiny, roughly a millionth of the normal state characteristic electronic energies.

Soon, theorists around the world focused their attention on developing a phenomenological description of superconducting flow, one among many was Fritz London (FL). In 1935, he pointed out that superconductivity is a quantum phenomenon in a macroscopic scale with the lowest energy state separated by a finite interval from the excited states called the energy gap and diamagnetism is its fundamental property.

### **1.1.3 Energy Gap (EG)**

This refers to the minimum energy value needed for electronically exciting the system from its ground state. The energy gap:

$$E_g = 2|\Delta| \quad (1.2)$$

was conjectured theoretically by F. London in 1935 and observed by infrared measurements in 1957 and by electron tunneling in 1960, where  $\Delta$  is the gap width. Limits to the lower and upper bounds of the superconducting gap were first given by infrared absorption in 1937 and microwave surface resistance measurements in 1940.

Now, we introduce some other basic building blocks for understanding the properties of matter at low temperatures.

(1) First came the recognition that electrons in a metal move in a periodic potential produced by ions which oscillate about their equilibrium positions and the motion of these ions can be described as a collective mode called Phonons.

(2) Next, in the course of the development of the quantum theory came the discovery by Pauli of the exclusion principle which bears his name that, no two electrons can have the same quantum numbers. Particles which possess an intrinsic spin ( $S$ ) of one-half are known as fermions, in honor of the work of Fermi who, with Dirac, developed the statistical theory of electron behavior at finite temperatures, the Fermi-Dirac Statistics (FDS).

It is important to mention that, in the momentum space description of simple metals the ground state is a sphere with radius  $P_f$  which is determined by the electron density.

Since the electrons move freely in simple metals, the energy of the outermost electrons is given [1]:

$$E_F = \frac{P_F^2}{2m_e} \quad (1.3)$$



where  $P_F$  is the momentum at the Fermi surface and  $m_e$  is the electron mass. This energy is very large compare to their average thermal energy  $KT$ , as a result of this only a fraction  $\frac{KT}{E_F}$  of the electrons are excited above the ground state, where  $K$  is Boltzman's constant and  $T$  is temperature. The electrons interact with each other by coulomb's law and their elementary excitations are quasi-particles the electrons plus their associated cloud of other electrons and phonons which accompany electrons as they move through the lattice. Then and still now, the question is widely open on how these interacting electrons could undergo a transition to the superconducting state.

An essential clue came in 1950 when researchers at the National Bureau of Standard and Rutgers University, discovered that the superconducting transition of lead depended on its isotopic mass  $M$

#### 1.1.4 Isotope Effects

Early experiments by Maxwell, Nesbit, Reynolds, Serin and Wright in 1950 showed an interesting dependence of  $T_C$  of a superconductor on the isotopic mass of the atomic nuclei that make up the material. They showed the following:

$$M^\alpha \times T_c = Const \quad (1.4)$$

where  $M$  is the nuclear mass, the exponent  $\alpha$  is about 0.5, for Pb  $\alpha=0.485$ . Several groups have shown that for high temperature superconducting (HTSC) materials this dependence holds but with  $\alpha$  much less than 0.5.

In the following year, Herbert Frohlich, who was visiting Purdue from his home University of Liverpool, and John Bardeen, who was then at Bell Laboratories, tried and

failed to construct a theory based on electron-phonon interaction. What they did can be visualized with the aid of the diagrams introduced by Richard Feynman.

When an electron emits and absorbs a phonon, its properties are modified by this dynamic coupling to the lattice and the change in its energy is inversely proportional to  $M^{\frac{1}{2}}$ . Frohlich then considered the next possibility, where one sees an electron emitting a phonon which is subsequently absorbed by a second electron, this phonon induced interaction is possible when electrons are close to the fermi surface. This kind of interaction is similar to the waterbed problem, two persons sharing a waterbed have a tendency to be attracted to its center by the same kind of induced process which attracts the electrons.

In subsequent decades other superconducting metals, alloys and compounds were discovered. In 1941, Niobium-Nitride was found to superconduct at 16 K . In 1953 Vanadium-Silicon displayed superconductive properties at 17.5 K and in 1962 scientists at Westinghouse developed the first commercial superconducting wire an alloy of niobium and titanium.

It is known that, the first widely accepted theory in understanding superconductivity was advanced in 1957, by American physicists John Bardeen, Leon Cooper, and John Schrieffer (BCS theory see Chapter 4). Their theories of superconductivity became known as the BCS theory (for Bardeen, Cooper and Schrieffer) and resulted in a Nobel Prize in 1972. The mathematically-complex BCS theory, explained superconductivity at temperatures close to absolute zero for elements and simple alloys.

It very successfully describes the superconducting properties of weak superconductors such as aluminum, which are weak because of the small strength of the electron-phonon interaction. Further refinements of the theory have led to the strong coupling theory of Eliashberg in 1960 which describes the properties of strong superconductors such as lead. It is important to mention that, the distinction between weak and strong is roughly given by the value of the electron-phonon mass enhancement factor  $\lambda$ , as shown by McMillan in 1968 [2].

Superconductors can be divided into two types, type I and type II superconductors.

Type I superconductors (Table 1.1), are mainly comprised of pure metals that normally show *some* conductivity at room temperature, also known as the soft superconductors which were discovered first and require the coldest temperatures to become superconductive.

They are characterized by a very sharp transition to a superconducting state and by perfect diamagnetism.

Ironically, copper, silver and gold, three of the best known metallic conductors, do not rank among the superconductive elements.

Type II superconductors (Table 1.2), is also comprised of metallic compounds and alloys except for the elements vanadium, technetium and niobium. They achieve higher  $T_c$  than type I superconductors by a mechanism that is still not completely understood.

**Table 1.1** Some type I superconductors with their respective  $T_C$ 's.

\* First superconductor discovered in 1911 [1(a)].

<b>ELEMENTS</b>	<b>SYMBOLS</b>	<b>TEMPERATURES (<math>T_C</math>)</b>
Lead	Pb	7.2
Lanthanum	La	4.9
Tantalum	Ta	4.47
Mercury *	Hg	4.15
Tin	Sn	3.72
Indium	In	3.40
Thallium	Tl	1.70
Rhenium	Re	1.697
Proctatinium	Pa	1.40
Thorium	Th	1.38
Aluminum	Al	1.175
Gallium	Ga	1.10
Molybdenum	Mo	0.915
Zinc	Zn	0.85
Osminium	Os	0.66
Zirconium	Zr	0.61
Titanium	Ti	0.40

**Table 1.2** Some type II superconductors listed with their respective descending  $T_C$  [3, 3(a), 3(b), 3(c), 5, 7, 111]

### Mercury Based High Temperature Superconductors

COMPOUNDS	TEMPERATURES ( $T_C$ )
$Hg_{0.8}Tl_{0.2}Ba_2Ca_2Cu_3O_{8.33}$	138
$HgBa_2Ca_2Cu_3O_8$	133-135
$HgBa_2Ca_{1-x}Sr_xCu_3O_{6+}$	123-124
$HgBa_2Cu_2O_{4+}$	94-98

### Thalium Based High Temperature Superconductors

COMPOUNDS	TEMPERATURES ( $T_C$ )
$Tl_{1.6}Hg_{0.4}Ba_2Ca_2Cu_3O_{10}$	130
$Tl_2Ba_2Ca_2Cu_3O_{10}$	127
$TlBa_2Ca_2Cu_3O_{9+}$	123
$Tl_{0.5}Pb_{0.5}Sr_2Ca_2Cu_3O_9$	120
$TlBa_2Ca_3Cu_4O_{11}$	112
$Tl_2Ba_2Ca_3Cu_4O_{11}$	112

### Bismuth Based High Temperature Superconductors

COMPOUNDS	TEMPERATURES ( $T_C$ )
$Bi_{1.6}Pb_{0.6}Sr_2Ca_2Sb_{0.1}Cu_3O_x$	115
$Bi_2Sr_2Ca_2Cu_3O_{10}$	110
$Bi_2Sr_2CaCu_2O_9$	110
$Bi_2Sr_2CaCu_2O_8$	80

Table 1.2 (continued)

## Rare Earth Based High Temperature Superconductors

---

COMPOUNDS	TEMPERATURES (T <sub>C</sub> )
TmBa <sub>2</sub> Cu <sub>3</sub> O <sub>7</sub>	90
Gd Ba <sub>2</sub> Cu <sub>3</sub> O <sub>7</sub>	94
YBa <sub>2</sub> Cu <sub>3</sub> O <sub>7+</sub>	93
Y <sub>2</sub> Ba <sub>4</sub> Cu <sub>3</sub> O <sub>15</sub>	93
Yb <sub>0.9</sub> Ca <sub>0.1</sub> Ba <sub>1.8</sub> Sr <sub>0.2</sub> Cu <sub>4</sub> O <sub>8</sub>	86
YbBa <sub>1.6</sub> Sr <sub>0.4</sub> Cu <sub>4</sub> O <sub>8</sub>	78

## Other Cuprate Superconductors

---

COMPOUNDS	TEMPERATURES (T <sub>C</sub> )
(Sr,Ca) <sub>5</sub> Cu <sub>4</sub> O <sub>8</sub>	70
Pb <sub>2</sub> Sr <sub>2</sub> Ycu <sub>3</sub> O <sub>8</sub>	70
(La,Sr,ca) <sub>3</sub> Cu <sub>2</sub> O <sub>6</sub>	58
La <sub>1.85</sub> Sr <sub>0.15</sub> CuO <sub>4</sub>	40
(La,Ba) <sub>2</sub> CuO <sub>4</sub>	35-38
(Nd,Sr,Ce) <sub>2</sub> CuO <sub>4</sub>	35
Pb <sub>2</sub> (Sr,La) <sub>2</sub> Cu <sub>2</sub> O <sub>6</sub>	32

## **1.2 Applications of Superconductivity.**

### **1.2.1 Power Quality Conditioning in Factories**

The concepts of superconducting magnetic energy storage (SMES) is one possible answer to the power-quality problem. What SMES does, is to store energy in a magnetic field of a superconducting coil without any resistive losses. A dc current will continue to persist in a superconductor as long as the coil is kept cold (an ac current in a SMSES would be lossy and inefficient)

### **1.2.2 Magnetic Separation**

Superconducting Magnetic Energy Storage is not the only use of superconductivity by industry. Since superconductors enable high magnetic fields to be sustained, almost any application that utilizes a high magnetic field is eligible for superconductivity.

In many high-magnetic field applications, e.g., measurement systems such as magnetic resonance imaging (MRI), some of the available field strength must be sacrificed in the interest of achieving uniformity and stability. However, there are applications of magnetic fields that can have great commercial value. For industry, the case of magnetic separation is a good example.

Conventional electromagnets can be used to separate iron from aluminum or from copper scrap since magnetic fields are not generally strong enough to divert impurities from water or flue gas streams. For example, a superconducting magnet of 20 T (Tesla) would be a very effective separation device even if it were non uniform, variable and suffered brief intermittent outages.

### 1.2.3 Medical Applications

The most familiar application of superconducting technology, is in magnetic resonance imaging (MRI). MRI is a noninvasive technique for seeing inside the body which uses no ionizing radiation. Almost unheard of in 1980, MRI has now found a widespread use in diagnosing injuries to bones and joints and detecting tumors. Today, MRI is regarded as a primary diagnostic instrument for many diseases that change the anatomy.

### 1.2.4 Levitation

Magnetic levitation using superconducting magnets was first suggested in 1963, by Powell, soon after the discovery of type II superconductors (see Table 1.2) with their implications for carrying large currents. Powell and Danby proposed the novel idea of a null-flux suspension system that would minimize the drag force and thus require much less propulsion power.

The most well-advertised possible application of superconductivity is that of Maglev trains (levitating trains), proposed to run at  $500 \frac{km}{h}$  (300mph). The public imagination is captured by the image of what amounts to an extremely low-flying aircraft hovering about 10 to 20 cm above a guiderail, whisking passengers silently, swiftly, and comfortably from city to city. This is commonly seen as an idea whose time has come, and high-temperature superconductivity could make it practical and inexpensive to operate.



## CHAPTER 2

### HIGH TEMPERATURE COPPER-OXIDE SUPERCONDUCTORS

#### 2.1 History of Copper-Oxide Superconductors

The discovery of superconductivity by Kammerlingh Onnes in 1911 in mercury (Hg) at 4 K, pushed scientists to investigate the superconducting states of many materials, to increase their transition temperatures to higher temperatures. The progress was quite very slow, but it is important to emphasize that the discovery of  $T_C$  above 10 K in NbC and NbN was a breakthrough. Superconductivity has been previously found in some perovskite and related compounds such as SrTiO<sub>3</sub> with  $T_C$  less than 1 K and BaPb<sub>1-x</sub>Bi<sub>x</sub>O<sub>3</sub> with  $T_C = 13$  K. The discovery of the A15 compounds with  $T_C$  found up to 20 K in the late 1960s and earlier 1970s, was the result of hard work for two decades in the search of high temperature superconductors (HTSC).

Finally in 1986, Bednorz and Muller discovered a  $T_C$  higher than in A15 compounds in the copper oxide based system, they found a transition occurring to the superconducting state in the La-Ba-Cu-O system near 30 K. Their result was then confirmed and refined in several laboratories across the world. They established that the  $T_C$  is in the range between 20-40 K for La<sub>2-x</sub>M<sub>x</sub>CuO<sub>4-y</sub> with M= Ba, Sr, Ca and when pressure is applied, the coefficient of temperature is larger and drives the  $T_C$  above 50 K in the M= Sr based system.

A year later in 1987, Wu. *et al.*, [3] found a  $T_C$  above 90 K for the YBaCuO<sub>7-y</sub> (123 or YBCO) compound, placing it among the first of the copper oxide compounds to exhibit superconductivity above the temperature of liquid nitrogen temperature (77 K).

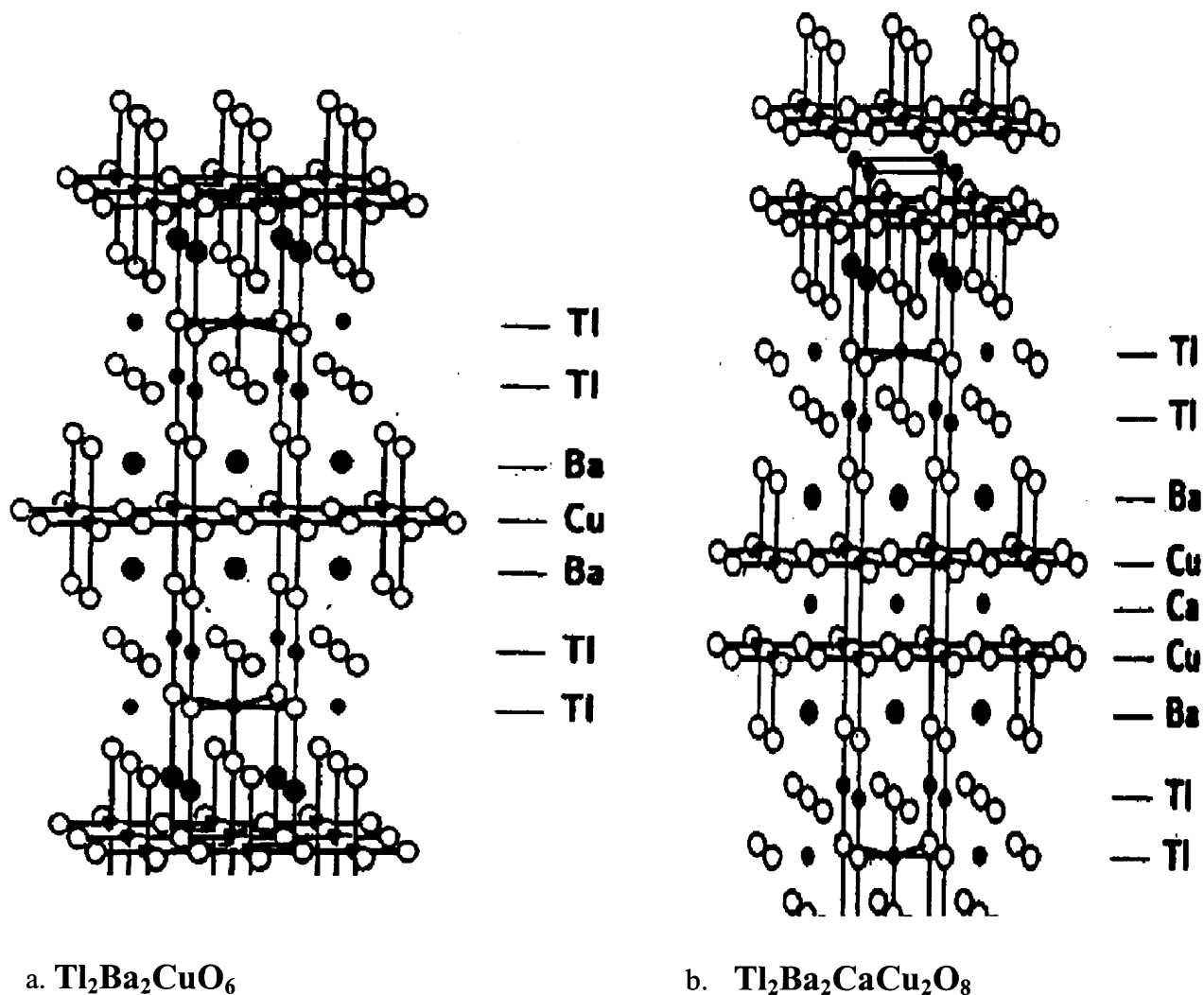
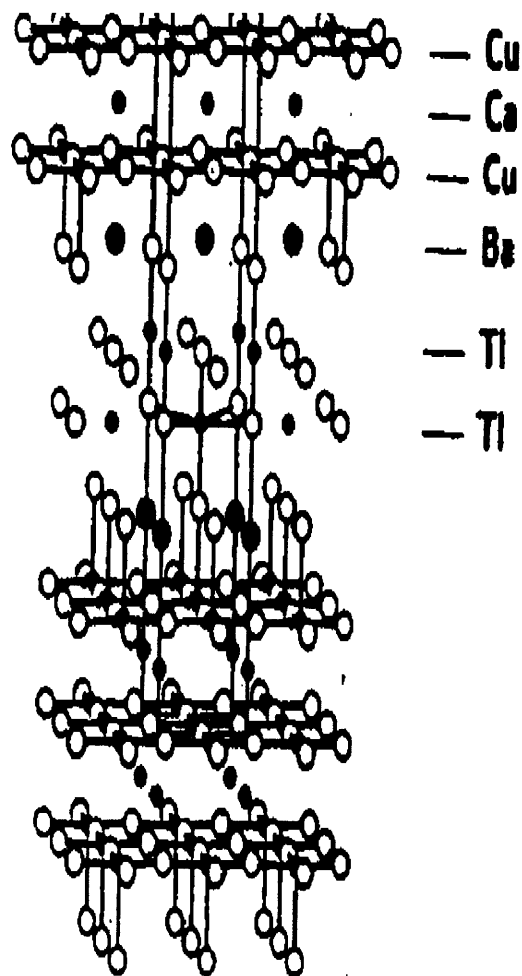


**Figure 2.1** Crystal structures of Tl based superconductors of the series compounds  $\text{Tl}_2\text{Ba}_2\text{Ca}_{n-1}\text{Cu}_n\text{O}_{4+2n}$ , for  $n=1$  (a), 2 (b). They differ by additional  $\text{CuO}_2$  layers separated by Ca ions[92,94]



c.  $\text{Tl}_2\text{Ba}_2\text{Ca}_2\text{Cu}_3\text{O}_{10}$

**Figure 2.1(continued)** Crystal structures of Tl based superconductors of the series compounds  $\text{Tl}_2\text{Ba}_2\text{Ca}_{n-1}\text{Cu}_n\text{O}_{4+2n}$ , for  $n=3$ . They differ by additional  $\text{CuO}_2$  layers separated by Ca ions[92,94]

It was also found that in  $\text{La}_{2-x}\text{Ba}_x\text{CuO}_4$  (LBCO), Ba can be replaced by Ca or Sr without changing the superconducting properties of the material. Similarly, in YBCO materials Y can be replaced by almost any rare earth (except Ce and Pr) without changing the  $T_C$  of the material. Michel *et al.*, [4] reported a transition temperature in Bi-Sr-Cu-O (BSCO) with  $T_C = 20$  K, their result led to the discovery of bulk superconductivity at 85 K and an evidence for superconductivity at 110 K in the Bi-Sr-Ca-Cu-O Maeda *et al.*, [5]. Also Tarascon *et al.*, [6] performed magnetization measurements on crystals weighting each about 0.1 mg, they found that most these crystals have bulk property and exhibit two  $T_C$ 's of 85 and 110 K. Hazen *et al.*, [7] found the Tl-Ba-Cu compound to be a high temperature superconductor, when doped with Ca the  $T_c$  increased up to 100K. The common feature of all copper-oxide base superconductors is that, they all have layers of copper-oxide sheets which are believed to play a very important role in the occurrence of high temperature superconductivity, the other layers contribute to the mechanisms responsible for superconductivity by maintaining charge equilibrium and stabilizing the crystal structures. Electron transport occurs in these  $\text{CuO}_2$  planes, few copper-oxide based superconductors are shown, see, Fig.2.1 Fig.2.3 and Fig.2.4.

In contrast to the Cu-O based superconductors, superconductivity was found in  $\text{Ba}_{1-x}\text{K}_x\text{BiO}_3$  (Ba-K-Bi-O) compound at 30 K by Cava *et al.*, [8] they claimed it to be structurally and electrically similar to the  $\text{Ba}(\text{Pb}, \text{Bi})\text{O}_3$  and it was shown that the Ba-K-Bi oxide has a three dimensional structure with Bi-O bond distances forming a cubic network [9]. The mechanisms by which superconductivity occurs is not well understood not only for Cu-O based system but for superconductors like the Ba-K-Bi oxide. Since

the CuO(2) planes are absent in the Ba-K-Bi oxide, this suggests that these planes are not responsible for HTSC to occur in them and it was concluded that the mechanisms by which HTSC occurs in these two materials are completely different. With a proper understanding of the mechanisms responsible for superconductivity in these compounds, it cannot be ruled out that a way might be found to synthesize oxide superconductors with higher  $T_C$ 's. This is why several mechanisms have been suggested in order to explain the occurrence of superconductivity in these compounds, one of the most known out of many is the BCS theory (see Chapter 4) which is up to now not well understood and controversial. Whether the attractive force responsible for the pairing (electron-electron) mechanism in high temperature superconductors is due to the weak electron-phonon interaction as seen in conventional BCS type superconductors is still not clear.

The major part of this thesis is based on recently published XAFS data on brominated and iodinated YBCO single crystals, therefore it is important to introduce some properties of YBCO compound.

**Table 2. 1** Here is a partial list of few HTSC compounds with their crystal structures and transition temperature greater than liquid nitrogen temperature, 77 K.

#### Mercury Based High Temperature Superconductors

COMPOUND	CRYSTAL STRUCTURE	$T_C$ (K)
HgBa <sub>2</sub> Ca <sub>2</sub> Cu <sub>3</sub> O <sub>8</sub>	Pmm; a= 3.85, c= 15.85	133
HgBa <sub>2</sub> Ca <sub>3</sub> Cu <sub>4</sub> O <sub>10</sub>	Pmm; a= 3.85, c= 19.01	127
HgBa <sub>2</sub> CaCu <sub>2</sub> O <sub>6</sub>	14/mmm; a= 3.86, c= 12.71	123
HgBa <sub>2</sub> Cu <sub>2</sub> O <sub>4</sub>	14/mmm; a= 3.88, c= 9.51	94

Table 2.1 (continued)

**Thalium Based High Temperature Superconductors**

<b>COMPOUND</b>	<b>CRYSTAL STRUCTURE</b>	<b>T<sub>c</sub>(K)</b>
Tl <sub>2</sub> Ba <sub>2</sub> Ca <sub>3</sub> Cu <sub>4</sub> O <sub>10</sub>	14/mmm; a= 3.85, c= 35.9	128
Tl <sub>2</sub> Ba <sub>2</sub> CaCu <sub>3</sub> O <sub>8</sub>	14/mmm; a= 3.86, c= 29.32	119
TlBa <sub>2</sub> Ca <sub>2</sub> Cu <sub>3</sub> O <sub>8</sub>	P4/mmm; a= 3.85, c= 15.91	110
TlBa <sub>2</sub> CaCu <sub>2</sub> O <sub>7</sub>	A2aa; a= 5.47, b= 5.47, c= 23.24 14/mmm; a= 3.87, c= 23.2	92

**Bismuth Based High Temperature Superconductors**

These are the most studied and developed compounds

<b>COMPOUND</b>	<b>CRYSTAL STRUCTURE</b>	<b>T<sub>c</sub>(K)</b>
Bi <sub>2</sub> Ca <sub>2</sub> Sr <sub>2</sub> Cu <sub>3</sub> O <sub>10</sub>	A2aa; a= 5.39, b= 5.40, c= 37.0	110
Bi <sub>2</sub> CaSr <sub>2</sub> Cu <sub>2</sub> O <sub>8</sub>	A2aa; a= 5.39, b= 5.40, c= 37.0	92

**Rare Earth Based High Temperature Superconductors**

These are the most studied and developed compounds

<b>COMPOUND</b>	<b>CRYSTAL STRUCTURE</b>	<b>T<sub>c</sub>(K)</b>
YBa <sub>2</sub> Cu <sub>3</sub> O <sub>7</sub>	Pmmm; a= 3.82, b= 3.89, c= 11.68	93
Y <sub>2</sub> Ba <sub>4</sub> Cu <sub>7</sub> O <sub>15</sub>	Ammm; a= 3.80, b= 3.87, c= 50.29	93
YBaSrCu <sub>3</sub> O <sub>7</sub>	Pmmm; a= 3.80, b= 3.84, c= 11.54	84
YBa <sub>2</sub> Cu <sub>4</sub> O <sub>8</sub>	Ammm; a= 3.84, b= 3.87, c= 27.24	80

**Table 2. 1 (continued)****Rare Earth Based High Temperature Superconductors**

<b>COMPOUND</b>	<b>CRYSTAL STRUCTURE</b>	<b>T<sub>c</sub>(K)</b>
SmBaSrCu <sub>3</sub> O <sub>7</sub>	14/mmm; a= 3.85, c= 11.53	86
DyBaSrCu <sub>3</sub> O <sub>7</sub>	Pmmm; a= 3.80, b= 3.85, c= 11.56	90
HoBaSrCu <sub>3</sub> O <sub>7</sub>	Pmmm; a= 3.79, b= 3.85, c= 11.55	87

**2.2 Properties of High Temperature Superconductors****2.2.1 Structure of High Temperature Superconductors**

Perovskite Oxides, which derive from the specific mineral known as BaBiO<sub>3</sub> are ceramics. Ceramics are solid materials combining metallic elements with nonmetals, usually oxygen, that have a particular atomic arrangement. Perovskites are the earth's most abundant minerals and have long been of interest to geologists because the clues they hold for the planet's history. They have attracted a lot of scientists from the technological point of view as well because, as a group, natural and synthetic perovskites show an array of electrical properties. They are found as insulators (non superconductors) semiconductors, metal-like conductors and now high temperature superconductors. The perovskite industry nowadays, is more than \$20 billion per year [8(a)] electroceramics a figure that may soon be eclipsed by applications of high temperature superconductors (see Chapter 1).

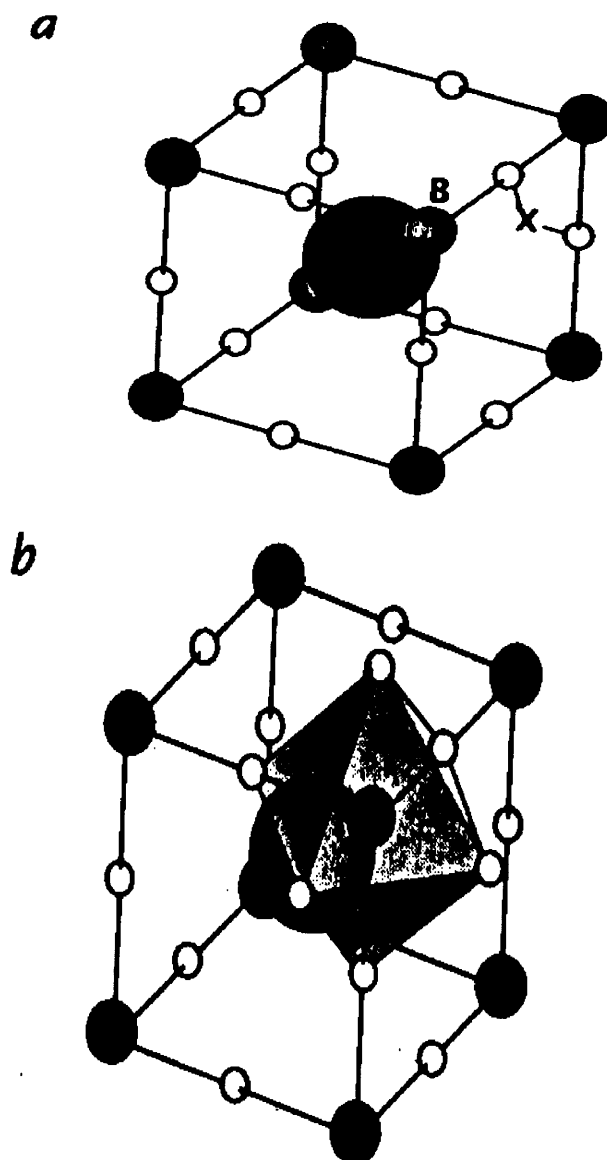


**Figure 2.2** Basic structural unit of perovskite is a cube (a). One metallic atom A lies at the center. Eight smaller metallic atoms B occupy the corners and 12 nonmetallic atoms X are at the midpoint of the edges. The A and B atoms are cations (positively charged ions) and the X atoms are negatively charged anions. (b). The six X anions that surround each B cation and are closely bound to it form the point of an octahedron. In such a model the basic structural unit becomes a group of eight corner linked octahedrons around an A cation [Ref. 8(a)].

### 2.2.2 Perovskite Structure

Cubic perovskites usually, are described by the generalized formula  $ABX_3$ , which consists of cubes made of three distinct different chemical elements [8(a)]. These



elements are present in a ratio of 1:1:3, where the A and B atoms are metallic cations (ions with positive charge) and the X atoms are nonmetallic anions (ions with negative charge). The A cation which is the larger of the two metals present, lies at the center of each cube and the B cations occupy all the eight corners and the X anions are located at the midpoint of the cubes's 12 edges (see Fig.2.2).

It is known that many elements from the periodic table can be combined to form ideal or modified perovskites, barium, potassium and the rare earth elements. Elements from cerium through lutetium, numbers from 58 to 71 in the periodic table of the elements which can fill the A position. Also 50 different elements, more than half of the stable entries in the periodic table are known to adopt B sites. The X atoms can be taken not only by oxygen, but by members of the halogen family of nonmetals (see Chapter 5). Almost, all high temperature superconductors are type II superconductors. Despite the fact that these high temperature superconducting compounds seem to be very complex and have a wide range of crystal structures, there is an underlying pattern of these compounds (materials). First of all their crystal structures are related to the perovskite structure of  $\text{SrTiO}_3$ . Next, they are cuprates with copper oxygen planes. Finally, the other atoms come from a limited part of the periodic table. These atoms are either 6s 6p (Hg, Tl, Pb, Bi), early transition metals, the 3d (Ca), 4d (Rb, Sr, Y) or 5d (Ba, La) or rare earth elements (Nd, Sm, Eu, Gd, Dy, Ho, Er, Tm). Unfortunately, these compounds are not understood well enough to use this pattern to systematically search for compounds with higher superconducting transition temperatures ( $T_C$ ).

In Table 2.1 is shown a partial list of few HTSC with their crystal structures and transition temperatures.

### 2.3 Properties of $\text{YBa}_2\text{Cu}_3\text{O}_{6+x}$

The crystal structure of  $\text{YBa}_2\text{Cu}_3\text{O}_{6+x}$  depends on the presence of the oxygen atoms in the material, the concentration of oxygen  $x$  in this material ranges from  $0 < x < 1$ . This means for  $x=0$ ,  $x=1$  in  $\text{YBa}_2\text{Cu}_3\text{O}_{6+x}$  the compound is in its insulating (tetragonal state) and superconducting (orthorhombic state) respectively. Phase diagram of  $T_C$  as a function oxygen concentration, Fig. 2.5

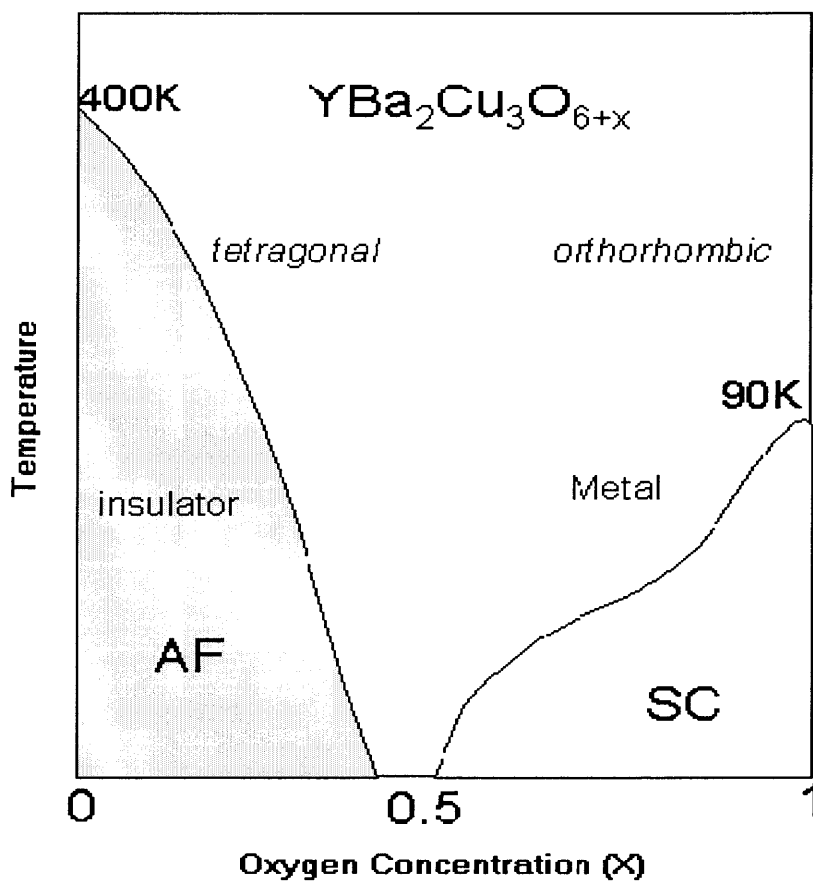


**Figure 2.5** Phase diagram of  $T_C$  as a function of oxygen concentration (X)

### 2.3.1 Orthorhombic Structure of $\text{YBCO}_{6+x}$

Since the discovery by Wu *et. al.*, [3] HTSC in YBCO (123) system with  $T_C$  above 90 K, Extensive studies have been performed on the structure of these materials [3, 4, 10, 11, ,14, 95, 96] (table 2.2). It was reported that the HTSC phase of this material forms in an orthorhombic  $Pmmm$  structure with a single formula unit per primitive cell. The crystal structure is described in terms of Cu-O planes and Cu-O chains, the chains consist of Cu(1) and O(1) atoms along the b axis at  $(0,0,0)$  and  $(0, \frac{1}{2}, 0)$  respectively (see Fig.2.4).

The chains are regarded as ribbons, however since the O(4) atom lies above and below the Cu(1) atom at  $(0,0, z_{O4})$  and the Cu-O distance is the smallest in the structure [10, 11].

The Cu(1) atom is fourfold coordinated with O ions and each O(1) ion is shared by two Cu(1) atoms. The planes or layers consist of Cu(2) sites at  $(0,0,z_{Cu(2)})$  neighbored by O(2) and O(3) sites at  $(\frac{1}{2}, 0, z_{O(2)})$  and  $(0, \frac{1}{2}, x_{O(3)})$ .

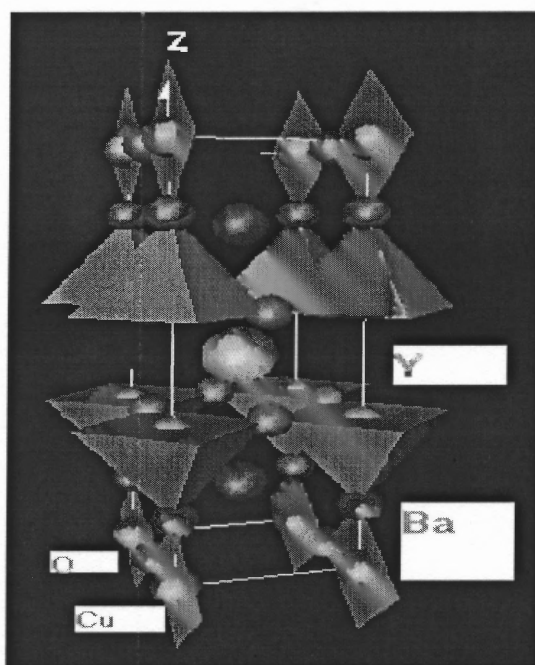
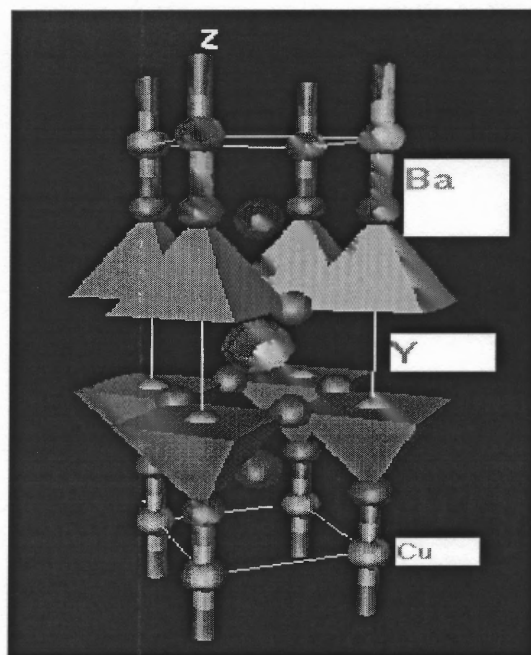


**Figure 2.3** The tetragonal structure of  $\text{YBa}_2\text{Cu}_3\text{O}_{6+x}$ . For  $x=0$ , the oxygen atoms on sites denoted by the dashed ellipsoids are missing, leaving  $\text{Cu}(\text{O}_4)_2$  dumbbells oriented along the  $c$ -axis (above). The orthorhombic unit cell is given below (Fig. 2.4)

### 2.3.2 Tetragonal Structure of $\text{YBa}_2\text{Cu}_3\text{O}_{6+x}$

The tetragonal structure in  $\text{YBa}_2\text{Cu}_3\text{O}_{6+x}$  corresponds to lower oxygen concentrations ( $x=0$ ) which leads to  $\text{YBCO}_6$  with a space group  $P4/mmm$  (see Fig.2.3).

The ideal symmetry of these phases can be described in terms of the composition of  $\text{YBa}_2\text{Cu}_3\text{O}_6$ , whose structure differs from the orthorhombic  $Pmmm$  structure given above by the removal of the Oxygen (O) ion from the chain O(1) site. It is important to mention that the lattice parameters of YBCO unit cell depend on the oxygen stoichiometry and temperature as well see Table 2.3 for the lattice parameters.

It was found that by replacing some of the Cu atoms in an orthorhombic superconducting YBCO with the 3d elements, the  $T_C$  of this material will drop significantly. Therefore, the following chapter will be devoted to doping an orthorhombic superconducting or an insulating non-superconducting YBCO systems.

**Table 2.2** Structural parameters for the orthorhombic phase ( $\text{YBa}_2\text{Cu}_3\text{O}_{6+x}$ ) with space group  $Pmmm$

LATTICE PARAMETERS	OXYGEN CONTENT	$T_C(\text{K})$
$a= 3.8231 \text{ \AA}$		
$b= 3.8864 \text{ \AA}$	$X \sim 1$	93
$c= 11.6807 \text{ \AA}$		

**Table 2.3** Structural parameters for the tetragonal phase ( $\text{YBa}_2\text{Cu}_3\text{O}_{6+x}$ ) with space group  $P4/mmm$

---

LATTICE PARAMETERS	OXYGEN CONTENT	$T_c(\text{K})$
a= 3.8600(1)		
b= 3.8600(1)	X~ 0	-
c= 11.8168(2)		

---

## CHAPETER 3

### EFFECT OF DOPING YBCO SAMPLES AND STRUCTURAL ORDER

#### 3.1 Chemical Doping of an Orthorhombic Superconducting or of an Insulating Non-superconducting YBCO

##### 3.1.1 Oxygen Doping of an Insulating Tetragonal YBCO System

Oxygen doping of insulating and tetragonal YBCO system have been done in two ways: The first way is annealing the YBCO sample in oxygen under ambient pressure and the second one is annealing in oxygen flow but under high pressure which is called high pressure oxygen annealing (HPA). Annealing insulating materials results in changing their phase from being insulating to superconducting with an increase of  $T_C$ , but HPA has been found to affect the transition temperature than ambient pressure annealing. Several groups have reported to have increase  $T_C$  for polycrystalline samples under HPA [12].

##### 3.1.2 Doping With Rare Earth and 3d Elements

Xiao *et al.* [13] performed substitution of the 3d elements (Ti, Cr, Mn, Fe, Co, Ni and Zn) on the Cu ions site, since their ionic and orbital structure are close to those of Cu. They substituted the 3d elements for 10% of the Cu ions and found that the substitution resulted a decrease in  $T_C$  in each case, but they claimed the change in  $T_C$  wasn't large enough to destroy superconductivity. When they increased the percentage of Cu substitution then, the  $T_C$  changed significantly. Another group Siergist *et al.*, [14] doped superconducting ceramic YBCO samples with aluminum at the copper site, found a degradation of the superconducting properties.

No element have been found for doping on the Cu site that either keeps the orthorhombic

symmetry or enhances the transition temperature in YBCO (123) compound. This is also true in the case of doping into the Ba site.

In contrast to the 3d elements substitution on the Cu site, several groups reported replacing the Y site with rare earth elements (La, Pr, Nd, Sm, Eu, Gd, Dy, Ho, Er, Tm, Yb) [15]. They showed that only Pr (Fig. 3.1) and La were not superconducting when replaced at the Y site, all other rare earth elements did show superconductivity behavior. Another group [16] prepared high temperature superconducting orthorhombic YBCO samples with potassium additives K-YBCO, then they doped these same samples with  $\text{KClO}_3$  and  $\text{K}_2\text{CO}_3$  compounds. They found that, the  $T_C^{\text{onset}}$  of most  $\text{KClO}_3$  doped samples was between 99 and 105 K much higher than the  $\text{K}_2\text{CO}_3$  doped system.

Soon after it was found that Pr suppresses the transition temperature in orthorhombic superconducting YBCO samples, a special interest was devoted to the PrYBCO system. Several groups have investigated the mechanisms responsible for  $T_C$  suppression in PrYBCO samples.

### 3.1.3 Pr Doped Orthorhombic Superconducting YBCO (123) Samples

The mechanism by which Pr suppresses  $T_C$  in the YBCO compound is still not well understood and unclear, recently [17] reported an inhomogeneous superconducting state with  $T_C = 92$  K in  $\text{PrBa}_2\text{Cu}_3\text{O}_7$  which contradicts the results of [15], they claimed that the key observation of superconductivity is sample preparation conditions that minimizes the amount of Pr in the Ba-site. A year later, it was shown superconductivity in single crystals of PrYBCO for the first time [18].



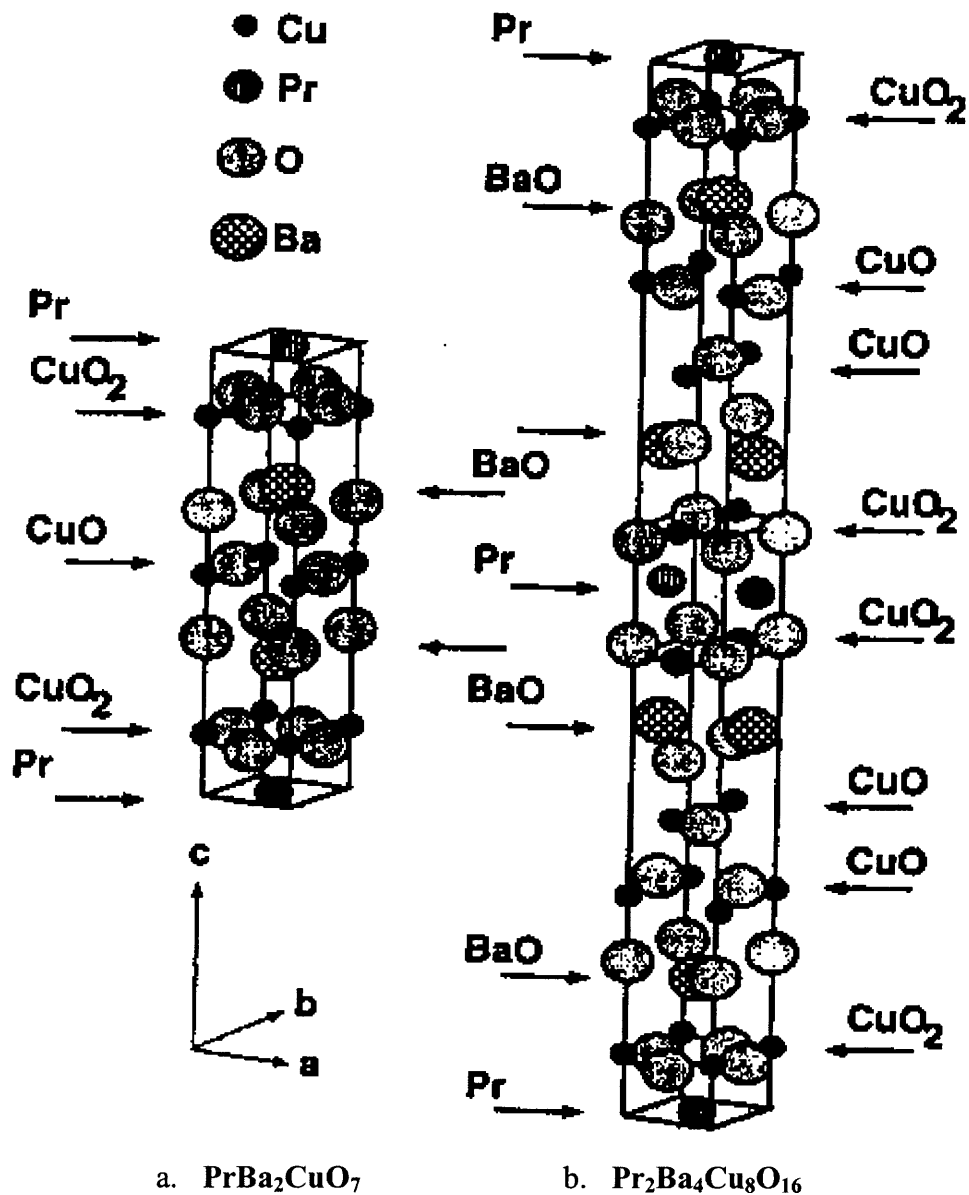


**Figure 3.1** Crystal structure of Pr doped YBCO. (a)  $\text{PrBa}_2\text{CuO}_7$  and (b)  $\text{Pr}_2\text{Ba}_4\text{Cu}_8\text{O}_{16}$  which is the double layer compound. The unit cell for (b) is twice as large as the formula unit, with chemical composition  $\text{Pr}_2\text{Ba}_4\text{Cu}_8\text{O}_{16}$  [94]

In addition, Toshiyuki Usagawa *et al.*, [19] claimed to have observed superconductivity on oriented PrYBCO films grown on YBCO single crystal substrates.

An interesting paper was published by Zou *et al.* [20]. This group reported to have been able to enhance the  $T_C$  of the PrYBCO when pressure up to 14 GPa is applied. They made a comparison of an orthorhombic superconducting YBCO without Pr with a Pr doped YBCO at the Y site (PrYBCO) and found changes in their  $T_C$ 's respectively. The transition temperature of the orthorhombic superconducting YBCO without Pr decreased and in contrast to the PrYBCO, the transition temperature increased up to 105 K when pressure is applied.

The mechanism by which  $T_C$  is being decreased or increased by Pr or other compounds doping of the orthorhombic superconducting YBCO sample is still controversial and not well understood. Chapter 4 of this thesis will introduce some of the proposed models.

### 3.2 Photodoping Semiconducting YBCO Samples

Kudinov *et al.* [21] photodoped a semiconducting  $YBCO_{6+x}$  film with oxygen content  $x \sim 0.4$ . They showed that photoinduced superconductivity and persistent photoconductivity in a semiconducting YBCO film can be done by illumination with visible light, which led to a transition from the semiconducting to superconducting states. Soon after Kudinov's experiment on the transport properties of semiconducting film, Osquiguil *et al.* [22] examined a range of oxygen concentration of the  $YBCO_{6+x}$  from  $x \sim 0.4$  up to  $x = 7$ . They found persistent photoinduced effects for the entire oxygen range in the system and also showed that the variation with oxygen content of the total

photoinduced enhancement of  $T_C$  and of the  $T_C$  enhancement due to oxygen ordering are similar in agreement with [21].

Another group Kawamoto *et al.* [23] studied the transport properties of a YBCO thin film sample with  $x=0.3$  by laser radiation below room temperature, they obtained a structural change that suggests a transition into an orthorhombic like state, which means a contraction in the distance between the apical oxygen and the CuO (2) plane [24]. They claimed that this may be caused by the reordering of the oxygen atoms in the basal plane induced by photoirradiation.

In recent work by Widder *et al.* [25], they investigated oxygen ordering and persistent photodoping in tetragonal YBCO<sub>6+x</sub> with  $x=0.1$  and  $0.2$  respectively. For the first time, they studied the persistent photoconductivity (PPC) effects on tetragonal YBCO samples with low oxygen concentration. Their results were in strong agreement with the idea of insulator-metal transition which is driven by a percolation process. In order to conclude this section, it is important to emphasize that, photodoping YBCO thin film samples with low oxygen by illumination, increases the concentration of carriers (free holes) which leads to similar effects in transport and magnetic properties as would result from increasing the oxygen content of the material. Federici *et al.* [25(a)] performed photodoping YBCO samples in the metal-insulator transition with oxygen concentration ranging from  $X=6.2-6.4$ . For comparison purposes they also photodoped a fully oxygenated (superconducting) YBCO and found no changes in the resistance and the luminescence spectra since there are no available vacancies to trap photogenerated electrons. Based on optical, transport and structural measurements a model of persistent photoconductivity (PPC) was suggested which incorporates both photogenerated

electrons trapped at defects (oxygen vacancies) and structural rearrangement in the basal plane in which the trapping of electrons is a precursor to structural rearrangement.

### 3.3 Pressure Effects on Superconductivity

Since the discovery of superconductivity, pressure experiments have been investigated by several groups on both type I and type II superconductors. Ishizuka *et al.* [26] reported the pressure dependence of the transition temperature ( $T_C$ ) of vanadium up to 120 GPa, from their results they found a linear dependence of  $T_C$  as a function of applied pressure. The  $T_C$  of vanadium increased significantly as pressure was increased (Fig. 2, ref. 26). The susceptibility measurements of vanadium at 120 GPa showed the highest transition temperature with  $T_C = 17.2$  K. Anomalies in  $T_C$  were observed in niobium, between 5-6 GPa and 60-70 GPa the  $T_C$  increases by 0.7 K in agreement with [26] and decreases by 1 K respectively [27]. Soon after the discovery of superconductivity in type II YBCO system, pressure measurements were achieved using a He gas as pressure medium up to 8 Kbar by [28]. They found the  $T_C$  to change as pressure was increased [26, 27]. Another superconducting material  $\text{La}_{2-x}\text{Sr}_x\text{CuO}_4$  (LSCO) system was studied under pressure. It is known that in the LSCO system, superconductivity, takes place mainly in the orthorhombic phase. Fujita *et al.* [29] applied a non-hydrostatic pressure so as to compress the  $a$ - $b$  plane and eventually to expand the  $c$ -axis, they were able to enhance the transition temperature  $T_C$  up to 52 K at 8 GPa in tetragonal LSCO with Sr concentration  $x = 0.5$ .

Also pressure dependence of  $T_C$  was performed on the newly discovered  $MgB_2$  superconductor [30], in contrast to Ref. [26, 27, 28, 29] the  $T_C$  decreased significantly up to 1.35 GPa [31].

### 3.4 Effect of Defects on Superconductivity

Effects of defects on superconductivity have been studied since the discovery of type I and type II superconductors. Several groups have investigated the role that stacking faults, ionic vacancies, grain boundaries and other crystal defects play in determining the superconducting properties of high temperature superconductors (HTSC).

In early 1990's, physicists and material scientists had their focus on the type of interaction that exists between substrates and superconducting thin films deposited on them; how a given substrate can affect crystal structures of the films.

Experiments have shown in superconducting YBCO thin films, that the transition temperature of these films decreased significantly when their thicknesses were reduced below 100 Å. Such an experiment was carried out by Li *et al.* [32], they studied a superconducting YBCO thin film deposited on a PrYBCO substrate. They claimed that the reason why they have used the PrYBCO as a substrate is that, it has an orthorhombic structure with lattice parameters close to the YBCO system; providing a much better lattice match than any other substrate to YBCO and also because it is a non superconductor with a very high resistivity at low temperatures. Their results showed the resistivity to drop as the thickness of the superconducting YBCO thin film was varied. This dependence of  $T_C$  on the layer thickness can be attributed to microscopic defects introduced by the multiplayer growth if they are not minimized, proximity effects,

interdiffusion and mechanical shorting between the conducting layers are still possible [32, 33]. In plane pressure effect in strained  $\text{YBCO}_7/\text{La}_{1.85}\text{Sr}_{0.15}\text{CuO}_4$  superlattices on MgO (100) substrate was investigated by Horiuchi *et al.* [34], they stacked layers of thin film YBCO on top of the LSCO layers then deposited them on the MgO (100) substrate. In agreement with [32, 33], they found the crystal structure to change when the layers of the YBCO thin films were varied while the LSCO layers were fixed.

### 3.5 Halogenation of YBCO Samples

Exposure of insulating non superconducting YBCO samples to halogens was performed for the first time by Osipyan *et al.* [49 (a)]. They reported a critical temperature ( $T_C$ ) of 90-92 K and an orthorhombic phase formed by exposing initially tetragonal,  $x \sim 0$ , YBCO samples to gaseous chlorine. Further work by this group showed that exposure to  $\text{Br}_2$  and  $\text{I}_2$  resulted in the recovery of superconductivity [49 (b)]. Recently, Potrepka *et al.* [57] investigated the local atomic structure (about Cu and Br) using  $^{63,65}\text{Cu}$  nuclear quadrupole resonance (NQR) and  $^{79,81}\text{Br}$  nuclear magnetic resonance (NMR) on well-characterized powder samples of parent, deoxygenated, and brominated YBCO. The NMR signal for the Cu(2) peak in brominated samples was found to be broadened compared to that in the parent materials. Potrepka *et al.* also performed low temperature Br *K*-edge XAFS measurements [57] and argued that Br did not enter the lattice substitutionally or interstitially. XAFS spectra were found to be similar to those of  $\text{BaBr}_2$  powder. They suggested that bromination led to  $\text{BaBr}_2$  precipitation as nano-particles which gave rise to the higher background seen in XRD. Unfortunately, model fitting of the XAFS spectrum was not performed and hence details of the local structure about Br remained unknown.

In contrast to [57]. In this thesis we have performed systematic multiple edge x-ray absorption fine structure (XAFS) measurements on both normal (non-brominated) and brominated YBCO samples. We also proposed a fitting model in order to ascertain the location of the bromine and iodine atoms in the YBCO sample.

### **3.6 Influence of Local Structure on Superconductivity**

#### **3.6.1 Purpose of Studying Local Atomic Structure Using X-ray Absorption Fine Structure Spectroscopy**

The long range periodic structure of HTSC materials has been well studied. However, much less work has been done on the local structure. In this thesis work, we will provide a quantitative characterization of local distortions about Br, I, Cu, Ba, Y sites for the brominated (non-brominated) and iodinated (non-iodinated) YBCO single crystals. Further, our multiple-edge XAFS results on the YBCO single crystals are compared with well known diffraction data.

#### **3.6.2 Long Range Structural Anomalies (X-ray Diffraction )**

Shafer *et al.* [76] investigated single phase superconducting  $\text{YBCO}_{6.9}$  by high resolution neutron powder diffraction in the temperature range from 16 to 300 K. In their experiments, they extracted parameters such as cell parameters, bond lengths and atomic thermal vibrations which contain information about structural effects as a function of temperature with several anomalies near  $T_C$ . They claimed to have found distinct structural anomalies for YBCO (123) near  $T_C$  thus corroborating significantly strong correlations between crystal structure and superconductivity. They stated in their conclusion that the ground state of the system is reached near  $T_C$  and that thermal

expansion saturates. The structural anomalies are concerned with the copper–oxygen system these are: 1). Discontinuous lattice contraction with a stretching of Cu(2)-O(3), 2). Discontinuous change of the Cu(1)-O(4) bond length affecting the structural link between chains and layers in the superconducting state, 3). Discontinuous behavior of the thermal vibrational parameters of the chain constituent atoms. (see Fig. 5, 6 in ref. 76). Further more, a neutron diffraction study was performed on YBCO (123) single crystals by Schweiss *et al.* [96], from their data analysis they found a good agreement between the measured and the calculated mean-square displacements. No evidence of an anharmonic dynamic of the apical oxygen along the c-axis which contradicts EXAFS results [84]. However, an anharmonic effect of this oxygen (apical) was observed parallel to the a-b planes. Another group [78] claimed to have observed an anharmonic behavior of the apical oxygen which is in agreement with *some* EXAFS analysis [84,87]. Further, Casalta *et al.* [79] found their results to be in good agreement with [77] but in disagreement with powder data [80] which is an indicative of controversy within the diffraction community as well.

### 3.6.3 Short Range Structural Anomalies (X-ray Absorption Fine Structure, XAFS)

Zhang *et al.* [81], studied the temperature dependence of YBCO (123) superconductor, CuO and BaO using the x-ray absorption fine structure technique. They found the Einstein model at low temperatures unsatisfactory for both the YBCO and CuO as it is at high temperatures since the phonons are dominant at low temperatures. However the large deviations from the model for the Cu-O are unexpected, especially around  $T_C$ . From their temperature dependence XAFS analysis, they concluded that their findings are



consistent with the idea that soft phonon modes are persistent for the Cu-O atomic pairs in the low temperature range for both the superconductor and CuO. These observations reflect the inadequacy of the Einstein model for the oxides. In Contrast to [81, 82], Yang *et al.* [83] performed polarized XAFS measurements on well oriented YBCO samples, they found no evidence of softening of phonon modes connected with longitudinal stretching of Cu-O and Y-X (X=O, Cu, Ba, and Y) bonds. They suggested that strong electron-phonon coupling is incompatible with their experimental evidence of no anomalous temperature dependence of the Debye-Waller factor and high effective vibrational frequencies for Cu-O pairs in the superconductor. Also they found no evidence of Cu and Y anti-site disorder in the superconductor. Further studies about structural anomalies near the transition temperature were performed by J. Mustre de Leon *et al.* [84], using XAFS techniques. They studied the temperature dependence of a thin slice of YBCO<sub>7</sub> oriented powder and found structural anomalies around the Cu-O pairs which is in agreement with other experiments performed on high temperature copper oxide superconductors [85, 86]. Two years latter, this same group lead by J. Mustre de Leon *et al.* [87] performed temperature dependence XAFS measurements on a well oriented YBCO<sub>7</sub> sample. Because of the linear polarization of the x-ray from the synchrotron radiation, they measured the Cu *K*-edge polarized XAFS. From their XAFS results, they claimed to have observed an anharmonic behavior of the Cu-O pairs near the transition temperature and a double well potential model was used to describe the anomaly.

X-ray Absorption Fine Structure measurements have been done as well on (PBCO) samples, Booth *et al.* [88] performed XAFS measurements on the

superconducting YBCO with Y being replaced by Pr. They studied a set of the Pr concentrations in the superconducting YBCO material to understand the reason why the transition temperature is significantly suppressed. They compared the Fourier Transforms of the multiple edges of the Pr doped YBCO, and were able to ascertain the dominant site for the Pr substitution. From their Fourier Transform spectra, they found the location of the oxygen and copper peaks in the Pr doped YBCO (PBCO Pr *K*-edge) is very similar to that around Y in the YBCO (Y *K*-edge). This indicates that most of the Pr substitutes at the Y site with an electronic valence state ( $\text{Pr}^{+3}$ ). Harris *et al.*, performed XAFS measurements on a non-superconducting PBCO, they found that Pr occupies the Y sites which contradict Ba-sites substitution. Booth *et al.* [89] studied YBCO thin films deposited on MgO substrates using XAFS techniques. They performed temperature dependence of the XAFS from 20-200 K; from their results they claimed that the O(4) peak can be described by a single-site, harmonic distribution. This distribution does not show any strongly anharmonic behavior with temperature near  $T_C$ , or at any other temperature between 20-200 K. J. H. Han *et al.* [90], also studied the Pr doped YBCO system using x-ray absorption fine structure techniques, they found that as the Pr concentration is increased, the Ba-O(3) bond distance increased with decreasing  $T_C$  which is in agreement with [88]. Another well-known techniques in x-ray absorption fine structure, is the energy-dispersive XAFS technique that allows to collect several absorption spectra in few seconds. The advantage of the energy-dispersive XAFS technique over other techniques is that, one can collect a wide range of temperature dependence XAFS spectra with relatively small temperature steps. Wu *et al.* [91], studied

local distortions about Th in crystalline oxide-type compounds using the energy-depressive XAFS technique.

### **3.7 Other Type of Transport Measurements and Existence of Anisotropy in Superconducting YBCO Samples**

Resistivity measurements were performed along both the *a-b* and *c* directions [92]. They found the resistivity along the *a-b* directions to be approximately  $450 \mu\Omega\text{cm}$  decreasing linearly with temperature above the superconducting transition. In contrast to the *c* direction resistivity measurements, the resistivity was found to be 30 times larger than in the *a-b* directions with a weak temperature dependence confirming the highly anisotropic nature of the material (Fig.3 in ref. 93). Next chapter will be focused on the BCS theory and on some of the models introduced by different research groups in understanding mechanisms responsible for superconductivity.

## CHAPTER 4

### THEORY OF SUPERCONDUCTIVITY

#### 4.1 Background of Theory of Superconductivity

Since the discovery of superconductivity in mercury (see Chapter 1), several attempts have been made by scientists then to explain this unusual phenomenon of matter at low temperatures. A major discovery came few decades later, when in 1933, Walter Meissner and Robert Ochsenfeld discovered that a superconducting material will expel a magnetic field. In 1935, H. London and F. London, proposed a phenomenological theory of the electromagnetic properties. F. London, suggested a quantum theoretic approach to a theory in which it was assumed that there is somehow a coherence or rigidity in the superconducting state such that the wave functions are not modified very much when a magnetic field is applied. A. B Pippard expanded on the concept of coherence, on the basis of experiments on penetration phenomena, he proposed a non local modification of the London equation in which a coherence distance  $\xi_0$  is introduced.

It was pointed out that an energy gap model will lead to the Pippard version, and this was found to be true for the BCS theory of superconductivity. The BCS theory of diamagnetic thus follows along the general lines suggested by London and Pippard. Also in 1928, the Sommerfeld-Bloch individual-particle model was able to give a good description of normal metals, but fails to account for superconductivity.

In the BCS theory, the strong electron correlations were neglected and assumes that each individual electron moves independently in some sort of self-consistent field determined by the other conduction electrons and the ions. Later, W. Heisenberg and H.

Koppe proposed a theory based on long wave-length components of the Coulomb interaction, which were presumed to give fluctuations in the electron density described by wave packets localizing a small fraction of the electrons on lattices moving in different directions.

The discovery of the isotope effect by Reynolds, Serin, Wright and Nesbit [35] strongly indicated as it was independently suggested by Frohlich [36], that electron phonon interactions are responsible for superconductivity. We now discuss the details of the BCS theory of superconductivity.

## 4.2 BCS Theory and Ground State Energy

In the BCS theory [37, 38], the Hamiltonian is most conveniently expressed in terms of creation and annihilation operators, based on the renormalized Bloch states specified by wave vector  $k$  and spin  $\sigma$ , which satisfy Fermi commutation relations.

The commutation relations for the creation and annihilation operators are given in the following:

$$[c_{k\sigma}, c_{k'\sigma'}^*]_{\pm} = \delta_{kk'} \delta_{\sigma\sigma'} \quad (4.1)$$

$$[c_{k\sigma}, c_{k'\sigma'}]_{\pm} = 0 \quad (4.2)$$

where  $c_{k\sigma}$  and  $c_{k\sigma}^*$  are the annihilation and creation operators respectively. The single-particle number operator can be introduced and is defined as:

$$n_{k\sigma} = c_{k\sigma}^* c_{k\sigma} \quad (4.3)$$

therefore the Hamiltonian for the electrons can be written:

$$\begin{aligned}
H &= \sum_{k \langle k_F} \varepsilon_k n_{k\sigma} + \sum_{k \langle k_F} |\varepsilon_k| (1 - n_{k\sigma}) + H_{coul} + \frac{1}{2} \sum_{k, k', \sigma, \sigma', \kappa} \frac{2\hbar\omega_\kappa |M_\kappa|^2 c^*(k' - \kappa, \sigma') c(k', \sigma') c^*(k + \kappa, \sigma) c(k, \sigma)}{(\varepsilon_k - \varepsilon_{k+\kappa})^2 - (\hbar\omega_\kappa)^2} \\
&= H_0 + H_I
\end{aligned} \tag{4.4}$$

where  $\varepsilon_k$  is the Bloch energy measured relative to the Fermi energy,  $k \rangle k_F$  and  $k \langle k_F$  represent states above and below the Fermi surface respectively. The last term in equation 4.4 is the phonon interaction, which comes from virtual exchange of phonons between electrons and  $M_\kappa$  is the electron phonon matrix of interaction calculated for zero point amplitude of the lattice vibrations given by:

$$|M_k|^2 = |v_x|^2 \left( \frac{\hbar}{2\omega_\kappa} \right) \tag{4.5}$$

$|M_k|^2$  varies with isotopic mass in the same way that  $\omega_\kappa$  does, therefore the ratio  $\frac{|M_k|^2}{\hbar\omega_\kappa}$  is independent of isotopic mass. BCS suggested an attractive (negative) phonon interaction for excitation energies given as:

$$|\varepsilon_k - \varepsilon_{k+\kappa}| \langle \hbar\omega_\kappa \tag{4.6}$$

for superconductivity to take place, the attractive phonon interaction is suppose to dominate the coulomb one. They also showed that, the most important transitions are those for which

$$|\varepsilon_k - \varepsilon_{k+\kappa}| \sim KT_c \langle \hbar\omega_\kappa \tag{4.7}$$

where  $K$  is the Boltzman constant and  $T_c$  is the transition temperature.

To obtain the ground state function, they observed that the interaction Hamiltonian connects a large number of nearly degenerate occupation number

configurations with each other via nonzero matrix elements. In fact, L. N. Cooper [37] solved a problem in which two electrons with zero total momentum interact via constant negative matrix element in a small shell above the Fermi surface.

In the actual problem, the interaction which takes a pair from  $(k_1\sigma_1, k_2\sigma_2)$  to  $(k_1'\sigma_1, k_2'\sigma_2)$  contains the following operators:

$$c^*(k_2', \sigma_2) c(k_2, \sigma_2) c^*(k_1', \sigma_1) c(k_1, \sigma_1) \quad (4.8)$$

from conservation of momentum one can write the following

$$k_1 + k_2 = k_1' + k_2' \quad (4.9)$$

It was shown that interaction conserves momentum, and a maximum number of matrix elements can be obtained if all pairs have the same net momentum.

$$q = k_1 + k_2 \quad (4.10)$$

All pairs were taken with opposite spin, since the exchange term reduces the interaction for parallel spins and the best choice for  $q$  for the ground state pairing was chosen to be

$$q = 0 \quad (4.11)$$

equation 4.11 represent a state if  $k$  is occupied so is  $-k$  occupied ( $k\uparrow, -k\downarrow$ ).

Then, BCS introduced the idea of a reduced problem, in which all the states are occupied in pairs such that if  $k$  is occupied so is  $-k$ .

In order to obtain a reduced Hamiltonian, creation and annihilation operators for pairs were introduced and defined in terms of single particle operators

$$b_k = c_{-k\downarrow} c_{k\uparrow} \quad (4.12)$$

$$b_k^* = c_{k\uparrow}^* c_{-k\downarrow}^* \quad (4.13)$$

the commutation relations for the creation and annihilation operators can be written in the following:

$$[b_k, b_{k'}^*] = (1 - n_{k\uparrow} - n_{-k\downarrow}) \delta_{kk'} \quad (4.14)$$

$$[b_k, b_{k'}] = 0 \quad (4.15)$$

$$[b_k, b_{k'}]_{\pm} = 2b_k b_{k'} (1 - \delta_{kk'}) \quad (4.16)$$

where  $(1 - n_{k\uparrow} - n_{-k\downarrow})$  and  $(1 - \delta_{kk'})$  arise from the Pauli exclusion principle on single particles.

Using equation 4.4 and the creation and annihilation operators for pairs with zero net momentum which are expressed in terms of single particle operators, they derived the following Hamiltonian:

$$H = 2 \sum_{k \in k_F} \varepsilon_k b_k^* b_k + 2 \sum_{k \in k_F} |\varepsilon_k| b_k b_k^* - \sum_{kk'} V_{kk'} b_{k'}^* b_k \quad (4.17)$$

in 4.17, the interaction term is defined with a minus sign so  $V_{kk'}$  is always positive for superconductors.

The wave function was introduced using the Hartree-like approximation

$$\Psi = \prod \left[ (1 - h_k)^{\frac{1}{2}} + h_k^{\frac{1}{2}} b_k^* \right] \Phi_0 \quad (4.18)$$

where  $\Phi_0$  is the vacuum.

Now, for any specified wave vector  $k'$ , it is convenient to decompose  $\Psi$  into two components, in one of which  $\varphi_1$  the pair state designated by  $k'$  is occupied and  $\varphi_0$  for which it is empty.



$$\Psi = h_k^{\frac{1}{2}} \varphi_1 + (1 - h_k)^{\frac{1}{2}} \varphi_0 \quad (4.19)$$

From the Hartree-like approximation, the coefficient  $h_k$  is the probability that state  $k$  is occupied and the  $\varphi$ 's are the normalized functions

The wave function (4.19) can be generalized to N pairs of particles, then 4.19 becomes

$$\Psi_N = h_k^{\frac{1}{2}} \varphi_{N1} + (1 - h_k)^{\frac{1}{2}} \varphi_{N0} \quad (4.20)$$

where the  $\varphi_N$ 's are also normalized functions. In terms of two pair states for N particles the wave function can be written in the following:

$$\Psi_N = (hh')^{\frac{1}{2}} \varphi_{N11} + [h(1-h')]^{\frac{1}{2}} \varphi_{N10} + [(1-h)h']^{\frac{1}{2}} \varphi_{N01} + [(1-h)(1-h')]^{\frac{1}{2}} \varphi_{N00} \quad (4.21)$$

where the first index in  $\varphi$  gives the occupancy of  $k$  and the second of  $k'$ .

The ground state energy relative to the Fermi surface is given in terms of 4.21 used as a variational approximation to the ground state function by the following:

$$W_0 = (\Psi_0 H_1 \Psi_0) \quad (4.22)$$

where  $\Psi_0$  is the N pair function  $\Psi_N$  for the ground state.

It is important to mention that all the Bloch energies  $\varepsilon_k$  are measured with respect to the Fermi energy and

$$-V_{kk'} = (-k' \downarrow, k' \uparrow | H_I | -k \downarrow, k \uparrow) + (k' \uparrow, -k' \downarrow | H_I | k \uparrow, -k \downarrow) \quad (4.23)$$

The kinetic energy corresponding to the ground state is:

$$W_{KE} = 2 \sum_{k < k_F} \varepsilon_k h_k + 2 \sum_{k < k_F} |\varepsilon_k| (1 - h_k) \quad (4.24)$$

where KE stands for kinetic energy and also the contribution to the interaction term can be written:

$$W_I = -\sum_{k,k'} V_{kk'} [h_k(1-h_k)h_{k'}(1-h_{k'})]^{1/2} \quad (4.25)$$

the total ground state energy can be expressed in terms of 4.24 and 4.25

$$W_0 = W_{KE} + W_I \quad (4.26)$$

Minimizing the ground state energy 4.26 with respect to  $h_k$ , BCS obtained an integral equation which determines the distribution function and also neglected the anisotropic effect. They also assumed the matrix element  $V_{kk'}$  to be an average matrix element.

This averaging is valid only for pairs making transitions in the region  $-\hbar\omega < \varepsilon < \hbar\omega$  and zero outside this range of energy, where  $\omega$  is the average phonon frequency. This means simply that the BCS wave function is formed from states in the region where the interaction is expected to be attractive and not mixing in states outside of this region.

Differentiation the ground state with respect to  $h_k$  they were to obtain the following distribution function:

$$h_k = \frac{1}{2} \left[ 1 - \frac{\varepsilon_k}{(\varepsilon_k^2 + \varepsilon_0^2)^{1/2}} \right] \quad (4.27)$$

and

$$[h_k(1-h_k)]^{1/2} = \frac{\varepsilon_0}{2(\varepsilon_k^2 + \varepsilon_0^2)^{1/2}} \quad (4.28)$$

where

$$\varepsilon_0 = V \sum_k \left[ h_k (1 - h_k) \right]^{\frac{1}{2}} \quad (4.29)$$

combining 4.28 and 4.29 one obtains the following:

$$\frac{1}{V} = \sum_k \frac{1}{2(\varepsilon_k^2 + \varepsilon_0^2)^{\frac{1}{2}}} \quad (4.30)$$

Replacing the sum with an integral and also taking into account that  $V=0$  for  $|\varepsilon_k| > \hbar\omega$

then they obtained the following integral

$$\frac{1}{N(0)V} = \int_0^{\hbar\omega} \frac{d\varepsilon}{(\varepsilon^2 + \varepsilon_0^2)^{\frac{1}{2}}} \quad (4.31)$$

by integrating the right hand side and solving for  $\varepsilon_0$

$$\varepsilon_0 = \frac{\hbar\omega}{\sinh \left[ \frac{1}{N(0)V} \right]} \quad (4.32)$$

where  $N(0)$  is the density of the Bloch states for one spin per unit energy at the Fermi surface.

Substituting 4.27, 4.28 and 4.29 into the ground state energy then:

$$W_0 = 2N(0) \int_0^{\hbar\omega} \left[ \varepsilon - \frac{\varepsilon^2}{(\varepsilon^2 + \varepsilon_0^2)^{\frac{1}{2}}} \right] d\varepsilon - \frac{\varepsilon_{00}^2}{V} \quad (4.33)$$

they assumed that the distribution function is symmetric in electrons and holes with respect to the Fermi surface:

$$1 - h(-\varepsilon) = h(\varepsilon) \quad (4.34)$$

using 4.32 and by integrating 4.33 they obtained the ground state energy to be in the form

$$W_0 = \frac{-2N(0)(\hbar\omega)^2}{e^{\left[\frac{2}{N(0)V}\right]} - 1} \quad (4.35)$$

the criterion for superconductivity is that  $V$  is always positive.

From 4.35, the excitations smaller than  $\hbar\omega$  the phonon interaction is independent of isotopic mass and therefore the mass dependence of the ground state comes from  $(\hbar\omega)^2$  which is in agreement with the isotopic effect.

BCS assumed the product  $N(0)V$  to be less than 1, ( $N(0)V \ll 1$ ) which corresponds to the weak coupling limit therefore the ground state energy is in order of  $N(0)(KT_c)^2$  and  $KT_c$  is much less than  $\hbar\omega$ .

In the weak coupling limit, the ground state energy is found to be:

$$W_0 = -2N(0)(\hbar\omega)^2 e^{\left[-\frac{2}{N(0)V}\right]} \quad (4.36)$$

4.36 can be expressed in terms of number of electrons in pairs virtually excited above the Fermi surface as:

$$W_0 = \frac{-n_c^2}{N(0)} \quad (4.37)$$

where

$$n_c = 2N(0)\hbar\omega e^{\left[-\frac{1}{N(0)V}\right]} \quad (4.38)$$

Using the empirical order of magnitude between the ground state energy and  $KT_c$  then they estimated the following relation:

$$KT_c \sim \hbar\omega e^{\left[-\frac{1}{N(0)V}\right]} \quad (4.39)$$

4.39 is the empirical relation for the BCS theory. It expresses the transition temperature in terms of the vibrational frequency of the phonons which is in agreement with the isotope effect. BCS also obtained almost the same result for  $KT_c$  from the free energy as a function of temperature method [38].

### 4.3 Models of Superconductivity

The BCS theory discussed in section 4.2, is the first theoretical model to explain superconductivity in metals and also made a number of remarkable predictions [38].

The basic feature of the BCS theory is that the electron pairing occurs in states with opposite momentum and opposite spins, according to the Pauli exclusion principle for fermions the two spins are combined to form a singlet state with  $S=0$ . The choice for the singlet in their theory, is based on the fact that other choice of spin combination will lead to a triplet state with  $S=1$  which implies that the superconducting state has magnetic properties which are absent. Thus the choice for the singlet state with  $S=0$  is the most reasonable for the BCS theory. Later work by Balian *et al.* [39] who solved the BCS equations for the triplet state with  $S=1$ , showed that the triplet state had a smaller binding energy and was therefore less favored. Below are given strong interaction models.

#### 4.3.1 Model I : Spin Bag Mechanism of High Temperature Superconductivity

A new approach to high temperature superconductivity was proposed by Schrieffer *et al.*, [40] based on the two dimensional antiferromagnetic (AF) spin correlations observed in these materials. They showed how spin ordering was responsible for an opening near the

Fermi surface called a pseudo gap, whose value is significantly reduced in presence of a hole. A year later, this same group [41] published a paper on the spin bag mechanism of high temperature superconductivity. In their work, they reviewed the basic formalism of the spin density wave (SDW) approach to the Hubbard model and calculated the dynamical pairing potential between spin bags. Another approach to the spin bag mechanism and pseudogaps, were studied this time by Kampf and Shrieffer [41(a)] in the paramagnetic (PM) metal phase (higher values of doping  $x$ ) rather than in the antiferromagnetic (AF) phase (lower values of doping  $x$ ). They proposed a model susceptibility for the 2D single orbital Hubbard model on a square lattice with the following Hamiltonian:

$$H = -t \sum_{\langle ij \rangle \sigma} (c_{i\sigma}^* c_{j\sigma} + c_{j\sigma}^* c_{i\sigma}) + U \sum_i n_{i\uparrow} n_{i\downarrow} - \mu \sum_{i\sigma} n_{i\sigma} \quad (4.40)$$

where  $c_{i\sigma}^*$  and  $c_{i\sigma}$  are creation and annihilation operators for localized electron states of spin  $\sigma$  on site  $i$ , and  $\mu$  is the chemical potential. For a strong Coulomb repulsion  $U$ , the Hubbard model develops a strong antiferromagnetic correlations between spins on nearest neighbor sites. They suggested that at half-filling, the nesting property of the Fermi surface of the tight-binding band gives rise to a ground state instability leading to a spin density wave (SDW).

$$\varepsilon_{\mathbf{k}} = -2t(\cos k_x a + \cos k_y a) \quad (4.41)$$

This is valid only for the strong coupling limit when  $\frac{U}{t} \gg 1$ . It is known that in the presence of spin density wave (SDW) with a long range order [40, 42] a gap opens up in

the single particle spectrum in agreement with [40]. This pseudogap ( $\Delta_{SDW}$ ) is smaller in magnitude when  $U \ll t$  while in the strong coupling case  $\Delta_{SDW}$  is of order  $U$ . They also found that in the paramagnetic (PM) metal regime, the strong correlation of spins causes the density of states to show a depletion of spectral weight near the Fermi level reflecting the nearby instability to antiferromagnetic ordering.

In relation to the weak coupling case for superconductivity, this same bag effects was observed in charge density wave (CDW) superconductors like Ba (Pb,Bi)O<sub>3</sub> and possibly (Ba, K)BiO<sub>3</sub> which also leads to a pseudogap. Schrieffer *et al.* [41] found these charge bags due to CDW to be attractive and their spin fluctuations are coupled to phonons leading to a partial isotope effect. In conclusion, it is important to mention that the spin bag approach is still not well understood as a model for superconductivity therefore, a number of questions is needed to be answered which are the following:

Are the spin and the charge of the excitations correctly predicted in the antiferromagnetic and in the metallic phase?. What is the actual shape of Fermi surface in the metal and is the pairing order parameter free of nodes on the Fermi surface?. What is the influence of quantum fluctuations in the superconducting properties?. Can the bag approach account for the general experimental facts which are not subject to materials difficulties?. All these issues have to be well clarified in order to understand the bag mechanism.

#### 4.3.2 Model II: Magnetic Ordering in Superconductivity

Felix Yndurain [42] studied the interplay between the BCS theory and magnetic ordering in high temperature superconductors (HTSC), he extracted the following issues for his model:

- 1) The phase diagram for different doping doses is generally accepted, systems range upon doping, from antiferromagnetic insulator to a superconductor and to normal metal. And the boundaries between these regions being under question.
- 2) Superconductivity takes place mainly in the CuO<sub>2</sub> planes, interaction between planes and through the CuO chains being not negligible but for secondary importance.
- 3) Electron-phonon interaction plays definite but partial role in the superconducting phase.
- 4) Magnetism plays a very important role both below and above the superconducting critical temperature, the Cu atoms displaying a magnetic moment in the superconducting phase region.

In his work, his focus was toward the possibility of existence of magnetic ordering due to saddle point singularities near the Fermi energy in the electronic spectrum, and also on the enhancement of conventional BCS superconductivity due to high density of electronic states near the singularities. His model is based on the assumption that the origin of superconductivity is the electron-phonon interaction and can be described by the standard weak coupling BCS theory. He also assumed the electron-electron interactions to be large (magnetic ordering), only one CuO<sub>2</sub> plane is considered and a two dimensional density of electronic states corresponding to single band is assumed.

He then introduced the following Hamiltonian for his model:

$$H = H_0 + H_{e-ph} + H_{SDW} \quad (4.42)$$

where

$$H_0 = \sum_{k,\sigma} E(k) c_{k\sigma}^* c_{k\sigma} \quad (4.43)$$



and  $E(k)$  stands for the one electron energy band dispersion. The operators  $c_{k\sigma}^*$  create and  $c_{k\sigma}$  destroys an electron respectively with momentum  $k$  and spin  $\sigma$ . The  $H_{e-ph}$  term corresponds to the standard reduced BCS Hamiltonian which has the form:

$$H_{e-ph} = \sum_{k,\sigma,q} V(k,q) c_{(k+q)\sigma}^* c_{(-k-q)\sigma}^* c_{-k\sigma} c_{k\sigma} \quad (4.44)$$

where

$$V(k,q) = \begin{cases} -V_0, & |E_k - E_F| < \hbar\omega \text{ and } |E_{k+q} - E_F| < \hbar\omega \\ 0, & \text{otherwise} \end{cases} \quad (4.45)$$

where  $\hbar\omega$  is the Debye energy. For the electron-electron interaction, the Hubbard Hamiltonian was introduced to have the form:

$$H = \frac{U}{2} \sum_{k,k',\sigma} c_{k\sigma}^* c_{k'\sigma}^* c_{k'\sigma} c_{k\sigma} \quad (4.46)$$

with such a Hamiltonian, the superconducting order parameter takes the form:

$$\Delta(k) = \begin{cases} \Delta_2 - \Delta_1, & |E_k - E_F| < \hbar\omega \\ -\Delta_1, & \text{otherwise} \end{cases} \quad (4.47)$$

where

$$\Delta_2 = V \sum_k' \langle c_{k\sigma}^* c_{-k\sigma} \rangle \quad (4.48)$$

$$\Delta_1 = U \sum_k \langle c_{k\sigma}^* c_{-k\sigma}^* \rangle \quad (4.49)$$

the prime in the sum indicates that only states with energy from the Fermi level within the Debye temperature should be considered. For a constant density of state and without magnetic ordering, he obtained the well known McMillan's expression for the critical temperature:

$$KT_c = 1.13\hbar\omega \exp \left[ \frac{-1}{V_0\rho - \frac{1}{\left(\frac{1}{U\rho}\right) + \ln\left(\frac{W}{\hbar\omega}\right)}} \right] \quad (4.50)$$

where  $\rho$  is the density of states at the Fermi level and  $\hbar\omega$  the Debye energy and the interplay between the electron-phonon and electron-electron interactions is obvious in 4.50. It is well known that in a two dimensional electron band there is always a saddle point that give rise to a logarithmic singularity in the density of states which produces magnetic ordering (SDW) [42].

In order to take into account the presence of magnetic ordering, he considered the presence of SDW in addition to superconductivity with an order parameter which is given by:

$$\gamma = U \sum_k \langle c_{k\sigma}^* c_{k+Q\sigma} \rangle \quad (4.51)$$

He solved the Hamiltonian 4.42 in the mean field approximation by means of canonical transformation assuming that two saddle points are connected by a Q vector, commensurate or not with the lattice, leaving the form of the band dispersion unspecified. Then from his calculations, he concluded the following:

1) Superconductivity and magnetic ordering can coexist below  $T_C$ , the electron-electron and electron-phonon interactions compete with each other and a mixed ground state takes place with two symmetries simultaneously broken.

2) The superconducting gap  $\Delta_2 - \Delta_1$  decreases near  $T_C$  faster than in the pure BCS case.

This is due to the fact that both of the order parameters of superconductivity and spin density wave are competing with one another. When superconductivity decreases by a

temperature effect the other SDW overcomes it, at the same time the SDW order parameter has its largest value at the superconducting critical temperature.

3) Above  $T_C$  there is a pure SDW magnetic ordering up to a critical temperature  $T_s$  where the magnetic ordering is destroyed. The electrons responsible for the formation of cooper pairs are the ones also responsible for magnetic ordering. But in BCS theory it is known that, the cooper pairs are formed by electrons with opposite momentum and spin (spin orientation depends on position).

#### **4.3.3 Model III: Variation of the Isotope Coefficient for HTSC Upon Doping**

This model is based on the coexistence between the conventional BCS type superconductivity and magnetic correlations [42], then extended to analyze the isotope effect with the hole concentration. This model is a continuation of model two described above. Felix Yndurain [43] considered a model two-dimensional system to describe the  $\text{CuO}_2$  planes such that the Fermi energy lies close to saddle point of the non-interacting electronic bands.

Several results have shown that, the electron-phonon coupling gives rise to both the conventional BCS theory and the charge density wave (CDW). On the other hand, when the strong electron-electron interaction is taken into account, it may produce what is called the spin density wave (SDW). The later interaction caused by the electrons alone, has a tendency to destroy superconductivity. Therefore, Felix Yndurain investigated the competition and possible cooperation between these broken symmetries in high temperature superconductivity.

He introduced for his model the following Hamiltonian, which contains the one electron, the electron-electron and the electron-phonon Hamiltonians:

$$H = H_0 + H_{e-ph} + H_{e-e} \quad (4.52)$$

where the one electron Hamiltonian is given by:

$$H_0 = \sum_{k,\sigma} E(k) c_{k\sigma}^* c_{k\sigma} \quad (4.53)$$

$E(k)$  is the one-electron band dispersion at the  $\text{CuO}_2$  planes and  $c_{k\sigma}^*$  ( $c_{k\sigma}$ ) represents the creation (annihilation) operator of electrons with momentum  $k$  and spin  $\sigma$ . The electron phonon interaction is approximated by the BCS expression:

$$H_{e-ph} = \sum_{k,q,\sigma} V(k,q) c_{(k+q)\sigma}^* c_{(-k-q)\sigma}^* c_{-k\sigma} c_{k\sigma} \quad (4.54)$$

The electron-electron part of the Hamiltonian is assumed to be the following Hubbard like form:

$$H_{e-e} = \frac{U}{2} \sum_{k,k',\sigma} c_{k\sigma}^* c_{k'\sigma}^* c_{k'\sigma} c_{k\sigma} \quad (4.55)$$

He approximated the Hamiltonian to be as in model II in this thesis:

$$H = H_0 + H_{sc} + H_{SDW} \quad (4.56)$$

where  $H_{sc}$  is similar to the BCS Hamiltonian which has the form:

$$H_{BCS} = -\Delta \sum_k' (c_{k\sigma}^* c_{-k\sigma'}^* + c_{-k\sigma'} c_{k\sigma}) + \frac{\Delta^2}{V_0} \quad (4.57)$$

the prime on the sum for the BCS Hamiltonian indicates that, the summation is restricted to the states such that

$$|E(k) - E_F| < \hbar\omega_D \quad (4.58)$$

For such Hamiltonian (BCS), the superconducting order parameter  $\Delta$  is energy dependent and it has the following form:

$$\Delta[E(k)] = \begin{cases} \Delta_2 - \Delta_1, |E(k) - E_F| < \hbar\omega_D \\ -\Delta_1, \text{otherwise} \end{cases} \quad (4.59)$$

where

$$\Delta_2 = V_0 \sum_k \langle c_{k\sigma}^* c_{-k\sigma'} \rangle \quad (4.60)$$

$$\Delta_1 = U \sum_k \langle c_{k\sigma}^* c_{-k\sigma'} \rangle \quad (4.61)$$

He then introduced the Hamiltonian for the SDW to be in the form:

$$H_{SDW} = -\gamma \sum_{k\sigma} c_{k\sigma}^* c_{k+Q\sigma'} + \frac{\gamma^2}{U} \quad (4.62)$$

where the spin density wave order parameter is given by:

$$\gamma = U \sum_{k\sigma} \langle c_{k\sigma}^* c_{k+Q\sigma'} \rangle \quad (4.63)$$

He calculated the phase diagram at  $T=0$  and for  $x=0.1$ , for possible different ground states depending on the values for the electron-electron and electron-phonon interact parameters. (See Fig.4.1)

From his phase diagram (Fig.4.1) on the electron-electron and electron-phonon interactions, it is noticeable that a large  $U$  parameter gives the formation of a spin density wave state which tends to suppress superconductivity. On the other hand, large values of  $V_0$  enhance the superconducting state and destroys spin density wave. Another case is when both parameters are small enough, both broken symmetries destroy each other and give rise to a new phase which is called the paramagnetic phase. In contrast to the small

values of the parameters, for their large values both superconductivity and spin density wave coexist in a large portion of the phase space. In conclusion, he presented a model which qualitatively accounts for the anomalous variation of the isotope effect when doping high  $T_C$  superconductors. From his results, he suggested that this anomalous behavior is due to the coexistence of both spin density wave (SDW) and superconductivity.

#### 4.3.4 Model IV: Frohlich Coulomb Model for High Temperature Superconductivity.

In contrast to the BCS theory of superconductivity, Alexandrov *et al.* [44] argued that a consistent theory of HTSC should include both the long range Coulomb repulsion between the carriers and the strong long-range electron phonon interaction. In their work, they proposed an analytically solvable multi-polaron model of high temperature superconductivity that takes into account these realistic long range interactions. The long range Coulomb repulsion is critical in ensuring that the carriers would not form large clusters. They also claimed that, in order to form stable pairs (bipolarons) the electron phonon interaction has to be strong enough to overcome the Coulomb repulsion at short distances. Since the electron phonon interaction is long range there is a potential possibility of clustering [44]. The Hamiltonian for Frohlich-Coulomb model contains, the electron kinetic energy, the infinite range Coulomb and electron phonon interactions as well as the lattice energy has the following form:

$$\begin{aligned}
 H = & - \sum_{n \neq n'} T(n-n') c_n^* c_{n'} + \sum_{n \neq n'} V_c(n-n') c_n^* c_{n'} c_n^* c_{n'} \\
 & - \omega \sum_{nm} g_\alpha(m-n) (e_{m\alpha} u_{m-n}) c_n^* c_n (d_{m\alpha}^* + d_{m\alpha}) + \omega \sum_{m\alpha} \left( d_{m\alpha}^* d_{m\alpha} + \frac{1}{2} \right)
 \end{aligned} \tag{4.64}$$

where  $c_n$  are the spinless fermion operators and  $d_{m\alpha}$  phonon operators. The electron phonon term is in real space rather than in momentum space,  $e_{m\alpha}$  is the polarization vector of  $\alpha^{\text{th}}$  vibration coordinate at site  $m$ ,  $u_{m-n} = \frac{m-n}{|m-n|}$  is the unit vector from electron  $n$  to the ion  $m$ , and  $g_\alpha(m-n)$  is the dimensionless electron-phonon coupling function in 4.64.

They concluded that, low Fermi energy and the strong unscreened coupling of carriers with high frequency optical phonons is the origin of high temperature superconductivity.

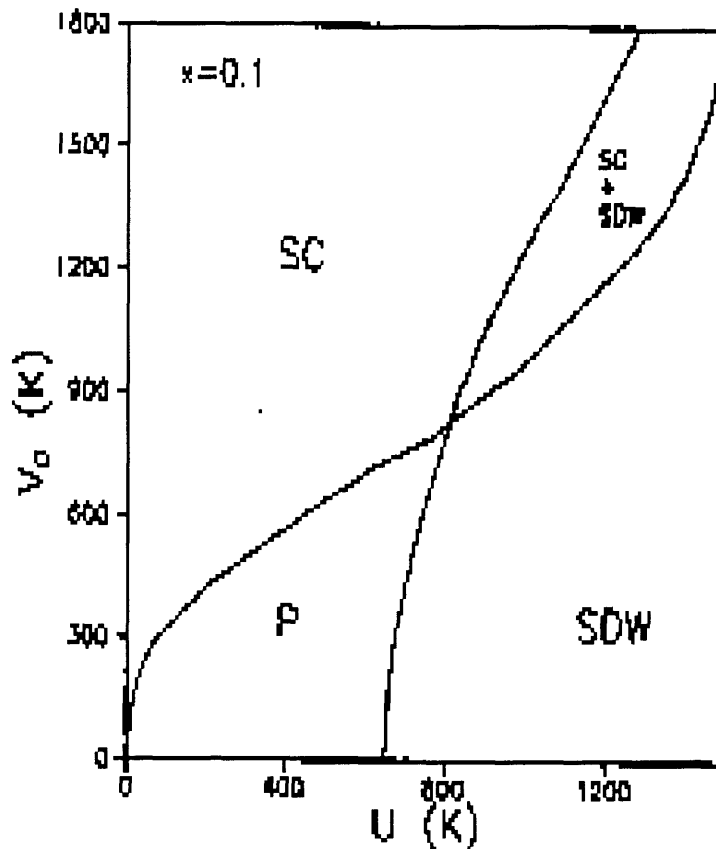


**Figure. 4.1** Phase diagram for the electron-electron and electron-phonon interaction parameters at  $T=0$  and hole occupation  $x=0.1$ . Coexistence and annihilation of superconductivity (SC) and SDW is shown. The phase P is the paramagnetic phase produced by the annihilation of superconductivity by the electron-electron interaction [43].

## CHAPTER 5

### X-Ray ABSORPTION FINE STRUCTURE (XAFS) SPECTROSCOPY

#### 5.1 Theory of XAFS

##### 5.1.1 Theory of Extended X-ray Absorption Fine Structure (EXAFS)

The extended x-ray absorption fine structure (EXAFS) is the fine structure in the x-ray absorption coefficient that usually starts 30 eV from above the absorbing atom edge and extends to about 1000 eV further. Some of the fundamental properties of EXAFS are the following: 1) Long range order is not required, it probes only the local atomic structure for short range atomic arrangement. 2) the local atomic arrangement can be determined about each type of atom separately in a given material. The systematic quantum mechanical treatment, initiated by Lytle, Sayers and Stern [45, 46,97] anticipated that the EXAFS technique can actually yield structure information on the material, particularly in situations where other techniques such as diffraction are not available. 3) In EXAFS, the structural information can be obtained by a simple and direct analysis. 4) With the advancement of synchrotron radiation, fast and easy measurements can be obtained as well.

The photoelectron in the process of repeated scatterings from the atoms of the condensed system before going out of the material, collects information on the neighbors of the absorber (Fig. 5.1). Several review papers have been published on the interpretation of the process including the possibility of understanding the x-ray absorption near-edge structure (XANES) [97,98,99], using the tools provided by the multiple scattering approach. When comparing theory with experimental data, detailed



information can be extracted on the local atomic environment about  $5 \text{ \AA}$ , around the photoabsorber.

### 5.1.2 Multiple Scattering Approximation

X-ray absorption measurement are performed on complex systems [48], a complex condensed system where the x-rays are tuned at energies above the threshold for the excitation of a deep core level of a given element. Usually, one measures  $\mu_c$ , the contribution to the x-ray absorption coefficient due to the excitation of the core level c.

$$\mu_c = n_c \sigma_c \quad (5.1)$$

where  $n_c$  is the number density of atoms with the core level c of concern and  $\sigma_c$  the absorption atomic cross section. As a function of the energy of the incoming photon, in the domain just before the threshold,  $\sigma_c$  presents a resonant structure which contains information about the binding energies, quantum numbers and the multiplicities of low lying energy levels. At the threshold,  $\sigma_c$  exhibits a finite jump, called the absorption edge. It was observed that above the absorption edge,  $\sigma_c$  shows marked fine structure, called XANES when near (usually 30 eV above the edge) and EXAFS away up to 1000 eV above the edge. For an isolated atom, the absorption cross section does not show any oscillatory behavior above the edge, it decreases smoothly as a function of the energy. It is important to say that XANES and EXAFS are then caused by the presence of the environment around the absorbing atom in the condensed material.

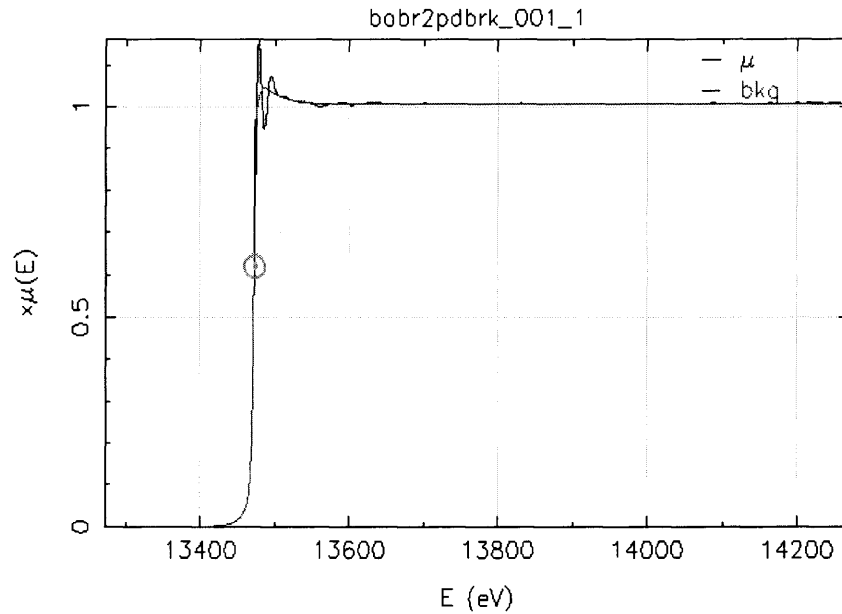
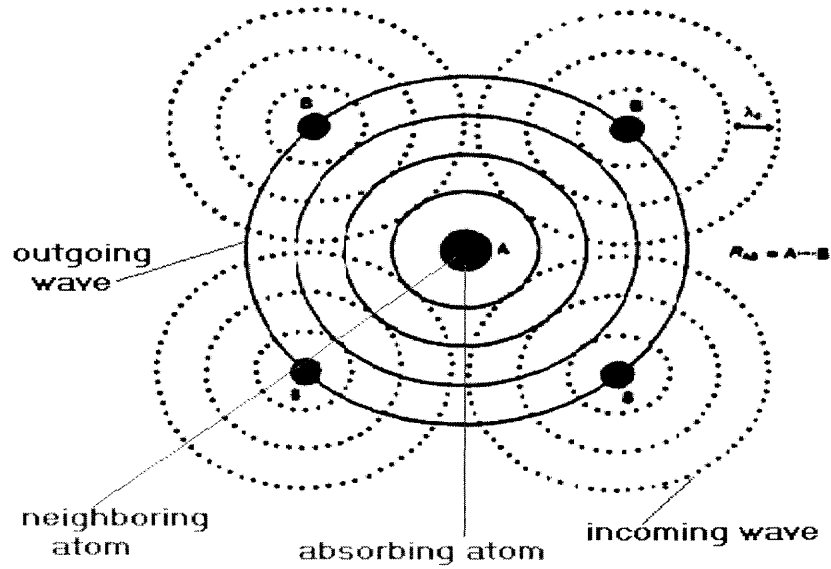


**Figure 5.1** Schematic of backscattering process, atom-A is the absorbing atom and atom-B the backscattering neighboring atom (above). Extended X-ray Absorption Fine Structure (EXAFS) of BaBr<sub>2</sub> powder sample, normalized and background subtracted (below).

In order to evaluate  $\sigma_c$  in the multiple scattering quantum mechanical approach, the photoemission transition matrix needs to be considered and evaluated on the energy shell, to the first order in the incoming photon field

$$T_{f \leftarrow i} = \left\langle \psi_f^{(z)} \left| \left\langle 0 \left| -\frac{e}{mc} \sum_{j=1} A(r_j) P_j \right| 1_i \right\rangle \right| \psi_i^{(z)} \right\rangle \quad (5.2)$$

where  $P_j$  is the momentum operator of the  $j$ th electron and  $m$  its mass.  $A(r_j)$  is the quantized radiation field evaluated at the position of the  $j$ th electron. The initial state vector is the product of the incoming photon state vector  $|1_i\rangle$  times the initial Z-electron atomic normalized bond state vector  $|\psi_i^{(z)}\rangle$  and the final state is given by the product of the photon vacuum  $|0\rangle$  times the state  $|\psi_f^{(z)}\rangle$  describing the emitted electron and the ionized (Z-1)-electron atom in which a deep core hole witnesses the absorption of the initial photon. In the Coulomb gauge  $\nabla_j \cdot A(r_j) = 0$ .

Within the frame work of a Hartree-Fock-Slater treatment of the states describing the initial and the final atoms, enables the factorization of those states reducing to the single particle amplitude

$$T_{f \leftarrow i} = F_0 \left\langle \psi_f^{(-)} \left| \left\langle 0 \left| H_I \right| 1_i \right\rangle \right| \psi_c \right\rangle \quad (5.3)$$

where  $|\psi_f^{(-)}\rangle$  and  $|\psi_c\rangle$  are now single particle states. It is important to mention that the single particle approach (5.3) holds well at energies away from the threshold, in the EXAFS region where the active electron scarcely intermingles with the other electrons in

the system. Expressing the total absorption cross section in terms of the transition matrix, we will obtain the following:

$$\sigma_c = 2 \sum_{m_i} \left( \frac{2\pi}{\hbar} \right)^4 \frac{m\hbar k_f}{c} \int d\Omega_f |T_{f \leftarrow i}|^2 \quad (5.4)$$

where  $m_i$  labels the orbital angular momentum degeneracy of the core level  $c$  and the factor 2 represents the two electrons lying on the level  $(E_c, l_i, m_i)$ .

The final energy can be written as  $E_f = \frac{\hbar^2 k_f^2}{2m} + Const$  and also the total absorption cross section can be rewritten to be:

$$\sigma_c = F_1 \sum_{m_i} \int d^3 k_f \delta(E - E_f) \left| \langle \psi_f^{(-)} | (H_I)_{01} | \psi_c \rangle \right|^2 \quad (5.5)$$

where  $E = \hbar\omega + E_c$  is the total initial energy,  $F_1 = 2 \frac{(2\pi)^4}{\hbar c} |F_0|^2$  and  $\langle 0 | H_I | 1_i \rangle = (H_I)_{01}$ .

Since  $|\psi_f^{(-)}\rangle$  is the eigenstate of the Hamiltonian  $H_f$  with eigenvalue  $E_f$ , we can write the the absorption cross section in the following:

$$\sigma_c = F_1 \sum_{m_i} \langle \psi_c | (H_I)_{10} \delta(E - H_f) \int d^3 k_f |\psi_f^{(-)}\rangle \langle \psi_f^{(-)} | (H_I)_{01} | \psi_c \rangle \quad (5.6)$$

Application of the operator  $\delta(E - H_f)$  eliminates the contribution of the bond states, we can write

$$\delta(E - H_f) |\psi_b\rangle = \delta(E - E_b) |\psi_b\rangle = 0 \quad (5.7)$$

since  $E > E_b$  and finally the absorption cross section can be written as

$$\sigma_c = F_1 \sum_{m_i} \langle \psi_c | (H_I)_{10} \delta(E - H_f) (H_I)_{01} | \psi_c \rangle \quad (5.8)$$

the absorption cross section can be evaluated in terms of the complete Greens function  $G$  defined by

$$G = \frac{1}{(E + i\epsilon - H_f)} = \frac{P}{(E - H_f)} - i\pi\delta(E - H_f) \quad (5.9)$$

where the limit  $\epsilon \rightarrow 0^+$  is understood and P means principal value. Now introducing the Hermitian conjugate of the propagator  $G$ , we get:

$$\delta(E - H_f) = \frac{i}{2\pi}(G - G^*) \quad (5.10)$$

the absorption cross section can be written in the form

$$\sigma_c = -\frac{F_1}{\pi} \sum_{m_i} \text{Im} \langle \psi_c | (H_f)_{i0} G (H_f)_{0i} | \psi_c \rangle \quad (5.11)$$

The Hamiltonian  $H_f$  can be written in terms of the kinetic energy of the ejected photoelectron and the sum of the all the potentials exerted on the photoelectron by the neighboring atoms.

$$H_f = K + U_a + \sum_{n \neq a} U_n \quad (5.12)$$

where  $K$  is the photoelectron kinetic energy . For simplification of the calculation, the photoelectron feels spherically symmetric non-overlapping local potentials  $U_n$ . This is so called the *muffin-tin potential* model.

The Green function can be written (generally)

$$G = G_a + G_a \left( \sum_{n \neq a} U_n \right) G \quad (5.13)$$

where  $G_a$  is the Green's function belonging to the potential  $U_a$

$$G_a = \frac{1}{E + i\epsilon - K - U_a} \quad (5.14)$$

Finally, the green's function can be written in terms the T-matrix

$$G = G_a + G_a T_{aa} G_a \quad (5.15)$$

where

$$T_{aa} = \sum_{n \neq a} U_n + \left( \sum_{n \neq a} U_n \right) G \left( \sum_{m \neq j} U_m \right) \quad (5.16)$$

substituting the Green's function into the absorption cross section we will obtain

$$\sigma_c = -\frac{F_1}{\pi} \sum_{m_i} \text{Im} \langle \psi_c | (H_I)_{10} [G_a + G_a T_{aa} G_a] (H_I)_{01} | \psi_c \rangle \quad (5.17)$$

where the first term in the right hand side give the total cross section for the photoemission from the isolated atom. The second term represents all the contributions to  $\sigma_c$  due to single and multiple scatterings suffered by the photoelectron in the material.

The operator  $T_{aa}$ , if it were not the fact that  $g$  also contains contributions from  $U_a$ , would represent the T-operator for the complete scattering of the photoelectron from the environment of the atom A. The multiple scatterings instead contain contributions from the resulting of the photoelectron from the absorbing atom A also.

In order to define the T-matrix, operators  $T_{kj}$  are defined as follows:

$$T_{kj} = \sum_{\substack{n \neq k \\ n \neq j}} U_n + \sum_{n \neq k} U_n G \sum_{m \neq j} U_m \quad (5.18)$$

for  $k=j=a$   $T_k$  reduces to (5.14). We singled out from  $G$  the contribution of the isolated atom  $N$ .

$$G = G_n + G_n \left( \sum_{p \neq n} U_p \right) G \quad (5.19)$$

now substituting (5.18) into (5.19) we get the following

$$T_{kj} = \sum_{\substack{n \neq k \\ n \neq j}} U_n + \sum_{n \neq k} U_n G_n \sum_{m \neq j} U_m + \sum_{n \neq k} U_n G_n \left( \sum_{p \neq n} U_p \right) G \sum_{m \neq j} U_m \quad (5.20)$$

Then we can define the complete T-operator for the scattering of the photoelectron from the isolated atom  $N$  as  $t_n$

$$t_n = U_n + U_n G_n U_n \quad (5.21)$$

we can see that the first two terms in (5.20) contain a sum of  $t_n$  therefore we can rewrite (5.20) to be

$$T_{kj} = \sum_{\substack{n \neq k \\ n \neq j}} t_n + \sum_{n \neq k} U_n G_n \left( \sum_{\substack{m \neq j \\ m \neq n}} U_m + \sum_{p \neq n} U_p G \sum_{m \neq j} U_m \right) \quad (5.22)$$

the bracket in right hand side of (5.22) is the  $T_{nj}$  by comparison we can write as follows

$$U_n G_n = t_n G_0 \quad (5.23)$$

where  $G_0$  is the free-space greens function which is defined as follows

$$G_0 = \frac{1}{E + i\varepsilon - K} \quad (5.24)$$

and also  $G_n$  is expressed in terms of  $G_0$

$$G_n = G_0 + G_0 U_n G_n = G_0 + G_n U_n G_0 \quad (5.25)$$

we then obtain a simple integral equation for the T-matrix

$$T_{kj} = \sum_{\substack{n \neq k \\ n \neq j}} t_n + \sum_{n \neq k} t_n G_0 T_{nj} \quad (5.26)$$

We are going to write down a perturbative expansion in multiple scattering terms for  $T_{aa}$  in terms of the Green's function as follows

$$T_{aa} = \sum_{n \neq a} t_n + \sum_{n \neq a} t_n G_0 \sum_{\substack{m \neq n \\ m \neq a}} t_n + \sum_{n \neq a} t_n G_0 \sum_{m \neq n} t_m G_0 \sum_{\substack{k \neq m \\ k \neq a}} t_k + \sum_{n \neq a} t_n G_0 \sum_{m \neq n} t_m G_0 \sum_{k \neq m} t_k G_0 \sum_{\substack{j \neq k \\ j \neq a}} t_j + \quad (5.27)$$

Substituting (5.27) into the equation for the absorption cross section we will obtain an expression of the total cross section as a sum of all the possible multiple scatterings. The overlap of these terms with that representing the photoemission from the isolated atom A gives rise to the structures (called XANES and EXAFS) observed in the absorption coefficient far above the threshold energy, the scattering of the photoelectron is taken to be weak, so we can retain only the single scattering term. At low energies, near the threshold, the scattering is strong, hence in the energy region where the perturbative expansion still converges, one must also take into consideration multiple-scattering terms of higher order.

### 5.1.3 The Photoemission Cross Section and the Multiple-Scattering Function

We will proceed to evaluate the total photoemission cross section  $\sigma_c$  by applying the dipole approximation, which amounts to substituting for  $\langle 0|H_I|1_i\rangle = (H_I)_{01}$  then we can write the following:

$$(H_I)_{01} \rightarrow -i \left[ \frac{\hbar\omega}{2(2\pi)^3} \right]^{\frac{1}{2}} \varepsilon \cdot e r \quad (5.28)$$

where  $\varepsilon$  is the unit polarization vector of the photon. Substituting (5.28) into the absorption cross section we will obtain

$$\sigma_c = -2\hbar\omega\alpha |F_0|^2 \sum_{m_i} \text{Im} \langle \psi_c | \varepsilon \cdot r [G_a + G_a T_{aa} G_a] \varepsilon \cdot r | \psi_c \rangle \quad (5.29)$$

where  $\alpha = \frac{e^2}{\hbar c}$  and  $\varepsilon \cdot r | \psi_c \rangle = \frac{4\pi}{3} \sum_{m_i} Y_{1m_i}^*(\varepsilon) Y_{1m_i}(r) |R_i\rangle$ . The free propagator  $G_0$  and

the complete  $G_a$  Greens functions can be evaluated.



For the free propagator we can write:

$${}_a\langle r|G_0|r'\rangle_a = -\frac{1}{4\pi} \frac{2m}{\hbar^2} \frac{e^{ik|r-r'|}}{|r-r'|} = \sum_L Y_L(r) G_{0l}(r, r') Y_L^*(r') \quad (5.30)$$

where  $G_{0l}(r, r') = -ik \left( \frac{2m}{\hbar^2} \right) j_l(kr_l) h_l^{(+)}(kr_l)$  and for the complete propagator we will obtain:

$$G_{al}(r, r') = -\frac{1}{4\pi} \left( \frac{2m}{\hbar^2} \right) \frac{(-i)^l}{krr'} \psi_l^{(+)}(k, r_l) f_l^{(+)}(k, r_l) \quad (5.31)$$

We can introduce the multiple scattering function which contains all the contributions from the environment of the absorbing atom

$$\chi_{L,L'} = i\delta_{LL'} + \sum_{s=2} \chi_{LL'}^{(s)} \quad (5.32)$$

where the first term gives rise to the cross section  $\sigma_c^{(A)}$  and the multiple scattering function is given by

$$\chi_{L,L'}^{(2)} = \frac{2m}{\hbar^2} k e^{2i\delta_l^{(A)}} \int d^3r' d^3r'' Y_L^*(r') h_l^{(+)}(kr') {}_a\langle r'|T_{aa}|r''\rangle_a h_l^{(+)}(kr'') Y_{L'}(r'') \quad (5.33)$$

Hence the total photoemission cross section averaged over the polarization vector turns out to be:

$$\sigma_c = \frac{1}{4\pi} \int_{4\pi} \sigma_c d\Omega_c = F_2 \sum_l [(l_i + 1)\delta_{l,l_i+1} + l_i\delta_{l,l_i-1}] M_l^{(A)} \frac{1}{2l+1} \sum_m \text{Im} \chi_{L,L'} \quad (5.34)$$

unpolarized photon beam.

The average of  $\sigma_c^{(A)}$  is obtained by substituting 1 from  $\text{Im} \chi_{L,L}$ . Finally, the multiple scattering function can be expressed in terms of the absorption coefficient for the  $K$ -shell

For  $l_i=0, l=l_i=1$  we obtain the following:

$$\frac{\mu_c - \mu_c^{(A)}}{\mu_c^{(A)}} = \frac{1}{3} \sum_m \text{Im} \chi_{1m,1m} - 1 \quad (5.35)$$

where, the isolated atom background is defined to be  $\mu_c^{(A)} = n_c \sigma_c^{(A)}$

By taking the polarization vector along the z-axis for simplicity we also have  $m=m'$  we get the imaginary part of the multiple scattering expression

$$\text{Im} \chi_{10,10}^{(2)(\text{Kedge})} = -3 \sum_{p \neq a} \left( \varepsilon \cdot \frac{R_{pa}}{R_{pa}} \right)^2 \frac{|f_p(\pi)|}{kR_{pa}^2} \sin(2kR_{pa} + 2\delta_1^{(A)} + \Phi_p) \quad (5.36)$$

where the backscattering amplitude is given by

$$f_p(\pi) = |f_p(\pi)| \exp(i\Phi_p) \quad (5.37)$$

for the unpolarized case we will obtain

$$\frac{1}{2l+1} \sum_m \text{Im} \chi_{LL}^{(2)} = (-1)^l \sum_i \frac{N_i |f_i(\pi)|}{kR_i^2} \sin(2kR_i + 2\delta_l^{(A)} + \Phi_i) \quad (5.38)$$

where  $N_i$  is the number of identical atoms on the  $i$ th shell at the distance  $R_i$  from the absorber (coordination number) and  $k = \frac{\sqrt{2m(E - E_0)}}{\hbar}$  is the photoelectron wave vector.

Under the assumption of a muffin-tin potential, the single scattering contribution to  $\chi(k)$  is given by (A. Kuzmin [104]).

$$\chi(k) = \sum_i^{\text{shells}} S_0^2 \frac{N_i}{kR_i^2} f_i(\pi, k, R_i) \exp\left(-2\sigma_i^2 k^2 + \frac{2}{3} C_{4ii} k^4\right) X \exp\left(-\frac{2R_i}{\lambda(k)}\right) \sin\left(2kR_i - \frac{4}{3} C_{3i} k^3 + \phi_i(\pi, k, R_i)\right) \quad (5.39)$$

where  $S_0^2$  is the scale factor taking into account amplitude damping due to the multielectron effects,  $N_i$  is the coordination number of the  $i$ -shell,  $R_i$  is the radius of the  $i$ -

shell,  $\sigma_i$  is the mean square radial displacement or Debye-Waller factor,  $C_{3i}$  and  $C_{4i}$  are cumulants of a distribution taking into account anharmonic effects and /or non-Gaussian disorder;  $\lambda(k)$  is the mean free path of the photoelectron;  $f_i(\pi, k, R_i)$  is the backscattering amplitude of the photoelectron due to atoms of the  $i$ -coordination shell;  $\phi_i(\pi, k, R_i)$  is the phase shift containing contributions from the absorber  $2\delta_l(k)$  ( $l$  is the angular momentum of the photoelectron,  $l=1$  for  $K$  and  $L_1$  edges and  $l=2$  or  $0$  for  $L_{2,3}$  edges). Equation (5.39) is the most commonly used in applications. It is important to mention that from equation (5.39), a great deal of information can be extracted from comparison with experimental data, using the method of Fourier transform and filtering, about the local atomic arrangement around the absorbing atom. When analyzing equation (5.39), one can obtain atomic structure quantities such as bond distances (with accuracies as good as  $\pm 0.001 \text{ \AA}$ ), coordination numbers and mean square displacements (Debye-Waller factor). Electron scattering becomes strong at low energies so, as we approach the absorption edge from above, more and more terms of the perturbative expansion are needed to describe the behavior of the cross section. In general, the EXAFS (high energy range) region, where only single scatterings are relevant merges into XANES region where multiple scatterings become important. Then, very close to the edge, because of the non-convergence of the multiple scattering series, one needs to use the full non perturbative solution.

## 5.2 XAFS Data Analysis

The first step in the data reduction is to convert the experimental “variables” into an experimental “spectrum”, where the Y-axis is the total linear absorption coefficient  $\mu(E)$

which is given by [102]:

$$\mu(E)x = \ln \frac{I_0}{I} \quad (5.40)$$

in transmission experiments but

$$\mu(E)x = \frac{I_f}{I_0} \quad (5.41)$$

in fluorescence experiments. In this thesis, the XAFS experiments on standard powder samples and on the YBCO single crystals were performed in transmission and fluorescence modes respectively.

### 5.2.1 Normalization

In most experiments, the exact concentration of the absorbing atom (e.g. Br, Cu, Y, Ba) neighboring atoms and sample thickness are not precisely known [99, see Sayers and Bunker in ref.99]. It is also important to mention that a variety of materials such as mylar windows and the sample matrix itself, enter into the beam path between the  $I_0$  monitor and the detector. This causes the observed signals to be multiplied by energy dependent factors. For example, in transmission experiments, a logarithm of the ratio of measured currents is taken, so the multiplicative factor turns into an additive background that varies slowly with energy. In contrast to the fluorescence detection, however, no log is taken and the energy dependent factors are carried through the entire analysis. This causes no problem, as long as the effect is the same for standard and unknown, and the energy dependence is very smooth. The elastically and inelastically scattered x-ray photons from the incident beam contribute an additive background to fluorescence data. Thus, at present, the EXAFS spectra are usually determined only modulo a scale factor

and slowly varying background. In some cases, it is desirable to measure the baseline spectrum separately, and then subtract it out. This of course will work if the background is sample independent which is not always the case in fluorescence studies. The normalization procedure by which the data is divided by the size of the edge step, compensates for the uncertainties in the concentration and sample thickness.

### 5.2.2 Conversion to $k$ -Space

**Sampling:** Conversion to  $k$ -space should be done before background subtraction so that the background fit does not preferentially follow the data at high energy (which oscillates slowly in energy space) [99]. Usually the experimental data are not collected on an even grid in  $k$ -space (although this is desirable), and therefore interpolation is performed when the change of variable is made. A uniform grid in  $k$ -space is desirable so that standard discrete Fourier transform algorithm can be used. Usually, a grid in  $k$ -space of  $0.05 \text{ \AA}$  is used, this adequately samples the EXAFS from shells out to distances of  $30 \text{ \AA}$ , which are quit negligible.

**Choice of  $E_0$ :** In order to convert to  $k$ -space, the value of  $E_0$ , the threshold energy (muffin tin zero level in the theory) must be specified [47]. Typically the half-maximum point on the edge is taken, or the bottom of the edge, or the top. Physically, somewhere near the bottom of the edge, close to the Fermi level, is probably preferred. In EXAFS data analysis, one needs to be aware of relative shifts that exist between the standard and the unknown; these energy shifts are very important: If both are shifted by the same energy amount then, the answer is going to be the same in a good approximation.

From our data analysis, we found that relative energy shifts affect mostly the data at low values of  $k$  (XANES domain). Thus, ambiguities in the absolute  $E_0$  position and small as (3 eV) differences in relative  $E_0$  position, do not introduce corresponding ambiguities in structure determination by EXAFS. We conclude that the choice of  $E_0$  does pose significant uncertainties for  $k$ -space analysis in the XANES region, however.

### 5.2.3 Background Subtraction

**Atomic Contribution:** Background subtraction is performed [99,100,101], to isolate the oscillatory EXAFS from the atomic part of the absorption and the background absorption or scatter from other elements in the beam path (Fig.5.2). In principle, the isolated atom absorption (which is generally unknown) is subtracted from the absorption of the atom in condensed matter, and the result is then divided by the isolated atom absorption.

**Precautions:** Background subtraction is accomplished by ordinary linear least squares fitting, typically using cubic spline functions. The differences between the data and the fit are weighted by an increasing function of  $k$  (such as  $k^3$ ) so that the data at high  $k$  (which are for small amplitudes) are adequately fit (Fig.5.2). In background subtraction, it is important to remove the background but not alter the data. If the background subtraction is too severe, the first shell in the EXAFS amplitude spectra will be distorted and significantly reduced. Also, if too little background is removed spurious contributions appear in the Fourier transforms, which may (or may not) overlap and interfere with the first shell signal. A variety of smooth functions can be used for background subtraction, as long as the fit is constrained to not oscillate at the same frequency (or higher) as the first shell data.

**Cubic Spline:** The most common functional form used in background subtraction is the least squares cubic spline. The cubics are constrained so the values, the first and the second derivatives match at the junctures (called “knot”). In most cases adequate background subtraction can be obtained by simply specifying a sufficient number of regions using cubic splines. One normally uses as few regions as necessary to give adequate background subtraction as judge by the Fourier transforms.

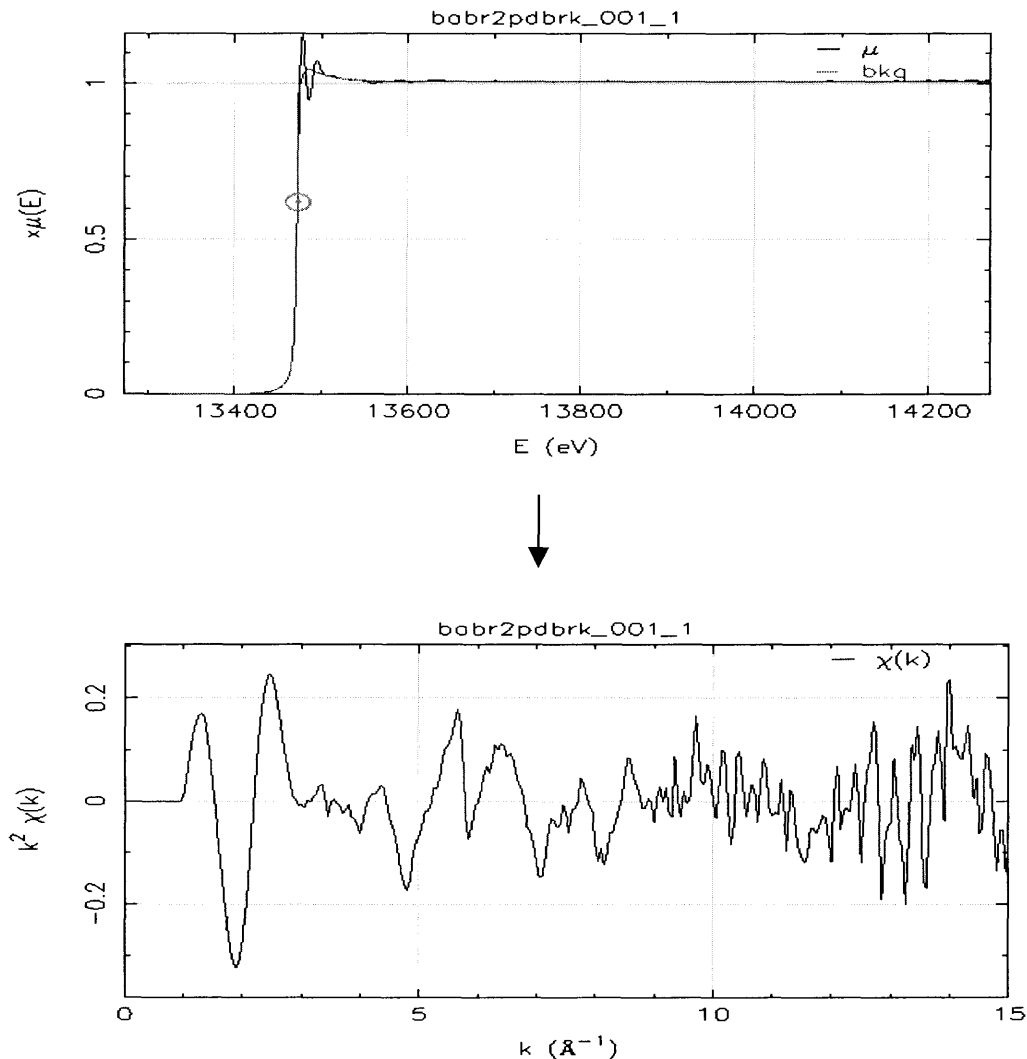


**Figure 5.2** EXAFS at Br *K*-edge ( $E_0 = 13474$  eV) for  $\text{BaBr}_2$  powder sample, normalized and background subtracted (above). From the above EXAFS graph,  $\chi(k)$  was extracted and weighted by  $k^2$  ( $k^2\chi(k)$ ) below.

### 5.2.4 Fourier Transform and Filtering

The next significant step occurred when it was realized that an appropriate Fourier analysis of the EXAFS data can locate the positions of atoms surrounding the x-ray absorbing atom [46,48,99]. This was important because it changed EXAFS from a qualitative effect to a quantitative one.

At this point, the data consist of sums of damped sine waves corresponding to the different shells of atoms. In order to reduce the number of fitting parameters, it is useful to separate the signals from different shells using Fourier filtering methods. These also permit a decomposition of the oscillations into amplitude and phase functions.

**Data Range:** Typically EXAFS data have good signal to noise ratios up to  $k \sim 18 \text{ \AA}^{-1}$  and the region below  $k \sim 2 \text{ \AA}^{-1}$  is excluded because of possible complications from multiple scattering [99]. It is important to mention that, multiple scattering is not a concern for first shell analysis, however, lower values of  $k$  are included in the transform. Plotting several independent scans is very helpful in determining the useful range of the data (essential). Extending the data to regions in which the signal is negligible doesn't help to resolve transform peaks.

**Interpretation of the Fourier Transform:** The data are generally weighted with some power of  $k$  (typically  $k^1, k^2$  or  $k^3$ ) to compensate for the decay of the waves, i.e. to make the data more nearly like a monochromatic sine waves over the data range. It should be born in mind that if the transform range (or weighting) were different from the background subtraction range (or weighting), low- $r$  transform peaks would generally be present.. The Fourier transform (FT) and back Fourier transform (BFT) are calculated by using the formulas:



$$FT(R) = \chi(R) = \left(\frac{2}{\pi}\right)^{\frac{1}{2}} \int_{k_{\min}}^{k_{\max}} \chi(k) k^n W(k) e^{-2ikR} dk \quad (5.42)$$

$$BFT(k) = \chi(k) = \frac{1}{W(k)} \left(\frac{2}{\pi}\right)^{\frac{1}{2}} \int_{R_{\min}}^{R_{\max}} FT(R) e^{2ikR} dR \quad (5.43)$$

where  $k_{\min}$ ,  $k_{\max}$  and  $R_{\min}$ ,  $R_{\max}$  denote the range of the Fourier transform in  $k$ - $r$ -space,  $W(k)$  is a window function. Since the Fourier transform procedure is only correct for the integration in the infinite range while experimental signal is always limited by some interval, it is assumed that the signal goes to zero at  $k \rightarrow \pm\infty$ . To eliminate the abrupt behavior of the signal at the ends of the measured interval, the window function is used. The window function used in order to fit our EXAFS data is given by the Kaiser-Bessel function which has the form [103]:

$$W(k) = \frac{J_0 \left( \pi A \sqrt{1 - \left(1 - \frac{k}{\bar{k}}\right)^2} \right)}{J_0(\pi A)} \quad (5.44)$$

where  $A$  is the parameter of window,  $J_0(x)$  is the Bessel function and  $\bar{k} = \frac{k_{\min} + k_{\max}}{2}$

The modulus of  $\chi(R)$  exhibits peaks that correspond to various coordination shells. The position of the peaks corresponds to the average frequency of the corresponding shell's EXAFS, which is related to the average distance in the shell. The peak height is related to the average amplitude of the (weighted) EXAFS over the data range and is therefore related to the number of atoms in the shell, the disorder parameter  $\sigma^2$ , the atomic number

of atoms in the shell. The transform depends on many factors including the  $k$  –range, and in good data analysis several transforms with different  $k$  weightings and  $k$ -ranges are examined until an understanding of the data is achieved. Standard samples are essential in any analysis. It is important to mention that, moderate to large disorder ( $k_{max} \sigma \approx 1$ ) in distances can cause significant peak shift that do not correspond to the average distance.

After Fourier and back Fourier transforms are performed and useful functions can be obtained [99,102].

$$|FT(R)| = \sqrt{\text{Im}(FT(R))^2 + \text{Re}(FT(r))^2} \quad (5.45)$$

$$AMPL(\chi(k)) = \sqrt{\text{Im}(BFT(k))^2 + \text{Re}(BFT(k))^2} \quad (5.46)$$

$$PHASE(\chi(k)) = \arctan\left(\frac{\text{Im}(BFT(k))}{\text{Re}(BFT(k))}\right) \quad (5.47)$$

where  $Im$  and  $Re$  denote the imaginary and real part respectively.

Useful tips:

- a) Always use the same range  $k$ -space for both the FT and BFT procedures.
- b) The best window is the one which produces the smallest distortion of the EXAFS signal after the FT and BFT procedures are applied. From our fits results, we found that the Kaiser-Bessel window gives the best results for our system.

### 5.2.5 Fitting EXAFS Data

In the single scattering approximation, the EXAFS equation is given by (5.39).

In this work, the backscattering amplitudes and phase shifts are calculated theoretically using the FEFF code.

The canonical method of estimating parameters and their error bars (confidence intervals) in non-linear least squares theory requires one to minimize the mean square error  $\varepsilon^2(\{\alpha\})$  between the data and the fit:

$$\varepsilon^2(\{\alpha\}) = \frac{1}{N_{pts} - N_{par}} \sum_j \frac{(Data_j - Fit_j(\{\alpha\}))^2}{q_j^2} \quad (5.48)$$

where  $\alpha$  denotes the set of parameters varied in the fit,  $N_{pts}$ ,  $N_{par}$  are respectively the number of independent data points and the number of parameters floated in the fit. It is important to note that  $\varepsilon^2(\{\alpha\})$  is dimensionless and the noise level represented by  $q_j^2$  in the data has been divided out. The best values that are much greater than 1.0 are considered poor fits, and any fit less than about 1.0 is considered acceptable.

Two essential points need to be kept in mind. The first is that the denominator in equation (5.48) must be included to properly account for the number of degrees of freedom used in the fit. The second is that the number of independent data points is reduced by Fourier filtering. In essence, when doing forward transform, the transformation content in  $k$ -space is spread out over a wide range of  $r$ , and when one uses an  $r$ -space window and inverse transform only a fraction of the information is retained. The number of independent data points after Fourier filtering using windows of width  $\Delta k$  and  $\Delta r$  is given by the formula [61]:

$$N_{pts} = \frac{2\Delta k \Delta r}{\pi} + 2 \quad (5.49)$$

The number of parameters floated in the fit should not exceed any value given by formula (5.49) [61,99]. We extracted the following parameters  $S_0^2$ ,  $N_j$ ,  $R_j$ ,  $\sigma_j^2$ ,  $\Delta E$ ,  $C_3$ , and  $C_4$  by fitting our EXAFS data.

## CHAPTER 6

### X-RAY ABSORPTION FINE STRUCTURE SPECTROSCOPY (XAFS) OF HALOGENATED $\text{YBa}_2\text{Cu}_3\text{O}_{6+x}$ SINGLE CRYSTALS

#### 6.1 X-ray Absorption Fine Structure of Brominated (non-brominated) $\text{YBa}_2\text{Cu}_3\text{O}_{6+x}$ ( $x \sim 0.6$ ) Single Crystals

##### 6.1.1 Introduction

The recovery of superconductivity in underdoped  $\text{YBa}_2\text{Cu}_3\text{O}_{6+y}$  (YBCO) by exposure to bromine is a long-standing problem which has not been clearly resolved. The key question concerns the role of Br in the lattice. Whether Br is incorporated in one of the crystallographic sites and dopes the system [49,50,51] or if it causes a local decomposition reaction to occur, creating an amorphous products, liberating oxygen, and oxygenating the underdoped unreacted regions [52] remains in dispute.

The first observation of the effect was made by Osipyan *et al.* [49] who reported a critical temperature ( $T_c$ ) of 90-92 K and orthorhombic phase formed by exposing initially tetragonal,  $y \sim 0$ , YBCO samples to gaseous chlorine [49 (a)]. Further work by this group showed that exposure to  $\text{Br}_2$  and  $\text{I}_2$  resulted in the recovery of superconductivity [49 (b)] with  $T_c = 80-85$  and 55K, respectively. Radousky *et al.* [50] performed systematic structural (x-ray diffraction), spectroscopic, and analytic measurements in an attempt to ascertain the role of Br in the restoration of superconductivity. In x-ray diffraction (XRD) measurements, bromination was found to increase peak widths and introduce a diffuse background typical of a partly amorphous phases. The diffraction pattern was not significantly different from the oxygen-rich orthorhombic YBCO pattern. Bromination was found to alter significantly the Raman

active phonons, changing the O(4) [53] vibration frequencies. These experiments, however, were not able to ascertain the location and chemistry of the Br atoms.

X-ray photoelectron spectra of brominated YBCO suggested that Br could have a chemical environment similar to that in BaBr<sub>2</sub> [54]. Several bulk-sensitive measurements attempted to resolve the structural changes induced by bromination of underdoped YBCO. Neutron diffraction studies suggested that Br occupies vacant O(1) sites [55]. Earlier x-ray absorption fine structure (XAFS) measurements at Y *K*-edge [56] found no changes in the local structure about the Y sites, while it was claimed, from the Br *K*-edge data, that Br entered vacancies in Cu(1)-O(1) containing planes. Recently, Potrepka *et al.* [57], investigated the local atomic structure (about Cu and Br) using <sup>63,65</sup>Cu nuclear quadrupole resonance (NQR) and <sup>79,81</sup>Br nuclear magnetic resonance (NMR) on well-characterized powder samples of parent, deoxygenated, and brominated YBCO. The NMR signal for the Cu(2) peak in brominated samples was found to be broadened compared to that in the parent materials. This was interpreted as the possible coexistence of a broad contribution from a component where the Cu(2) near-neighbor environment had been perturbed and has a sharp contribution reminiscent of Cu(2) sites in well-ordered superconductor (two-phase model). However, neither the phase ratio nor the details of the local structure of the perturbed phase were determined. Potrepka *et al.* also performed low temperature Br *K*-edge XAFS measurements [57] and argued that Br did not enter the lattice substitutionally or interstitially. XAFS spectra were found to be similar to those of BaBr<sub>2</sub> powder. They suggested that bromination led to BaBr<sub>2</sub> precipitation as nano-particles which gave rise to the higher background seen in XRD.

Unfortunately, model fitting of the XAFS spectrum was not performed and hence the details of local structure about Br remained unknown.

The motivation of this paper is to provide a quantitative characterization of local distortions about Br, Cu, Ba, and Y sites (leading to a three dimensional picture) and to determine the location of the Br atoms and possible phase composition of the brominated  $\text{YBa}_2\text{Cu}_3\text{O}_{6+y}$  ( $y \sim 0.6$ ) crystal. In contrast to previous XAFS measurements, we utilized slightly brominated crystals (1 Br atom per 30 Cu atoms), combined with x-ray fluorescence yield (FY) measurements. Use of well-oriented samples was important because it allows one to take advantage of the high degree of linear polarization of synchrotron x-rays to isolate the atomic species contributing to the XAFS signal. For instance, *c*-axis polarized XAFS provides a direct probe of Cu(1)-O(4) and Cu(2)-O(4) pairs, eliminating contributions from the "in plane" Cu(2)-O(2,3) pairs and, therefore, reducing the number of parameters in the XAFS fit. The number of free parameters is sufficient to perform a quantitative characterization of *two phases*, enabling us to address the issue of possible phase separation in brominated YBCO. FY measurements do not require high Br content. Moreover, slightly brominated samples appear to be less structurally distorted and less subjected to possible decomposition reactions [52], simplifying the structural analysis while keeping the physics unchanged.

The combined analysis of the Cu *K*-, Ba *L*<sub>3</sub>- and Y *K*-edge XAFS data undertaken in this work has a significant advantage over traditional single-edge XAFS. In distorted multiple-phase compounds the probing length of XAFS is typically limited to 3-4 Å (2-3 first coordination shells about the absorption site). In order to determine what part of the

YBCO unit is affected by bromination, the local distortions introduced about the Cu, Ba and Y sites must be compared.

In Section 6.1.3, we describe experimental details and data analysis for mixed-phase compounds. In Sect 6.3.3.1, Br *K*-edge XAFS analysis will be used to show that *Br does not enter a perfect YBCO lattice*, while it does occupy the Cu(1) position in fragment of the lattice forming a nano-cluster of Br-O(4)-Ba-Cu(1)Cu(2)-... . C-axis polarized Cu *K*-edge XAFS reveals that the Cu-O pair distribution of the brominated sample can be best described in terms of a two-phase model with a 2:1 ratio of Cu(1,2)-O(4) pairs [as in the well-ordered YBCO ( $y \sim 0.9-1$ )] and presumably Cu(2)-O(2,3) pairs of  $\sim 1.95 \text{ \AA}$  (Sect. 6.1.3.2). This result is further supported by polarized Cu *K*-edge XANES measurements given in Sect 6.1.3.3. The behavior of major peaks in the XANES spectra suggest a re-oxygenation of about 2/3 of the brominated sample accompanied by the appearance of a decomposed phase exhibiting a weak polarization dependence. Ba *L*<sub>3</sub>-edge and Y *K*-edge XAFS are presented in Sect. 6.1.3.4 and 6.1.3.5. Multiple-edge data analysis outlined in Sect. 6.2 are consistent with the formation of a strongly heterogeneous sample as a result of bromination. About 1/3 of the YBCO is decomposed. This decomposed phase consists of nano-domains of the fragmented YBCO lattice which are embedded in a "host" lattice resembling well-ordered oxygen-rich YBa<sub>2</sub>Cu<sub>3</sub>O<sub>6+x</sub> ( $x \sim 0.9-1$ ). The fragmentation takes place mostly along the Cu(1)-O(1) containing planes accompanied by rearrangement of the nano-domains. The implications of diffraction, magnetization and resistivity measurements are discussed at the end of Sect. 6.2 and the conclusions of this work are summarized in Sect. 6.3.

## 6.1.2 Experimental Procedure and Data Analysis

### A. Preparation of YBCO Single Crystals

Single crystals of  $\text{YBa}_2\text{Cu}_3\text{O}_{6+x}$  ( $x \sim 0.6$ ) were prepared by Prof. F. Dogan (from University of Washington now at the University of Missouri) for the experiments conducted.  $\text{YBa}_2\text{Cu}_3\text{O}_{6+x}$  powders doped with  $\text{Y}_2\text{BaCuO}_5$  and Pt were compacted by pressing. A seed crystal of  $\text{SmBa}_2\text{Cu}_3\text{O}_7$  was placed on the top center of this compact. The sample was heated to 1050 °C and cooled below the peritectic melting temperature. The nucleation and growth process of undercooled semisolid YBCO was initiated by the seed crystal at 1005 °C. The YBCO crystal was then grown under isothermal conditions. Samples for XAFS studies were prepared by cleaving of the crystals along the *ab* plane.

### B. Bromination of $\text{YBCO}_{6.6}$ single-crystal

Bromination of the  $\text{YBCO}_{6.6}$  single crystal was performed by inserting a glass tube inside a tube furnace which was heated up to 260°C Fig. 6.1, 6.1(a). While the tube furnace was at 260°C, the glass tube was left inside for about two hours to assure equilibrium temperature. Prior the entry of  $\text{Br}_2$  vapor, the glass tube was evacuated with nitrogen gas for 30 minutes to remove oxygen. A pair of single crystals from the same batch (with the same oxygen content) was used in these experiments. A single crystal YBCO sample in a quartz boat was inserted inside the glass tube in a nitrogen atmosphere at 260°C. a sample of 99.5% pure  $\text{Br}_2$  liquid in a small 50 ml beaker was connected to one of the ends of the glass tube which was submerged in a 1000 ml beaker with water. And the other end of the quartz road was submerged in another 1000 ml beaker with water to dissolve the  $\text{Br}_2$  vapor. Then the  $\text{Br}_2$  vapor was carried out in a nitrogen atmosphere by heating the 1000 ml beaker at about 50 °C since bromine evaporates at 59 °C. The single



crystal YBCO sample was treated under the  $\text{Br}_2$  vapors in nitrogen atmosphere at  $260^\circ\text{C}$  for about an hour. The sample was cooled to room temperature and removed.

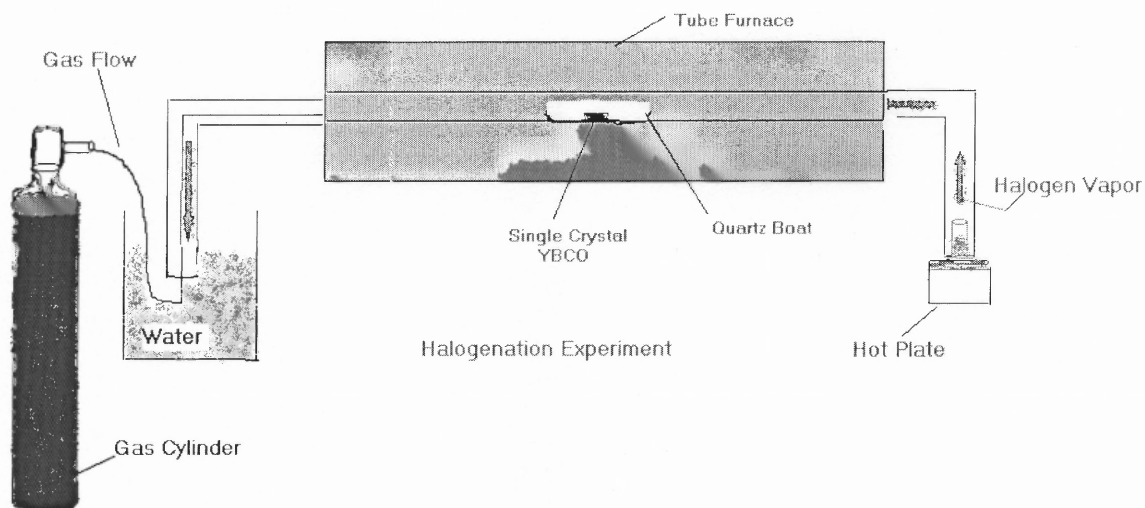


**Figure 6.1** Experimental set up for halogenation of YBCO single crystals. YBCO single crystals were placed inside the tube furnace under nitrogen gas flow for bromination and argon gas flow for iodination experiments.

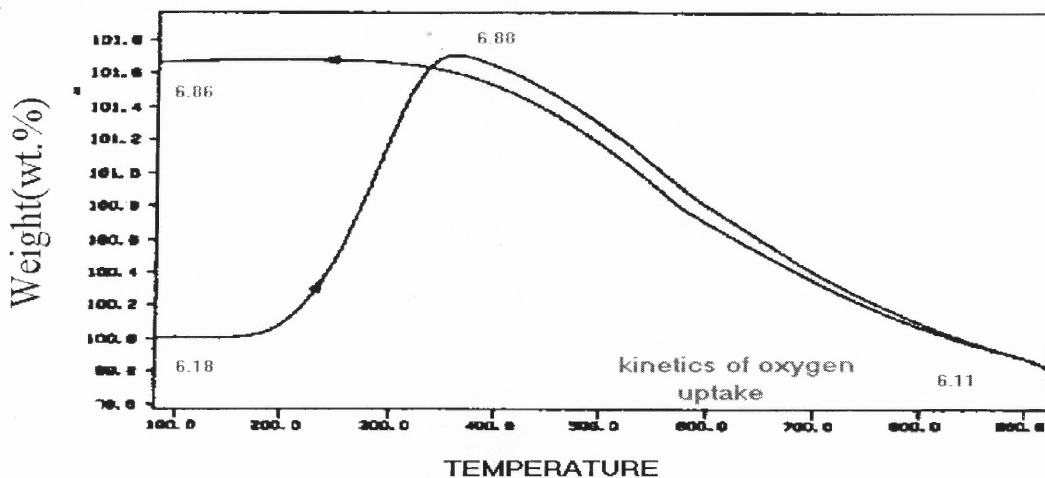


**Figure 6.1(a)** Kinetics of oxygen uptake of  $\text{YBCO}_{6+x}$  sample heated in  $\text{O}_2$  at  $1^\circ\text{C}/\text{min}$ . Numbers on the plot refer to oxygen content [Goodenough *et. al.*,]

In order to find the  $\text{Br}_2$  content in the single crystal YBCO sample, the sample, (at QTI Inc). The bromine content was determined by using a combustion and titration techniques

and was found to be about 1.24 % (wt) Br - corresponding to a Br:Cu ratio of  $\sim 1:30$ . Zero-field-cooled magnetization measurements (in a 20 Oe magnetic field) on the brominated sample were compared with those of normal crystal (Fig. 6.2) revealing an enhancement of the critical temperature from 63 to 89 K (onset).

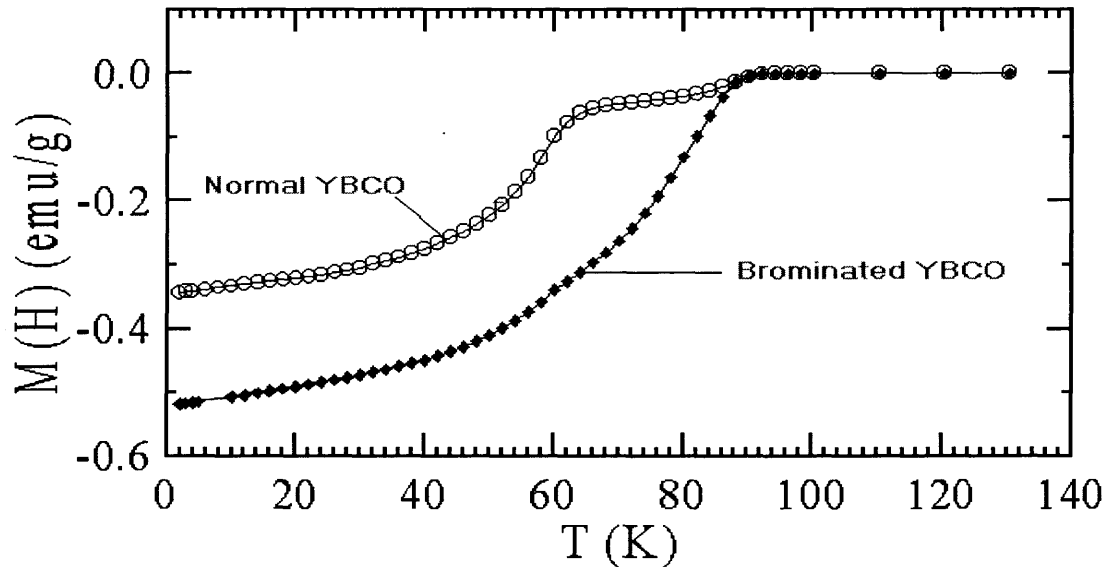


**Figure 6.2** Zero-field-cooled magnetization vs. temperature in a 20 Oe magnetic field for brominated (diamonds) and normal (open circles) YBCO( $x \sim 0.6$ ). Spectra are not corrected for the demagnetization factor.  $T_C$  is taken at the onset for superconductivity. The untreated sample has a minor component ( $\sim 15\%$ ) with  $T_C \sim 88$  K and major component with  $T_C \sim 63$  K. Bromination produces samples with  $T_C \sim 89$  K.

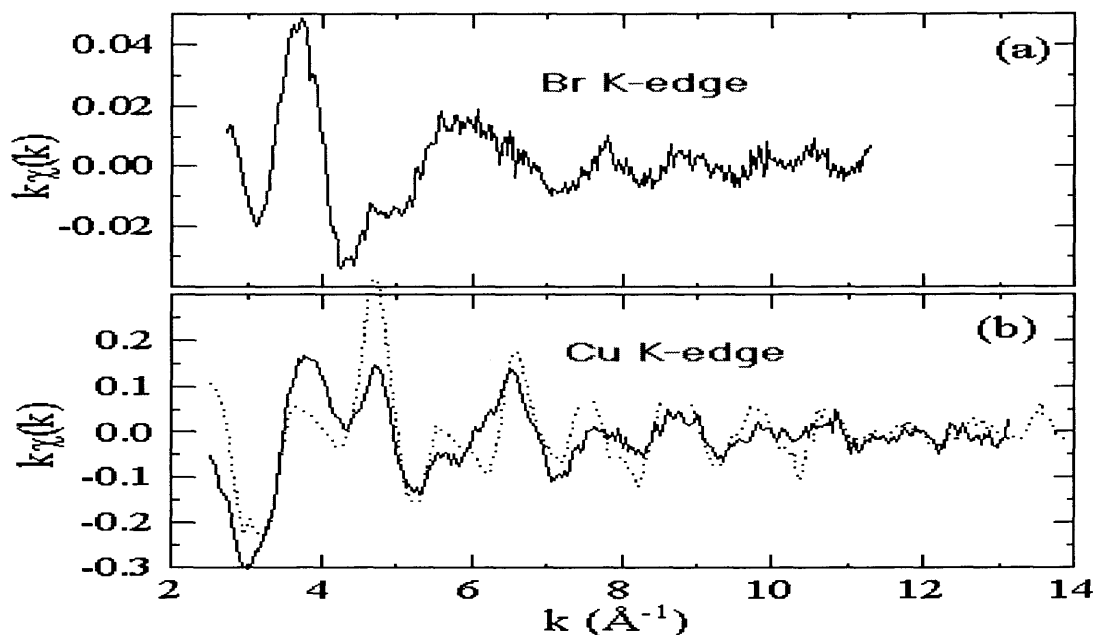


**Figure 6.3** (a) Br  $K$ -edge  $k\chi(k)$  vs  $k$  for brominated YBCO with x-ray polarization at 45 Deg to the  $c$ -axis. (b) Cu  $K$ -edge  $k\chi(k)$  vs  $k$  for brominated (solid line) and pristine YBCO( $x \sim 0.6$ ) (dashed line) with x-ray polarization parallel to  $c$ -axis. Cu  $K$ -edge data were corrected for self-absorption as described in Ref. [59].

Synchrotron high resolution x-ray diffraction data were collected at beam line X16B of the National Synchrotron Light Source (NSLS). The diffraction patterns revealed no evidence for secondary crystallographic phases.

XAFS data were collected at NSLS beamlines X23A2 (Cu  $K$ -edge, Si (311) monochromator), X19A (Ba  $L_3$ -edge, Si (111) monochromator), X18B (Br  $K$ -edge, Si (111) monochromator), and X11A (Y  $K$ -edge, Si (111) monochromator) in fluorescence yield (FY) mode at room temperature. Special care was taken to suppress higher order x-ray harmonics. We used a PIPS detector and  $Z-1$  filter to obtain the total FY at Cu  $K$ -, Ba  $L_3$ -, and Y  $K$ -edges and a 13-element Ge detector with an energy resolution of 260 eV to detect the partial  $K_\alpha$  yield at the Br  $K$ -edge. The absolute energy scales were calibrated by a standard procedure [58], using a set of pure metal foils: Cu, Ti, Y, and Pt for Cu  $K$ -, Ba  $L_3$ -, Y  $K$ -, and Br  $K$ -edge data, respectively. Reproducibility of the Cu  $K$ - and Br  $K$ -

edge XANES spectra was achieved through repeated measurements of the studied samples. From two to twelve scans (at Br *K*-edge) were collected to improve the signal-to-noise ratios.

For Cu *K*-edge XAFS measurements the single crystals were aligned so that an angle between polarization vector of oncoming x-rays,  $\mathbf{E}$ , and the surface normal (which coincides with *c*-axis) was  $\phi \sim 20 \pm 5^\circ$ , giving predominantly the  $\mathbf{E} \parallel \mathbf{c}$  spectrum. For the Ba *L*<sub>3</sub>- and Y *K*-edges we used  $\phi \sim 90 \pm 5^\circ$  yielding  $\mathbf{E} \parallel \mathbf{ab}$  spectra. The PIPS detector was placed at  $\phi \sim 60^\circ$  with respect to the direction of the oncoming x-rays. Br *K*-edge measurements were performed at  $\phi \sim 45 \pm 5^\circ$ , with the Ge detector positioned at  $\phi \sim 90^\circ$ . For the above experimental conditions, the sampling depths (x-ray penetration depth) [59] were estimated to be  $\sim 2000 \text{ \AA}$  for Cu *K*-,  $\sim 1400 \text{ \AA}$  for Ba *L*<sub>3</sub>-, and more than  $3000 \text{ \AA}$  for Y *K*- and Br *K*-edges, yielding XAFS measurements that are bulk-sensitive. Further measurements at different grazing angles of the oncoming x-rays beam must be done to address the depth dependence of the bromination.

All spectra except the Br *K*-edge XAFS data were corrected for self-absorption using the atomic absorption coefficients from Ref [60]. We further accounted for the large solid angle of the PIPS detector and for contribution from both Cu *K*<sub>α</sub> and *K*<sub>β</sub> lines. Reduced Cu *K*-edge  $k\chi(k)$  and Br *K*-edge  $k\chi(k)$  are shown in Fig. 6.3. Cu *K*-edge spectra were limited in *k*-space due to Bragg reflections. Ba *L*<sub>3</sub>-edge data were cut off by the Ba *L*<sub>2</sub> edge at  $\sim 9.5 \text{ \AA}^{-1}$ . Upper limits for Br *K*- and Y *K*-edge XAFS spectra ( $\sim 11.5$  and  $15 \text{ \AA}^{-1}$ ) were based on the signal-to-noise ratios in the raw data.

Data analysis were performed according to standard procedures [58]. Usually XAFS analysis is performed on single-phase materials that are checked by x-ray

diffraction and/or EDAX measurements. In brominated YBCO, a mixture of phases some of which are possibly amorphous have been discussed in the literature [52,57]. Therefore, before going into a detailed analysis, we briefly examine the XAFS for a mixture of  $m$ -different phases. Assuming that the typical size of a nanoparticle is larger than 5-6 Å (that is the approximate cut off limit of X-ray absorption spectroscopy) an effective coordination number is given by  $N_{eff} = 3N_j p_m \cos^2(\theta_j)$ , where  $N_j$  atoms at distances  $R_j$ ,  $p_m$  is a partial weight of  $m$ -th nano-phase which follows the normalization rule:  $\sum p_m = 1$ .  $\theta$  denotes the angle between polarization vector of oncoming x-ray and the unit vector pointing along the direction from the absorbing atom to the scattering atom. The structural parameters  $R_j$ ,  $N_j$ ,  $\sigma_j^2$  (Debye-Waller factor) become phase dependent. Phase sensitivity,  $p_m$ , is limited by the typical error in determining  $N_{eff}$  (10 to 20%) . Since Br in Br\_YBCO is at the level of an impurity (1 Br per 30 Cu), neither the Cu  $K$ -edge, Ba  $L_3$  or Y  $K$ -edge XAFS have the potential to determine the Br location with respect to the Cu, Ba, and Y sites.

Instead, Cu  $K$ -, Ba  $L_3$ -, and Y  $K$ -edge XAFS will be used to obtain information on the local structure of the *major phase(s)* created by bromination. Usually, the number of structural parameters available in the fit [61] allows one to consider a mixture of no more than two phases. This simple model, however, appears to satisfy the results of the important experimental observations [52]: One of the phases is associated with the parent YBCO, which might have a slightly modified local structure and oxygen stoichiometry. Another phase accounts for locally decomposed regions (domains) characterizing by possible non-stoichiometric composition and low dimensionality (large local distortions). We shall further discuss the validity of the two-phase approximation (Sect. 6.2) invoking

results of our multiple-edge XAFS analysis. The local structure about specific atomic sites will be expressed in terms of cluster expansions including the first oxygen shell about Cu(1,2) (Sect. 6.1.3.2) and the first two shells about Ba and Y (Sections 6.1.3.4 and 6.1.3.5).

Photoelectron backscattering amplitudes and total phase shifts required to perform the fits [58] were generated by the FEFF-6 code [62] using clusters with a radius  $\sim 8$  Å around the Cu(1,2), Ba, and Y absorption sites. The clusters were constructed using the neutron diffraction data of YBCO ( $y=0.51$ ) [63]. Incorporated Br was ignored, since it was at the level of an impurity. For the decomposed phase we used the same amplitudes and phase shifts as for pristine YBCO. This *ad-hock* approximation will be verified in Sections 6.1.3.2, 6.1.3.4 and 6.1.3.5. This is expected to be satisfactory provided that the decomposed phase mostly consists of nano-fragments of YBCO lattice where the average interatomic distances and the 3D arrangement of atoms are similar to those in YBCO, while the coordination numbers could be different. For the Br K-edge analysis, the amplitudes and phase shifts were initially determined by the FEFF-3 code utilizing atomic potentials. As the location of Br was determined in a first approximation, a cluster about Br atom was assembled and more accurate amplitude and phase shifts were generated by FEFF-6.

### 6.1.3 Experimental Results and Data Analysis

X-ray absorption fine structure (XAFS) measurements were performed at the Br *K*-edge, Cu *K*-edge, Ba  $L_3$  edge and Y *K*-edge to probe the local and atomic structure for the brominated and non-brominated (normal) YBCO single-crystals.

### 6.1.3.1 Br *K*-edge of the Brominated $\text{YBa}_2\text{Cu}_3\text{O}_{6+x}$ ( $x \sim 0.6$ ) Single Crystals

The Br *K*-edge spectrum shown in Fig. 6.3(a) were Fourier transformed to *r*-space over the range of 2.9-11.4 Å using a square window. The resulting magnitude and imaginary parts are plotted in Fig. 6.4. Although the peak heights are relatively small, the multiple shell structure about Br is apparent from the plot.

The complex structure of the Br *K*-edge analysis comes from the fact that neither the chemical composition nor the local structure about Br atoms are known a-priori. In an attempt to refine the structure we will proceed in several steps, narrowing the choice for possible structural models and finally discussing the uniqueness of the fit. As a first step, we estimate contribution from Br-X pair(s) through a back Fourier transformation over the range of 0.7-1.7 Å. Although the first peak is not perfectly separated from the others, the filtered XAFS enables the chemical composition and quantitative structural parameters of the Br nearest neighbor to be determined. It should be mentioned that the peak at  $\sim 1.5$  Å usually corresponds to the oxygen coordination. Bromine-to-metal bonds are characterized by larger interatomic distances. Nevertheless, all four elements constituting YBCO were considered. Results of a direct XAFS simulation over the range 4-10.5 Å showed that the first peak, indeed, corresponded to Br-O pair, while neither of metals or mixtures of metals could fit the data. The best fit reveals Br-O interatomic distance  $R=1.83 \pm 0.02$  Å, DW factor  $\sigma^{(2)}= 0.013 \pm 0.003$  Å<sup>2</sup>, and coordination number  $N=0.9 \pm 0.3$ . Note, that the extracted Br-O distance coincides with Cu(1)-O(4) distance in YBCO. This prompted us to check the hypothesis that Br enters the Cu(1) site of oxygen-deficient YBCO ( $y \rightarrow 0$ ). In order to show that Br-O distribution has no peak at about 1.93

$\text{\AA}$  (that corresponds to Cu(1)-O(1) bond in oxygen-rich YBCO), a two site distribution peaking at 1.83 and 1.93  $\text{\AA}$  was attempted. This two peak fits collapses to a single site distribution at about 1.83  $\text{\AA}$ . In normal YBCO all Cu(1) sites are occupied (the on-site deficiency appears to be well below of the amount of Br introduced in the sample). Therefore, in the framework of our hypothesis, for substituted Br atoms there is one Cu atom removed which is potentially available to be bond to the liberated oxygen or bromine. The latter will be considered in a form of a “nano-copper bromide” (referred to below as CuBr\*), with local structural parameters (Br-Cu interatomic distance, DW factor and coordination number) to be determined along with the structural parameters of the phase with Br in the Cu(1) position.

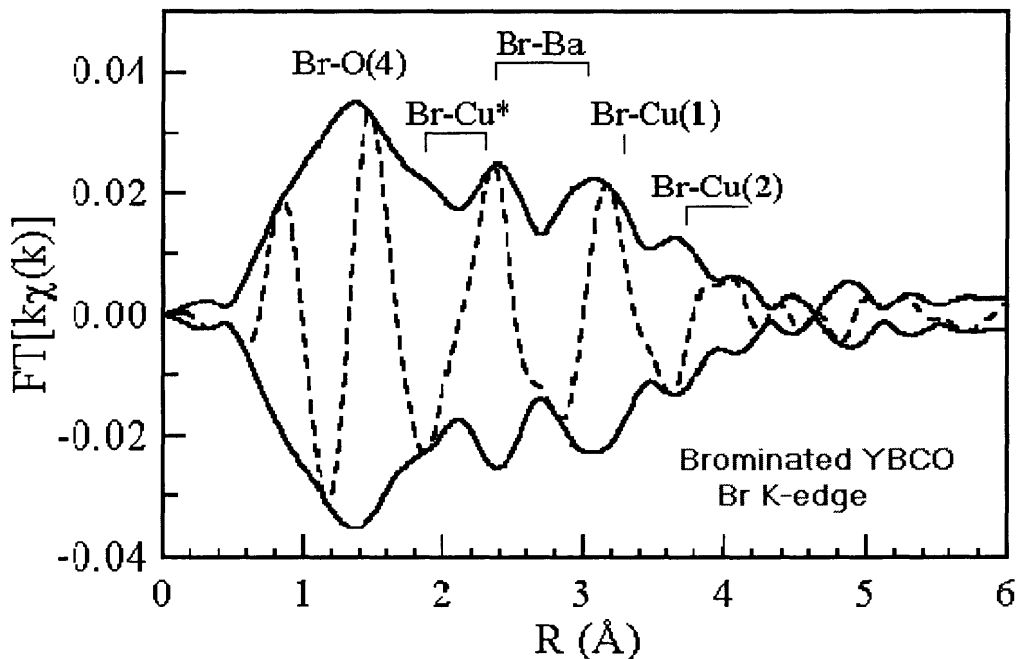


**Figure 6.4** The Fourier transform (FT) of brominated YBCO. The oscillating curve (dashed line) is the imaginary part of the FT. The envelope (solid curve) is the magnitude of the FT. The data are transformed with a square window between 2.9-11.4  $\text{\AA}^{-1}$ . Peak assignment is based on the multiple-shell model.



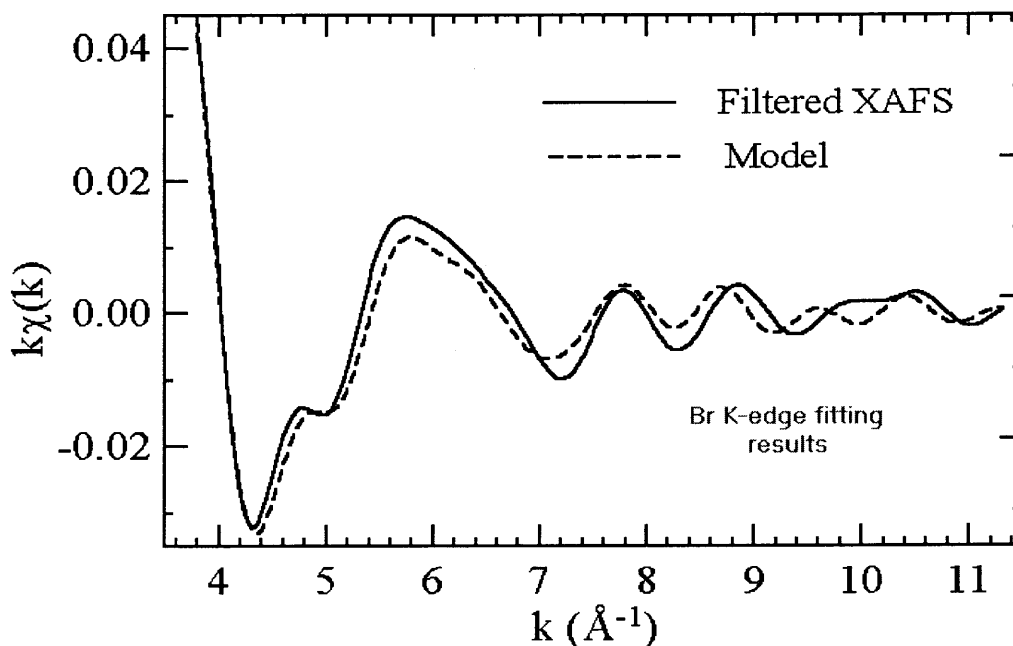


**Figure 6.5** Comparison of the Fourier-filtered data (solid line) with model involving Br - [O(4), Ba, Cu(1,2)] pairs (dashed line). Structural parameters extracted from the non-linear least square fit are provided in Table 6.1.

It is worth mentioning that though our synchrotron x-ray diffraction data ruled out the presence of CuBr in our crystal compared to previous work which reported traces of CuBr [64]. Thus, we considered CuBr\* along with a phase with Br in the Cu(1) position. If the amount of CuBr\* in brominated crystal is negligible then the Br-Cu coordination number should approach zero.

The Fourier transformed  $k\chi(k)$  data were back transformed from 0.7 to 4.26 Å. The resulting XAFS was fit in the single-scattering approximation [65] assuming Br-O(4), Br-Ba, Br-Cu(1), and Br-Cu(2) peaks at 1.83, 2.51, 3.87, and 4.19 Å for the phase with Br in the Cu(1) position and Br-Cu peak at 2.42 Å for the CuBr\* phase. For the fitting range from 3.7 to 11.3 Å<sup>-1</sup> the maximum allowed number of varying parameters is 18 [61]. We performed a constrained fit using 14 free parameters: The energy shift for Br-O shell and  $S_0^2$  factors for all shells were fixed as estimated from the first peak fit

described above. In addition, we constrained all coordination numbers in order to determine the shape of clusters about Br atoms. For instance, if Br is in the Cu(1) position of oxygen-deficient YBCO lattice it has to be two fold coordinated to O(4), eightfold to Ba, fourfold to Cu(1), and twofold to Cu(2). Taking into account the experimental geometry of our polarized Br *K*-edge measurements, the effective coordination numbers should be 3, 5.9, 3, and 3, respectively. If the top four of eight unit cells are missing ( as a result of decomposition reaction occurring upon bromination) the expected effective coordination numbers should be half of those listed above. Clusters of other shapes which are a fraction of the well-aligned "host" lattice can be considered accordingly. We also expanded the search to clusters, which are randomly oriented with respect to the host single crystal structure. We found that to obtain a reasonable fit, the Br-Ba coordination number should not exceed 3/2, thereby limiting number of aligned cells to two units and suggesting an open structure with Br on its surface. If two units are connected along the *c*-axis or either *a*- or *b*-axes then the O(4) coordination number should be 3 or 3/2 – both fall beyond the oxygen coordination of  $0.9 \pm 0.3$  estimated from the first peak fit. The experimental data are better fit with one O(4), Ba, and Cu(2) and two Cu(1) atoms about Br in the Cu(1) site. This set of coordination numbers implies the cluster is randomly oriented with respect to the polarization vector  $\mathbf{E}$ , and, therefore, with respect to the host crystalline structure. The agreement factor for the model is 2.3 times lower than that for the closest competitive model assuming two cells to be combined along *a*- or *b*-axis of the crystal. The coordination number for CuBr\* was found to be 1. Finally, we constrained the energy shifts to values extracted from the previous fit, while allowing the coordination numbers to vary. The best fit is shown by dashed line in Fig. 6.5. It is in

reasonably good agreement with the experimental data. The results are summarized in Table 6.1.

Significantly lower coordination numbers found about the Br atom unambiguously indicate that *Br does not enter the Cu(1) site in the perfect YBCO lattice.* However, good agreement between all four Br-X [X=O(4), Ba, Cu(1),Cu(2)] interatomic distances obtained from the fit suggests that *Br occupies the Cu(1) site in Br-O(4)-Ba-Cu<sub>2</sub>(1)Cu(2)-... nano-clusters (nano-fragments)* which yet retain the 3D structure of the original YBCO lattice. Coordination numbers extracted suggest that those nano-clusters are randomly oriented in the brominated crystal.

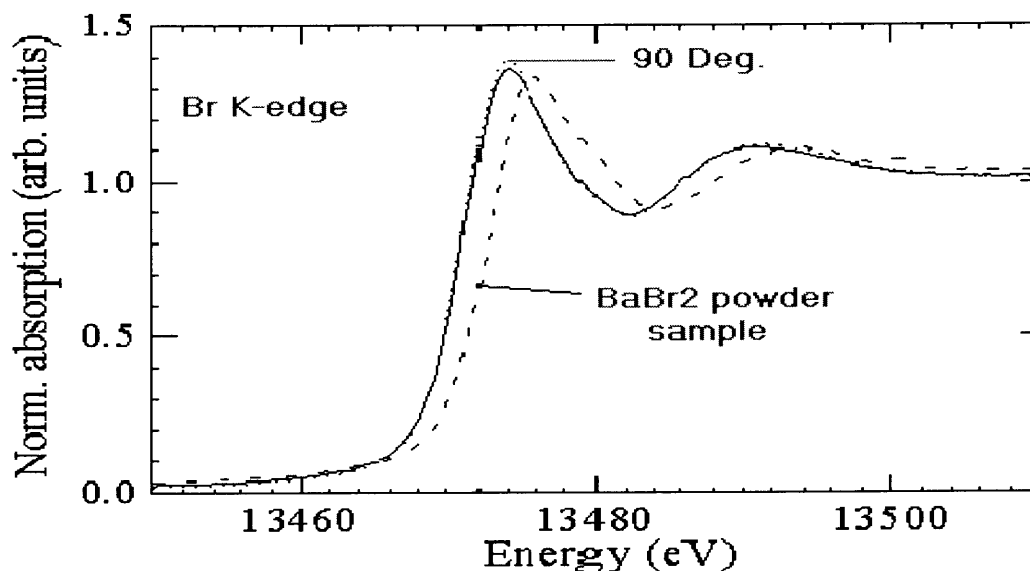


**Figure 6.6** Polarized Br *K*-edge XANES spectra of Br<sub>YBCO</sub>, measured at  $\phi=45^\circ$  (solid line) and  $\phi=90^\circ$  (dotted line). Notice that no polarization dependence is observed implying that Br-O(4)-Ba-Cu(2)<sub>2</sub>Cu<sub>1</sub>-... nanoclusters are randomly distributed with respect to x-ray polarization and, therefore, with respect to host YBCO lattice. Br *K*-edge XANES of powder BaBr<sub>2</sub>·2H<sub>2</sub>O (dashed line) is to show that the formal Br valence in brominated YBCO is close to -1.

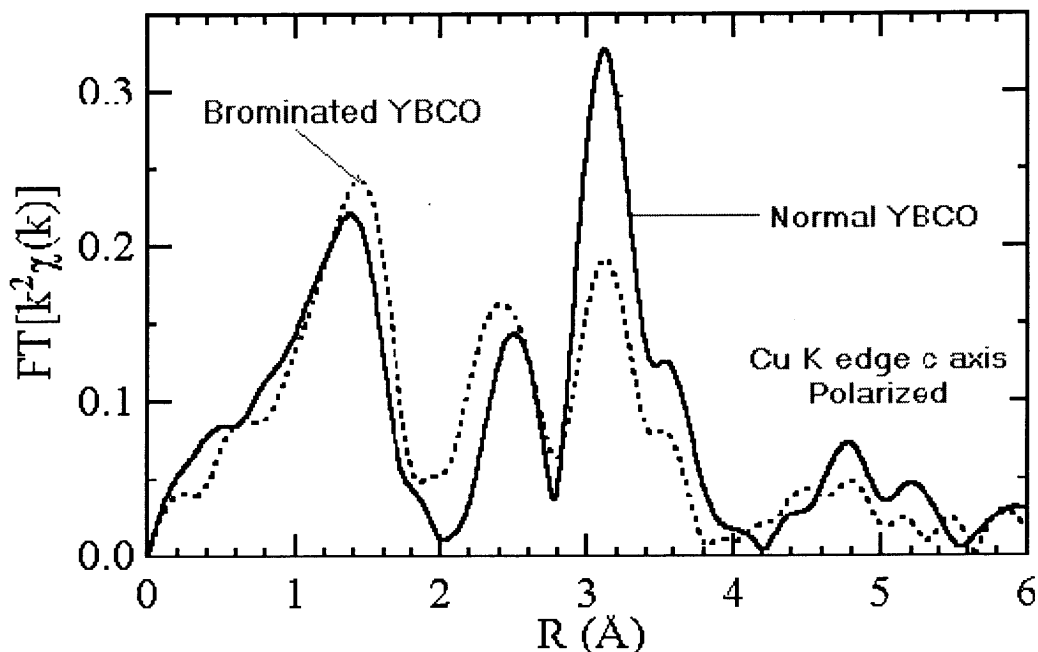


**Figure 6.7** FT of Cu *K*-edge  $k^2\chi(k)$  of untreated (solid line) and brominated (dashed line) YBCO ( $x\sim 0.6$ ). The data are transformed with a square window between 2.5-13.0  $\text{\AA}^{-1}$ . The origin of the peaks is described in the text.

Independent confirmation for this fact comes from absence of polarization dependence of Br *K*-edge x-ray absorption near edge structure (XANES) performed on the same brominated crystal at two different experimental geometries (Sect.6.1.3):  $\varphi=45^\circ$  and  $\varphi=90^\circ$  ( $\mathbf{E}\parallel\mathbf{ab}$ ). As revealed from Fig. 6.6, the detail comparison over the range of 13440-13520 eV shows no essential differences between the two spectra. Such weak polarization dependence is possible if clusters are randomly oriented with respect to the polarization vector  $\mathbf{E}$ , and, therefore, with respect to the oriented host crystalline structure.

**Table 6.1** Local structural parameters obtained from the constrained fit of the Fourier filtered Br *K*-edge  $k\chi(k)$  data.  $S_o^2$  was estimated to be 0.72 from the first peak fit. Neutron-diffraction results on YBCO( $x=0.51$ ) [67] are given for comparison of Cu(1)-X interatomic distances and number of neighbors. Parameters for conventional CuBr powder are taken from [68]. Errors in the parameters were estimated from the covariance matrix generated from the fit and should be taken as relative errors corresponding to the reproducibility of the XAFS data.

Br K-edge		XAFS		Neutron diffraction		
Bond	R (Å)	No. of neighbors	$\sigma^{(2)} \times 10^3$ (Å <sup>2</sup> )	Bond	R(Å)	No. of neighbors
Br - O(4)	1.84±0.02	1.0±0.1	13±2	Cu(1) - O(4)	1.8325	2
Br - Ba	2.51±0.03	1.0±0.2	21±5	Cu(1) - Ba	2.5140	8
Br-Cu(1)	3.89±0.03	2.2±0.4	15±5	Cu(1) - Cu(1)	3.8392	2
					3.8791	2
Br - Cu(2)	4.16±0.04	1.0±0.3	10±3	Cu(1)-Cu(2)	4.1932	2
Br-Cu (in BrCu*)	2.45±0.04	1.2±0.4	27±9	Br-Cu in BrCu		4

Considering the uniqueness of the obtained solution, it is worth recalling that the single scattering (SC) fit to XAFS data provides interatomic distances and coordination numbers, but not a 3D picture of the clusters about the absorption site. In turn, this raises a question on the phase composition- Whether Br-O-Ba-Cu<sub>3</sub>-... is a well-defined nano-phase or the structure (probed as an average over the bulk) is a mixture of simpler nano-fragments, like Br-O and Br-Ba with the same interatomic distances and coordination numbers as listed in Table 6.1. Either scenario would be in line with the XAFS refinement. The 3D structure could be accessed either through detail analysis of multiple-scattering (MS) terms which are basically small additions to the SC contribution in the strongly distorted compounds or through analysis of XANES spectra which are dominated by the MS contributions. For moderate signal-to-noise ratio achieved in Br *K*-

edge XAFS spectra (Fig. 6.3(a)) the XANES analysis appears to be preferred. Below, we will restrict our discussion to quantitative analysis of normalized Br *K*-edge XANES spectra shown in Fig. 6.6, while leaving detail MS simulations to be done in a further work. Bromine in Br-O and Br-Ba nano-fragments, if any, would have to have formal valence states of about (+1) and (-2). The position of the main edge depends on formal valence of the absorbing atom, showing an upward shift of the main line position as the formal valence increases. The XANES spectra from two phases with different valence is expected to display additional peaks associated with those valences or, at least, to be broadened compared to XANES spectrum of a single phase characterized by some specific valence state. As seen from Fig. 6.6, the Br *K*-edge of brominated YBCO does not exhibit additional structures. Comparison with the Br *K*-edge of BaBr<sub>2</sub>·2H<sub>2</sub>O reveals that, they are very much alike, indicating the *formal* Br valence in brominated YBCO to be -1, and, therefore eliminating the model of mixed Br-O and Br-Ba nano-phases as possible products of bromination.

### 6.1.3.2 C-axis Polarized Cu *K*-edge EXAFS for Brominated (non-brominated) YBCO Single Crystals

The magnitudes of Fourier-transform (FT) spectra of the c-polarized Cu-*K*-edge  $k^2\chi(k)$  of normal and brominated samples are shown in Fig. 6.7. The first peak (~0.8-2.1 Å) corresponds to Cu(1)-O(4) and Cu(2)-O(4) pairs. A multi-peak structure (~2.3-4.2 Å) is due to combined contributions of Cu(2)-Y, Cu(2)-Cu(2), Cu(1,2)-Ba, Cu(1)-Cu(2), and Cu(2)-O(2,3,4) single-scattering as well as several multiple-scattering paths. Since the first peak is well separated, it was isolated through a back FT to *k*-space. A good fit to the  $k^2\chi(k)$  filtered data was achieved revealing Cu(1)-O(4) and Cu(2)-O(4) distances of

1.83±0.01 and 2.33±0.02 Å, in good agreement with the results of neutron diffraction for YBCO( $x=0.51$ ) single crystals [63]. Results of the fit (including Y, Ba, and Cu environment) are listed in Table 6.2. It's worth mentioning that although there is no obvious beat at  $\sim 12 \text{ \AA}^{-1}$  at room temperature, the DW factors for Cu(2)-O(4) and Cu(2)-Cu(2) pairs are abnormally large (2-3 times larger than those for YBCO ( $x\sim 0.95$ ) [66]) implying the Cu(1,2)-O(4) and Cu(2)-Cu(2) pair distributions to be more complex than a single site distribution. Apparently, this makes the  $x\sim 0.5$  composition a better choice to explore a possible splitting of the O(4) position [66,67] and suggested out-of-plane displacements of the Cu(2) atoms [68]. A detailed temperature-dependence study is required.

Comparing the FT spectra of the normal and brominated samples we note a very unusual behavior of the first Cu-O peak, it is shifted to higher  $r$  with increased intensity, while the Cu-Y, Cu-Cu, Cu-Ba peaks are reduced presumably due to structural disorder accompanying the bromination. Detail analysis of Cu-Y, Cu-Cu, Cu-Ba shells in a framework of a two-phase model requires a larger number of fit parameters than is allowed by the  $E||c$  data, and, therefore it is not attempted in this work. We will focus on the Cu-O pair correlations. Fits to the filtered Cu-O shells were performed in terms of three constrained models which differ in the number of Cu-O shells. Model 1S corresponds to a single Cu-O bond with a mean distance of complex Cu-O pair distribution, possibly in a multiphase sample. Model 2S describes the typical YBCO structure in  $E||c$  geometry: two Cu(1,2)-O(4) distances and corresponding coordination numbers were allowed to vary, while the number of the pairs were fixed to 2. Note, that 2S is explicitly a single-phase model. Finally, we considered the 3S model assuming a

2:1 mixture of two phases: one has Cu(1,2)-O(4) pairs typical of YBCO family, while the other is characterized by an average Cu-O bond length of about 1.95 Å. The origin of the latter bond will be briefly discussed.

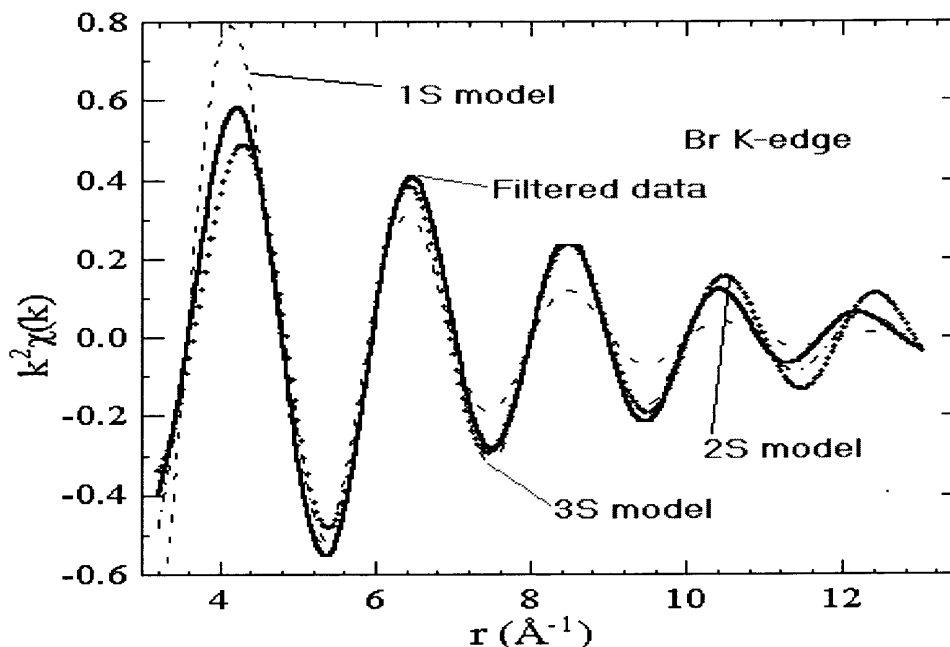


**Figure 6.8** Comparison of the Fourier-filtered Cu-O contribution to c-axis polarized with three structural models for the Cu-O pair distribution in Br<sub>x</sub>YBCO. The back FT range is 1-2.1 Å, using a square window. A three-shell model providing the best fit to the filtered data assumes two Cu-O distances resembling to Cu(1)-O(4) and Cu(2)-O(4) in optimally doped single-crystal YBCO ( $x \sim 0.9-1$ ) and more Cu-O distance (1.95 Å) due to the decomposed phase. The latter distance is mostly responsible for increase of the Cu-O peak intensity seen in Fig. 6.7 for the brominated YBCO sample



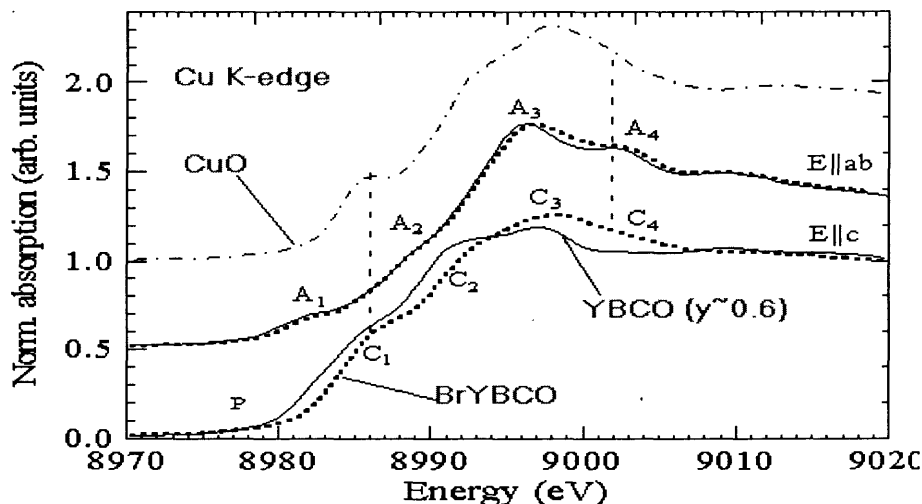


**Figure 6.9** Effect of bromination on the Cu *K*-edge XANES of YBCO( $x \sim 0.6$ ) measured with x-ray polarization vector parallel to the *c*-axis ( $E \parallel c$ ) and parallel to the *ab*-plane ( $E \parallel ab$ ). Cu *K*-edge XANES spectrum of the CuO powder (dot-dashed line) and ( $E \parallel ab$ ) spectra are offset for clarity.

Before proceeding with the fit, we constructed a difference:  $k^2[\chi_B(k) - \alpha \chi_N(k)]$ , where  $\chi_B(k)$  and  $\chi_N(k)$  refer to brominated and normal samples, and  $\alpha = 2/3$ . Fits to the first-shell data gave  $3.8 \pm 0.5$  oxygen neighbors at  $1.95 \pm 0.01$  Å, with a very small DW factor ( $\sim 0.0015$  Å<sup>2</sup>). It is therefore highly unlikely that this peak is composed of several different Cu-O distances. Next, the Cu-O peak of the difference  $k^2[\chi_B(k) - \alpha \chi_N(k)]$  was fit as a function of the parameter  $\alpha$ . A single-site distribution allowing  $R$ ,  $\sigma^{(2)}$ , and  $\Delta E_0$  parameters to vary freely, while holding the number of oxygen neighbor to four was employed. We found that an agreement factor (defined in the caption to Table 6.2) has a flat minimum at  $\alpha \sim 0.6$  which validates the ratio 2:1 used in the 3S model.

**Table 6.2** Local structural parameters obtained from the constrained fit of the Fourier filtered Cu  $K$ -edge  $k\chi(k)$  data.  $S_o^2 = 0.8$  for all Cu-O bonds and 0.9 for all other bonds. Three models (S1-S3) of Cu-O pair distribution are constructed as described in the text. Reduced agreement factor,  $R_a = 1/(\gamma M) \sum_i^M k(\chi_i^{\text{exp}} - \chi_i^{\text{calc}})$ , where  $M$  is the number of data points, and  $\gamma$  is the number of degrees of freedom in the fit. S1-model does not pass the  $\chi^2$ -test for the quality of the fit to the filtered data, while both S2 and S3 do. Neutron-diffraction results on YBCO( $x=0.51$ ) [67] are given for comparison of Cu(1)-X interatomic distances and the number of neighbors.

Sample	Bond	Cu	K-edge	XAFS		Neutron	diffraction
		R (Å)	N	$\sigma^{(2)} \times 10^3 (\text{Å}^2)$	$R_a \times 10^3$	R(Å)	N
YBCO ( $y=6.6$ )	Cu(1)-O(4)	1.83±0.01	2*	3.3±0.4		1.8325	2
	Cu(2)-O(4)	2.33±0.02	2*	18±4		3.3607	2
	Cu(2)-Y	3.21±0.02	4.3±0.4	4.4±0.6		3.2026	4
	Cu(2)-Cu(2)	3.35±0.04	1.1±0.2	24±9		3.3527	1
	Cu(2)-Ba	3.41±0.02	7.8±0.8	4.1±0.5		3.3711	8
	Cu(1)-Ba	3.51±0.03	4.5±0.6	9.2±1.5		3.5140	4
	Cu(2)-Cu(1)	4.19±0.03	4.8±1.0	10.0±2.0		4.1932	4
Br_YBCO 1S-model	Cu-O	1.91±0.01	4*	11.6±1.0	6.7		
Br_YBCO 2S-model	Cu(1)-O(4)	1.91±0.01	2*	2.2±0.2	4.7		
	Cu(2)-O(4)	2.33±0.02	2*	22±8			
Br_YBCO 3S-model	Cu(1)-O(4)	1.85±0.01	4/3*	2.5±0.5			
	Cu(2)-O(4)	2.29±0.02	4/3*	14.3±2.1	3.3		
	Cu(2)-O(2,3)	1.95±0.01	4/3*	1.3±0.3			

\* Fixed in the fit.

The best-fit curves corresponding to three models are plotted in Fig.6.8 along with the Fourier-filtered contribution from Cu-O peak. Model S1 (dashed line) gives a poor

fit. It doesn't pass the  $\chi^2$ -test. Model 2S (dots) demonstrates a good agreement to  $k \leq 10 \text{ \AA}^{-1}$ , deviating above. The estimated shortest Cu-O distance of 1.91  $\text{\AA}$  appears to be unrealistically long for a Cu(1)-O(4) bond in YBCO( $0 < x < 1$ ). Model S3 (dot-dashed line) provides a fit over whole range, yielding the lowest (among the competing models) reduced agreement factor-  $R_a$  (Table 6.2). Two observations are important in order to understand the mechanism for the restoration of superconductivity in the brominated sample:

(i) Cu(1,2)-O(4) distances and corresponding DW factors associated with the parent YBCO phase are similar to those expected in optimally doped crystals ( $x \sim 0.9-1$ ) [66];

(ii) The intermediate Cu-O distance ( $1.95 \pm 0.01 \text{ \AA}$ ) is remarkably similar to the Cu(1)-O(1) Cu(2)-O(2) and Cu(2)-O(3) bond lengths which for YBCO( $x=0.51$ ) are equal to 1.928, 1.936 and 1.955  $\text{\AA}$ , respectively [63]. Note that in  $\mathbf{E} \parallel \mathbf{c}$  geometry there should be no contribution from the above bonds in the Cu-O XAFS unless these bonds are misaligned with respect to the  $c$ -axis of the brominated crystal. The Cu-O bonds at a distance of 1.95  $\text{\AA}$  should be viewed as constituting the secondary (decomposed) phase incorporated by the "host" YBCO lattice.

### 6.1.3.3 Polarized Cu $K$ -edge XANES for Brominated and Normal YBCO Single Crystals

Polarized Cu  $K$ -edges of normal and brominated YBCO ( $x \sim 0.6$ ) measured for  $\mathbf{E} \parallel \mathbf{c}$  and  $\mathbf{E} \parallel \mathbf{ab}$  are shown in Fig. 6.9. To ascertain the dominant trend in the XANES upon bromination we compare our polarized data with those for two oriented powders of YBCO ( $x \sim 0.23$  and 1.) reported by Tranquada *et al* [69] in their figure. 2. In  $\mathbf{E} \parallel \mathbf{c}$

geometry, the XANES spectra of both brominated YBCO and YBCO ( $x \sim 1$ ) (from Ref. [69]) are shifted (non-rigidly) towards the low energy by  $\sim 1.5$  eV, compared to spectra of the normal YBCO and YBCO( $x \sim 0.23$ ) samples. The main feature  $C_3$  decreases, while the  $C_2$  shoulder becomes more pronounced. In the  $\mathbf{E} \parallel \mathbf{ab}$  geometry, the peak  $A_1$  and, to a smaller extent, the shoulder  $A_2$ , are suppressed as a result of both bromination and the increase of  $x$  from 0.23 to 1 in the oriented powder. Such a behavior is in line with the general thought that re-oxygenation of sample takes place at the expense of decomposition [52]. Decomposition implies the appearance of additional phases (products of the reaction). Careful inspection of our polarized spectra reveals several differences between brominated and fully oxygenated samples (from Ref. [69]). In  $\mathbf{E} \parallel \mathbf{c}$ , the shoulder  $C_1$  is very weak in YBCO ( $x \sim 1$ ) (Ref. [69]), while it's very apparent in our brominated sample. One might notice, that this feature gets even stronger upon bromination of YBCO ( $x \sim 0.6$ )- in reverse order to the observed trend upon oxygenation. Bromination gives rise to additional spectral intensity at the  $A_4$  and  $C_4$  features, which are clearly beyond the limits observed as  $y$  goes from 0.23 to 1. Lastly,  $\mathbf{E} \parallel \mathbf{c}$  and  $\mathbf{E} \parallel \mathbf{ab}$  spectra of Br\_YBCO are smoother than any spectrum of YBCO (regardless of the oxygen content), implying that the local structure of Br\_YBCO is strongly distorted and/or the sample is composed of different phases.

Interestingly, the mentioned differences can be satisfactorily understood by assuming that Br-YBCO contains an admixture of a decomposed phase that, in a first approximation, is reminiscent of "CuO powder" shown in Fig. 6.9 by the dot-dashed line. Difference spectra for 100% of Br\_YBCO and 66% untreated YBCO ( $x \sim 0.6$ ) were formed for both polarizations. Being normalized to unity in the extended area they are

plotted in Fig.6.8 along with the normalized spectra of CuO powder. The  $E||c$  difference is also shifted by -1.3 eV to match the CuO data. Energy positions of all major peaks in the  $E||c$  difference spectrum and the spectrum of CuO powder almost coincides although the magnitudes of these peaks are slightly different. The  $E||ab$  difference of the brominated sample retains weak features of original  $E||ab$  polarized spectrum ( $A_1$  and  $A_4$ ) which don't match those of CuO powder. However, their major peaks and oscillations in the extended area ( $E > 9010$  eV) coincide reasonably well. Note, that the decomposed phase is neither completely amorphous nor is it completely randomly oriented with respect to the major phase. Weak polarization dependence is seen in Fig. 6.10, presumably due to different orientation of decomposed domains with respect to the host lattice.

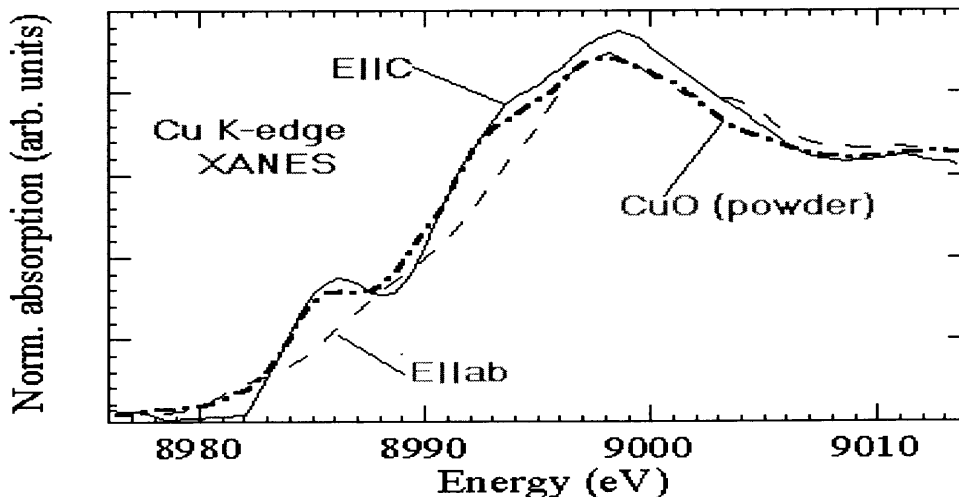


**Figure 6.10** Contribution to the Cu K-edge XANES from the decomposed phase. The residual Cu K-edge polarization dependence implies that domains forming the decomposed phase are differently ordered with respect to the polarization vector whereas the impurities domains Br-O-Ba-Cu-... and Br-Cu are randomly oriented. The XANES spectrum of the powder CuO is shown by the dot-dashed line for comparison.

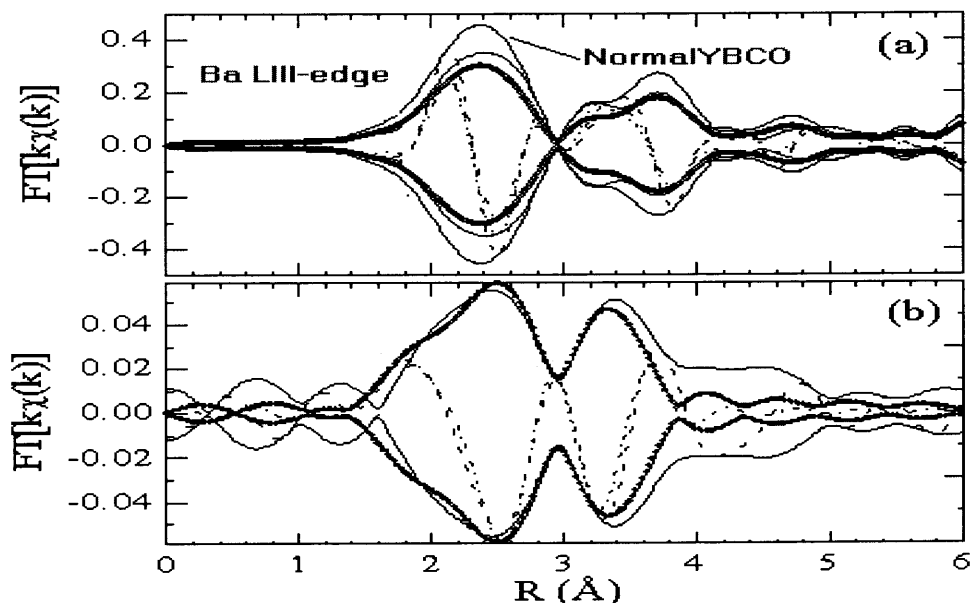


**Figure 6.11** Fourier transform at the Ba  $L_3$ -edge  $k\chi(k)$  (a) Magnitude and imaginary parts of Normal and brominated YBCO single crystals. The Fourier Transform range is  $1.8-9 \text{ \AA}^{-1}$  with a square window. (b) Fit to the FT of  $k\chi(k)$  Performed in  $r$ -space for  $1.7-3.7 \text{ \AA}$ . The constrained fit includes Ba-O,-Cu(1,2) Y and Ba-Ba shells.

#### 6.1.3.4 Ba $L_3$ -edge XAFS of Brominated and Normal YBCO Single Crystals

Magnitudes and imaginary parts of the Fourier-transformed  $k\chi(k)$  spectra of normal and brominated crystals are shown in Fig 6.11(a). In untreated YBCO the first peak corresponds to three Ba-O groups at 2.74, 2.87, and 2.98  $\text{\AA}$  [63]. The second double-peak structure is dominated by Ba-Cu(1,2), Ba-Y and Ba-Ba contributions. The peaks heights for brominated sample are reduced. In the same plot the magnitudes and imaginary parts of normal YBCO are to be scaled to 2/3 of their original value. For  $R > 3.5 \text{ \AA}$  the spectra are almost identical to those of the brominated sample. To analyze the local structure of the decomposed phase, the difference of the 100% brominated signal and 66% of the as-prepared YBCO ( $x \sim 0.5$ ) was computed. We will ignore the interference between the  $p \rightarrow d$  and  $p \rightarrow s$  channels in Ba  $L_3$ -edge XAFS since the decomposed phase shows weak

polarization-dependence and the contribution of the  $p \rightarrow s$  channel is significantly weaker than that of the  $p \rightarrow d$  channel. The Fourier transform of the resultant  $k\chi(k)$  spectrum consists of two peaks, which are assigned to Ba-O and Ba-Cu, Ba-Y, and Ba-Ba bonds [Fig. 6.11(b)]. Because of the short available range in the  $k$ -space, a single-distance Ba-O distribution was considered. The best fit is shown in Fig. 6.11(b). Extracted parameters are summarized in Table 6.3.

The local structure of the decomposed phase with respect to the Ba site is given by a cluster expansion  $\text{Ba-O}_8\text{-Cu(2)}_4\text{Cu(1)}_2\text{-YBa}_2\text{-...}$ . Importantly, only two of four Ba-Cu(1) bonds (which are only  $\sim 0.1$  Å longer than Ba-Cu(2)) were observed in the fit. This is consistent with Br  $K$ -edge data implying homogeneity of the Cu(1)-O(1) planes as Br is substituted in the Cu(1) position of the fragmented lattice and with the Cu  $K$ -edge XANES results as we shall discuss in Sect. 6.3.

**Table 6.3** Results of Ba  $L_3$ -edge XAFS analysis of the decomposed phase.  $S_0^2 = 0.95$ . Errors in numbers of Ba neighbor are below 25%. The constrained parameters are taken from neutron-diffraction results on YBCO ( $x=0.51$ ). The loss of the XAFS signal in the medium-to-long range pair correlations ( $R > 4$  Å) is probably due to cancellations of these contributions in the aperiodic media.

Sample	Bond	R, (Å)	DW (Å <sup>2</sup> )	N
	Ba-O	2.82	0.029	8
	Ba-Cu(2)	3.40	0.005	4*
$k\chi(k)$ difference	Ba-Cu(1)	3.51	0.008	2
Br_YBCO – 0.66*YBCO	Ba-Y	3.80*	0.003	1*
	Ba-Ba	3.85*	0.003	2 *

\*Fixed in the fit

### 6.1.3.5 Y *K*-edge XAFS of Brominated and Normal YBCO Single Crystal

The Fourier transformed  $k\chi(k)$  data of normal and brominated sample are compared in Fig 6.12. The first three peaks correspond to Y-O(2,3), Y-Cu(2), and Y-Y pairs. In contrast to Cu *K*- and Ba  $L_3$  edges, Y *K*-edge data exhibit only minor changes upon bromination. Structural parameters for the oxygen and copper shells of normal and brominated sample are summarized in Table 6.4. Since the changes are small, application of the two-phase model used in the previous sections is not obvious. Therefore fits were performed to the Y *K*-edge data of Br YBCO and YBCO corresponding to single-phase and two-phase models. This implies that the local distortions in Y-O(2,3) and Y-Cu(2) pairs are homogeneously distributed throughout the sample. The latter associates the local distortions with the decomposed phase, while the major phase remains undistorted. Following the previous results, the mixture of major and distorted phase was fixed at 2:1. All atomic parameters for the undistorted phase were further constrained as determined from our XAFS fit of normal YBCO( $x \sim 0.6$ ). Both models gave very similar agreement factors. Therefore, the data are consistent with either model. Y-O(2,3) and Y-Cu(2) distances and oxygen and copper coordination numbers remain the same within the resolution of our experiment and are consistent with the diffraction results (Table 6.4). The only parameters to differ in the models are the DW factors, which are slightly larger in the distorted phase. As will be shown in the next section, combined analysis of the Cu *K*-, Ba  $L_3$  and Y-*K* edge data require a mixture of two phases. *However, regardless of the model used for the Y *K*- edge data, the extracted structural parameters provides clear evidence that the local structure of the superconducting Cu(2)-O(2,3)<sub>2</sub> planes is not affected by bromination.*



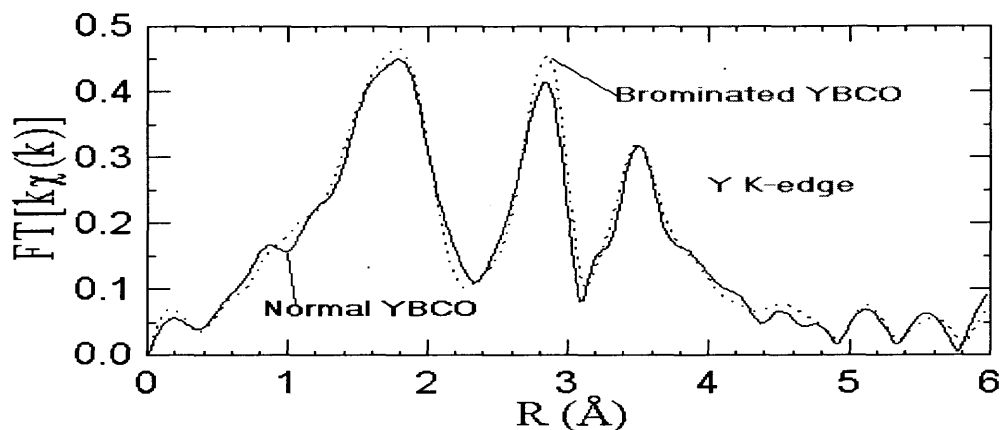


**Figure 6.12** FT of Y *K*-edge  $k\chi(k)$  of untreated (solid line) and brominated (dashed line) YBCO ( $x \sim 0.6$ ). The data are transformed with a square window between  $1.9\text{--}14.7 \text{ \AA}^{-1}$ .

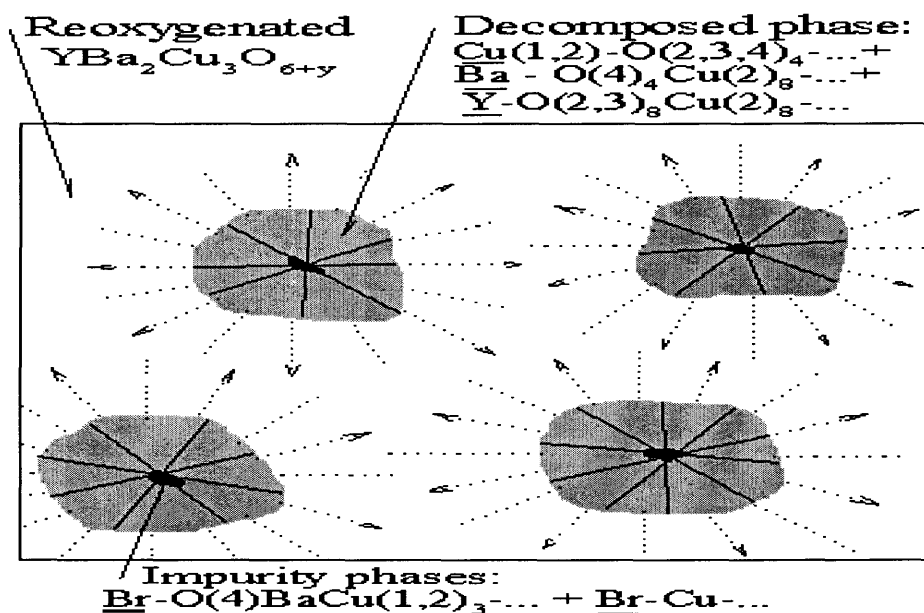


**Figure 6.13** Polarized Cu *K*, Y *K*, Ba *L*<sub>3</sub> and Br *K*-edge measurements are consistent with nanoscale heterogeneity in brominated YBCO ( $x \sim 0.6$ ). Well ordered, undistorted YBCO lattice hosts differently and heavily distorted decomposed inclusions (gray regions) which account for about 1/3 of the volume. The decomposed phase consists of nano-fragments (nano-domains) formed as a result of truncation of the YBCO lattice predominantly along the Cu(1)-O(1) planes. The typical size of the decomposed areas is unknown but is expected to be no less than  $7\text{--}8 \text{ \AA}$  since bromine enters the Cu(1) site forming impurity phases (small black regions inside the gray ones) causing at least 8 unit cells to decompose. The local structure of the host lattice coincides with the fully oxygenated YBCO one, presumably due to reoxygenation of the YBCO ( $x \sim 0.6$ ) by O(1) diffusing from the decomposed regions. The decomposed and impurity phases are given in terms of cluster expansion.

## 6.2 Discussion

Previous SEM and EDAX measurements on YBCO ceramic addressed the macroscopic and chemical homogeneity at scales of several hundred angstroms and larger [70]. Br treatment of YBCO increases the grain size and porosity. Larger grains are elongated along certain directions, but they do not precipitate secondary phases and have the same chemical composition as untreated YBCO. In our attempt to address the chemical composition on an atomic scale we rely on a multiple-edge XAFS analysis.

**Table 6.4** Local structural parameters for the oxygen and copper shells about the yttrium in normal and brominated YBCO( $x \sim 0.6$ ). Parameters are derived from the non-linear least square fit to the Fourier filtered  $k\chi(k)$  data. Back FT ranges were 1.4-2.2 and 2.3-3.1 Å, respectively. From the fit of normal YBCO the  $S_0^2$  was estimated to be 0.9 and was fixed in the refinement of Br\_YBCO. Only parameters referring to the distorted (decomposed) phase are listed for the two-phase model since the parameters for the undistorted phase were constrained to those in normal YBCO (first two rows in this Table). Neutron-diffraction results on YBCO( $x=0.51$ ) [67] are given for comparison.

Sample	Y- K edge		XAFS		Neutron	diffraction
	Bond	R (Å)	N	$\sigma^{(2)} \times 10^3$ (Å <sup>2</sup> )	R (Å)	N
Normal	Y-O(2,3)	2.39±0.01	8.2±1	4.1±0.5	2.3922/24082	4/4
YBCO ( $x \sim 0.6$ )	Y-Cu(2)	3.22±0.01	7.8±1	4.4±0.4	3.2026	8
Br_YBCO (single phase)	Y-O(2,3)	2.39±0.01	7.9±1	4.3±0.5		
	Y-Cu(2)	3.22±0.01	8.0±1	4.9±0.6		
Br_YBCO distorted phase	Y-O(2,3)	2.40±0.01	2.4±0.3	5.8±0.7		
	Y-Cu(2)	3.21±0.01	2.7±0.3	5.4±0.7		

It has been shown in Sections 6.1.3.2. – 6.1.3.5 that the local structure of the distorted phase about Cu, Ba, and Y sites can be expressed as the cluster expansions:  $\text{Cu}(1,2)\text{-O}_4 - \dots$ ,  $\text{Ba-O}_8 - \text{Cu}(2)_4\text{Cu}(1)_2 - \dots$  and  $\text{Y-O}(2,3)_8\text{-Cu}(2)_8 - \dots$ . Corresponding expansions of the single phase  $\text{YBa}_2\text{Cu}_3\text{O}_{6+x}$  are:  $\text{Cu}(1,2)\text{-O}(2,3,4)_4\text{O}(1)_{2/3+x} - \dots$ , Ba -

$O(4)_4 - Cu(2)_8Cu(1)_{4-x}$ , and  $Y - O(2,3)_8 - Cu(2)_8$ .... The difference in local chemical compositions (in  $O(1)$  and  $Cu(1)$  stoichiometry) about  $Cu(1)$  and  $Ba$  sites affirms that a decomposition reaction does take place. The decomposed phase is not YBCO with  $0 < x < 1$ .  $Ba$ -,  $Y$ - and  $Cu$ -oxides ( $BaO$ ,  $Y_2O_3$ ,  $Cu_2O$ , and  $CuO$ ) or barium cuprates ( $BaCuO_2$ ,  $Ba_2CuO_3$ , ..) which are often seen in the literature as likely components of the decomposed phase. However, even if they are considered in the form of nano-particles (with typical size of  $\sim 10-20\text{\AA}$  and larger) and therefore do not scatter elastically- they cannot provide all three components listed above. For instance,  $Y_2O_3$  oxide has an oxygen shell about the  $Y$  similar to YBCO, but does not have  $Y-Cu$  pairs. In both  $BaO$  and YBCO, the  $Ba$  atom is fourth-oxygen(4) coordinated.  $Ba-O$  distances are very much alike in these compounds. However, an assumption on  $BaO$  oxide cannot explain observation of  $Ba-Cu$  pairs revealed by  $Ba L_3$  edge XAFS. The presence of  $Y-Cu$  and  $Ba-Cu$  pairs causes the decomposed phase to differ from that of  $CuO$  oxide.

Before we construct a pictorial view of brominated YBCO we would like to make four points:

(i) Oxygenation of the pristine YBCO phase takes place at the expense of de-oxygenation of the decomposed phase. Indeed, bromination in the nitrogen atmosphere employed in this work excludes external oxygenation. A chemical balance implies that if oxygenation of one of the phases to take place then at least that amount of oxygen had to diffuse from the other decomposed region. In YBCO ( $x \sim 0.6$ ) the most likely candidates for diffusion are  $O(1)$  atoms which are well known to be quite mobile at  $T=260^\circ\text{C}$  (temperature of bromination). The current multiple-edge analysis provide supporting evidences for  $O(1)$  diffusion from the decomposed to superconducting phase:  $Y K$ -edge

XAFS data revealed that the local structure of  $\text{CuO}_2$  planes composed of  $\text{Cu}(2)\text{-O}(2,3)$  atoms is preserved. Cu-O coordination numbers extracted from Cu  $K$ -edge XAFS fit requires non-zero oxygen coordination about the  $\text{Cu}(1)$  site. (Otherwise, the total coordination number about Cu falls beyond the estimated error bar). Ba  $L_3$  edge XAFS analysis confirm Cu  $K$ -edge data showing Ba to be four-fold oxygen coordinated. Thus, Y-edge XAFS imply that  $\text{O}(2,3)$  sites are heavily populated, while Cu  $K$ - and Ba  $L_3$  edge XAFS analysis ensure that  $\text{O}(4)$  sites are populated as well. Therefore, by exclusion, among all oxygen sites in the decomposed phase only the  $\text{O}(1)$  occupancy is altered. The nature of the changes in Cu  $K$ -edge XANES (Sect. 6.1.3.3.) suggests an increase of overall oxygen concentration in the well-ordered phase due to the population of vacancies in  $\text{O}(1)$  sites. The same is evidenced by Cu  $K$ -edge XAFS analysis of the Cu-O pair distribution along the  $c$ -axis. It is well known from the diffraction measurements that the difference between  $\text{Cu}(2)\text{-O}(4)$  and  $\text{Cu}(1)\text{-O}(4)$  distances decreases from 0.42 to 0.33 Å as  $y$  increases from 0.5 to 0.95 [63]. The trend is clearly seen from Cu  $K$ -edge XAFS results (Table 6.2) as one goes from pristine to brominated crystals.

(ii) There might be a mechanism disfavoring the formation of macroscopic decomposition. As we know from the literature [71] the concentration of Br in the underdoped samples is much larger than in oxygen-rich YBCO (for the same condition of bromination). We suggest that Br locally decomposes YBCO ( $x \sim 0.6$ ) and liberates  $\text{O}(1)$  atoms which enters empty neighboring  $\text{O}(1)$  sites driving local oxygen content to the optimal level, and, thereby, preventing a new nucleus of the decomposed phase from being created nearby.

(iii) Combined analysis of the three cluster expansions about Y, Ba, and Cu sites shows that the decomposed phase consists of nano-fragments of YBCO. Cu *K*-edge polarization-dependent measurements indicate the nano-fragments to be misoriented with respect to the host lattice.

(iv) Cu *K*-edge XANES data imply that the local structure of YBCO nano-fragments forming the decomposed phase is broken about the Cu(1)-O(1) planes. In the perfect YBCO structure both Cu(1) and Cu(2) sites contribute to the total x-ray absorption cross section, providing 1/3 and 2/3 of total signal, respectively. Differential XANES spectra are similar to CuO oxide (Fig. 6.8), i.e. the major signal comes from the Cu(2) sites while the contribution from Cu(1) sites is effectively diminished. This condition is met if local environment about Cu(1) is strongly disturbed. With respect to (i), losses of O(1) atoms which are the nearest neighbor of Cu(1) are not sufficient- the differential spectra have little resemblance to Cu *K*-edge XANES of YBCO( $x \sim 0$ ) powder. Results of multiple-scattering (MS) simulations performed for a cluster of 42 atoms about the Cu(1) site shows that the strongest suppression is achieved when the cluster is fragmented rather than just locally distorted from the perfect YBCO structure. It is due to fragmentation that the original coordination is altered for all Cu(1)-X (X= O, Ba, Y,) reducing dramatically the degeneracy of the MS paths. The discontinuation along the Cu(1)-O(1) planes is further supported by the Ba  $L_3$ - edge XAFS analysis suggesting a smaller number of Ba-Cu(1) pairs than in YBCO.

Using this information we propose a structural model of a brominated sample depicted in Fig. 6.13. In terms of a two-component model about 1/3 of the YBCO lattice is locally decomposed but is incorporated into a well-ordered "host" lattice as nano-scale

second phase. The decomposed phase consists of heavily distorted domains that are differently oriented with respect to the "host" lattice. Structurally, these domains are fragments of the YBCO lattice that are discontinued along the Cu(1)-O(1) plains. This picture implies that YBCO( $x \sim 0.6$ ) subjected to bromination becomes strongly heterogeneous on atomic length scales. Heterogeneity of brominated YBCO brings about unusual structural and electronic properties. We shall briefly discuss implications on conventional diffraction, magnetization, and transport measurements.

It is well established that diffraction peaks broadens significantly when bromine is introduced. The broadening, however, should not be directly associated with lattice distortions. In a two-phase model adopted in this paper, the distorted domains do not form any well-defined macroscopic phase. Therefore, they don't scatter elastically and don't give rise to additional diffraction peaks. As for the major phase (hosting the distorted domain inclusions) these inclusions deflect a lattice function in the reciprocal

space:  $L(r) = \sum_{n_1, n_2, n_3 = -\infty}^{\infty} \delta(r + n_1 a + n_2 b + n_3 c)$ . In heterogeneous compounds like Br-YBCO,

the sums run over other discrete domains of varying sizes,  $\Gamma$ , resulting in the  $\delta$ -functional

profiles to be substituted by Gaussian ones:  $L'(r, \Gamma) = \sum_{n_1, n_2, n_3 \in \Gamma} \delta(r + n_1 a + n_2 b + n_3 c)$ . The

DW factors extracted from a Rietveld refinement will overestimate lattice distortions in the major phase. The weight of the major phase scattering elastically will depend on the coherence length of an x-ray source and does not necessarily coincide with the XAFS estimate ( $\sim 2/3$  of the pristine sample for  $x \sim 0.6$ ). At the same time, lattice parameters are expected to be less affected by the heterogeneity. Their variation is a reasonable measure of *average* changes in orthorhombicity, volume of unit cell, and oxygen content

associated with the major phase. Previous diffraction results found that bromination converts the lattice of underdoped YBCO from tetragonal to orthorhombic phase, with  $c$ -parameter reduced: both are signatures of the re-oxygenation.

Local structural inhomogeneity could account for the broad superconducting transition seen for the brominated sample. It's instructive to compare the fractional amount of the superconducting phases (Meissner fraction) in the brominated and re-oxygenated samples ( $x \sim 0.9-1$ ) if the same YBCO ( $x \sim 0.6$ ) is subjected to either the bromination or re-oxygenation. Since we do not have our own data on re-oxygenated crystals, the ZFC magnetization data on 1- $\mu\text{m}$  YBCO powder ( $x=0.6$ ) shown in Fig. 4 of Ref. [57] will be examined here. Considering a ratio of the residual magnetizations at 10 K, one can estimate that the Meissner fraction in the brominated ceramic is about 60-65% of that in the re-oxygenated powder. Recalling that  $\sim 1/3$  of brominated crystal is locally decomposed we speculate that the decomposed phase isn't superconducting. Discontinuous behavior of the structure and large local distortions are consistent with the observation [72] that the room temperature resistivity of brominated YBCO is  $\sim 35$  times that of normal YBCO with the same critical temperature.

Lastly, we would like to point out that the heterogeneity in Br\_YBCO ( $x \sim 0.6$ ) differs in its origin from that observed in many high temperature superconductors [73] at low temperatures. In the latter compounds, the nanoscale heterogeneity (or phase separation) is derived from a correlated behavior of the electronic system coupled with lattice degrees of freedom. Though Br\_YBCO contains oxygen-rich domains where the above mechanism could be involved, the major factor determining the inhomogeneity is

aperiodic and incommensurate arrangements of nano-fragments caused by the decomposition reaction.

### 6.3 Conclusions

We have reported on the Br *K*-, Cu *K*-, Ba *L*<sub>3</sub>- and Y *K*-edge XAFS measurements of brominated YBa<sub>2</sub>Cu<sub>3</sub>O<sub>6+x</sub> crystal (Br/Cu~1/30, *x*~0.6) showing a superconducting transitions at ~89 K. Br *K*-edge data reveal that Br does not enter substitutionally or interstitially into the *perfect* YBCO lattice. Nor does it creates a large amount of *amorphous* decomposition products. The major result of this paper is that the brominated sample becomes strongly heterogeneous on the atomic length scales.

The heterogeneity can be satisfactorily understood in terms of major and impurity phases. The major phases are well-ordered, undistorted, and re-oxygenated YBCO lattice hosting differently ordered and heavily distorted decomposed inclusions which accounts for about 1/3 of the sample. The decomposed inclusions comprised of nano-fragments (nano-domains) formed as a result of a truncation of the parent YBCO lattice predominantly along the Cu(1)-O(1) planes accompanied by the fragments rearrangement. Despite the discontinuous behavior there are still highly correlated atom pairs so that the local structure still can be expressed by cluster expansions: Y-O(2,3)<sub>8</sub>-Cu(2)<sub>8</sub>-..., Ba-O<sub>8</sub>-Cu(2)<sub>4</sub>Cu(1)<sub>2</sub>-... and Cu-O<sub>4</sub>-...with respect to Y, Ba and Cu sites. The typical size of the decomposed domains is unknown, but is expected to be no less than 7-8 Å. Impurity phases (~1% of the total weight of the sample) are due to Br entering the Cu(1) site of a YBCO *fragment*, forming Br-O(4)-Ba-Cu<sub>2</sub>(1)Cu(2)-... and Br-Cu-... nano-clusters.



An artificial inhomogeneity might partly account for the divergence in the accumulated experimental data [49,50,51,52,53,54,55,56,57] demonstrating that measured physical properties essentially depend on the probing length of the chosen experimental technique. The small size of decomposed and impurity domains prevent them from diffracting elastically. Their presence, however, is observable by local structure sensitive measurements. Taking advantage of polarization-dependent measurements in FY mode (Sect. 6.1.3.1) we have found that Br is incorporated into randomly ordered nano-clusters which have more complex structure than  $\text{BaBr}_2$  considered in Refs. [54] and [57]. It is worth mentioning that the Br-Ba interatomic distance in the Br-O(4)-Ba-Cu<sub>2</sub>(1)Cu(2)-... cluster is close to the average Br-Ba distance in powder  $\text{BaBr}_2$ . Besides, Ba is a first heavy element coupled with Br so that X-ray photoemission and Br NMR spectra are expected to be reminiscent, although not identical, to those of powder  $\text{BaBr}_2$ . Further theoretical calculations of XPS and NMR spectra of different Br-based nanoclusters will be needed to reconcile remaining differences among the local structural probes.

This present work shows very clearly that bromination of  $\text{YBa}_2\text{Cu}_3\text{O}_{6.6}$  crystal must not be considered as doping since Br atoms destroy the homogeneity of the sample. Br-based nanoclusters are located in the decomposed regions, Fig. 5.14, which are highly-resistive at room temperature [72] and apparently are not superconducting, Sect. 6.3. A direct doping of the  $\text{CuO}_2$  planes, therefore, is unlikely. In agreement with previous work [52,57], the recovery of superconductivity is attributed to an increase of the oxygen population at the O(1) positions of the well-ordered crystalline phase that is evidenced by: (i) the behavior of Cu(1)-O(4) and Cu(2)-O(4) interatomic distances and

corresponding DW factors and by (ii) nature of the changes in polarized Cu *K*-edge XANES (Sect. 6.1.3.3).

#### **6.4 X-ray Absorption Fine Structure of Iodinated YBCO( $x \sim 0.27$ ) Single Crystals, Experimental Procedure and Data Reduction**

Nemudry *et al.*, [74,49(b)] reported a transition from tetragonal to orthorhombic after treating an insulating YBCO to iodine, see Section on brominated YBCO single crystals for additional information on halogenated YBCO materials. They found a partial destruction of the host lattice by a formation on the surface of copper oxides, yttrium oxides, barium iodides and copper iodides. As we proceeded for the brominated YBCO<sub>6+x</sub> ( $x \sim 0.6$ ) in (Section 6.1.3.1), we also investigated the location of the iodine atoms in iodinated YBCO<sub>6+x</sub> ( $x \sim 0.3$ ) single crystals at the I *L*<sub>3</sub>-edge.

##### **A Preparation of YBCO Single Crystals**

Single crystals of YBCO<sub>6+x</sub> ( $x \sim 0.27$ ) were prepared for the experiments as in Section 6.1.2 for the brominated YBCO single crystal (Fig. 6.1).

##### **B Iodination of YBCO<sub>6+x</sub> ( $x \sim 0.27$ ) single-crystal.**

Iodination of YBCO<sub>6+x</sub> ( $x \sim 0.27$ ) single crystals was performed by inserting a quartz rod inside a tube furnace which was heated up to 450°C. While the tube furnace was at 450°C, the quartz rod was left inserted inside for about two hours to assure equilibrium in temperature. It is important to mention that the iodination experiment performed at 450°C was set up similar to the bromination case see Section 6.1.2, B.

A pair of single crystals from the same batch (with the same oxygen content) was used in these experiments, but only one in a quartz boat out of the two was inserted inside the

A pair of single crystals from the same batch (with the same oxygen content) was used in these experiments, but only one in a quartz boat out of the two was inserted inside the quartz rod in an argonne atmosphere at 450°C. Finally, the single crystal  $\text{YBCO}_{6+x}$  ( $x \sim 0.27$ ) was treated under  $\text{CHI}_3$  vapor in argonne atmosphere at 450°C for four hours.

We performed x-ray diffraction measurements at NJIT using the Rigaku X-ray diffractometer. The results of the diffraction patterns showed no evidence for secondary crystallographic phases as in the brominated YBCO single crystals. Therefore, we speculate the iodine atoms to be at the impurity level in the iodinated sample.

X-ray Absorption Fine Structure (XAFS) data were collected at the National Synchrotron Light Source beamline X-19A (I  $L_3$  edge, Si (111) monochromator) in fluorescence mode at room temperature using the PIPS detector. At the iodine  $L_3$ -edge, we collected from two to six scans in order to improve the signal to noise ratios.

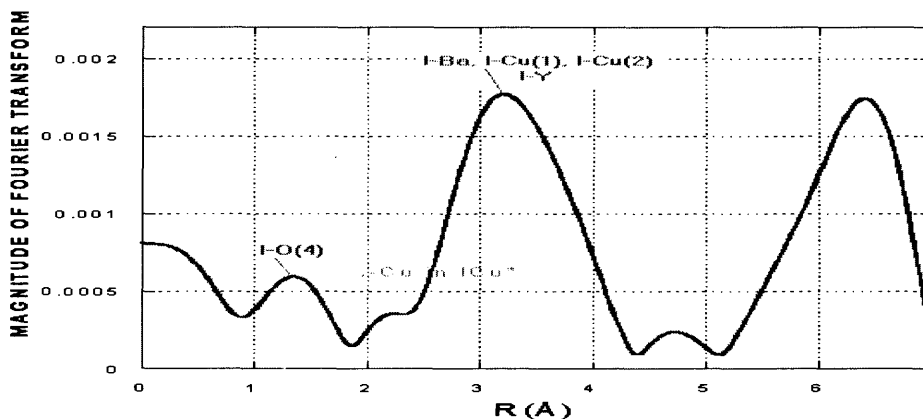


**Figure 6.14** Fourier transform of  $k^2\chi(k)$  in  $r$ -space for the iodinated  $\text{YBCO}(x \sim 0.27)$  single crystal at the I  $L_3$ -edge. Notice the first peak between 1-1.9 Å in the Fourier transform corresponds to the I-O(4).

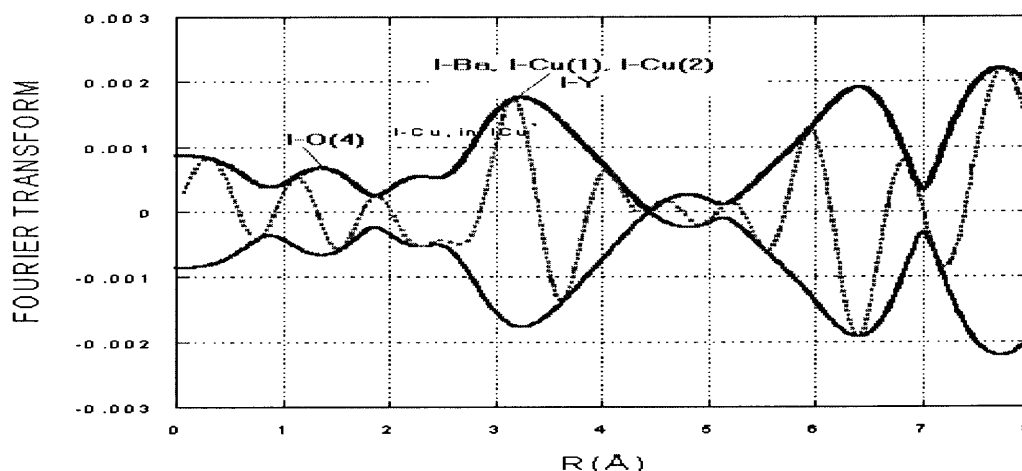


**Figure 6.15** The Fourier transform (FT) of iodinated YBCO at the I  $L_3$ -edge. The oscillating curve (dashed line) is the imaginary part of the FT. The envelope (solid curve) is the magnitude of the FT. The data are transformed with a square window between 3.75-8.66  $\text{\AA}^{-1}$ .

### 6.5 Experimental Results and Data Analysis for Iodinated YBCO( $x \sim 0.27$ ) Single Crystals, I $L_3$ -edge of the Iodinated YBCO Single Crystal

X-ray Absorption Fine Structure (XAFS) measurements at the I  $L_3$ -edge were performed in order to probe the location of the iodine atoms in the iodinated YBCO $_{6+x}$  ( $x \sim 0.27$ ) single crystal.

The I  $L_3$ -edge spectrum shown in were Fourier transformed to  $r$ -space over the range 3.75 - 8.66  $\text{\AA}$  using a square window. The resulting magnitude and imaginary parts are plotted in Fig. 6.14. The complex structure of the I  $L_3$ -edge analysis comes from the fact neither the chemical composition nor the local structure about the I atoms are known a priori. In an attempt to refine the structure as in the bromination case, we will proceed in several steps narrowing the choice of structural models and finally discussing the uniqueness of the fit. The first peak at  $\sim 1.80 \text{\AA}$  in Fig. 6.15 in the Fourier transform corresponds to the oxygen atoms. The best fit reveals the I-O interatomic distance  $R = 1.808 \text{\AA}$ , Debye-

the fit. The first peak at  $\sim 1.80 \text{ \AA}$  in Fig. 6.15 in the Fourier transform corresponds to the oxygen atoms. The best fit reveals the I-O interatomic distance  $R= 1.808 \text{ \AA}$ , Debye-Waller factor  $\sigma^{(2)}= 0.00089 \text{ \AA}^2$  and coordination number  $N= 0.147 \pm 0.002$ . Note that the extracted I-O interatomic distance coincides with Br-O(4) interatomic distance in Br\_YBCO and with Cu(1)-O(4) distance in YBCO. This also prompted the hypothesis that I enters the Cu(1) site of the oxygen deficient YBCO<sub>6+x</sub>(x~0). Next, we extended the number of peaks to be fitted in the Fourier transform Fig. 6.15. The I-O(4), I-Ba, I-Cu(1), I-Cu(2) peaks were fit in the single scattering approximation [65] as for the brominated YBCO<sub>6+x</sub> (x~0.6) (Section 6.1.3.1). We constrained all the coordination numbers in order to determine the shape of the clusters about the iodine atoms. For instance, if iodine is in the Cu(1) site of the oxygen deficient YBCO lattice it has to be two fold coordinated O(4), eightfold coordinated to Ba, fourfold coordinated to Cu(1) and two fold coordinated to Cu(2). We found that the experimental data are better fit with less than one O(4), with one Ba, Cu(2) and with about 2 Cu(1) atoms about the I in the Cu(1) site. This set of coordination numbers implies that clusters are randomly oriented with respect to the polarization vector **E** and therefore are randomly oriented with respect to the host crystalline structure. The coordination number for ICu\* is found to be about 1, the results are summarized in Table 6.5. Lower coordination numbers found about the I atom indicate that *I does not enter the Cu(1) site in the perfect YBCO lattice*. However, good agreement between all four I-X [X=O(4), Ba, Cu(1), Cu(2)] interatomic distances obtained from our fit suggests that iodine occupies the Cu(1) site in I-O<sub>0.14</sub>(4)-Ba-Cu<sub>1.9</sub>(1)-Cu<sub>1</sub>(0)-....nanoclusters (nanofragments) which yet retain the 3D structure of the original YBCO lattice. The extracted coordination numbers suggest that the nanoclusters

are randomly oriented in the iodinated YBCO ( $x \sim 0.27$ ) single crystal. We have compared our XAFS results at the I  $L_3$ -edge on the iodinated YBCO with those XAFS results at the Br- $K$ -edge of the brominated YBCO Table 6.6. We conclude that iodine occupies the Cu(1) site in nanofragments of the YBCO lattice which is in agreement with our work on brominated single crystal samples see Section 6.1.3.1 [75].

## 6.6 Conclusions

We have performed XAFS measurements on I-YBCO $_{6+x}$  ( $x \sim 0.27$ ) at the I  $L_3$ -edge. Our XAFS measurements at I  $L_3$ -edge on I-YBCO reveal that I does not enter substitutionally or interstitially into the perfect YBCO lattice, but I occupies the Cu(1) site in nanofragments of the YBCO lattice. From our XAFS results at the I  $L_3$ -edge, it shows clearly that iodination can not be taken as doping since iodine atoms destroy the homogeneity of the sample. We believe that iodine based nanoclusters are located in the decomposed phase as in brominated YBCO single crystals. In order to confirm this hypothesis, XAFS measurements at the Cu  $K$ -edge need to be analyzed for I-YBCO $_{6+x}$  ( $x \sim 0.27$ ) single crystals.

**Table 6.5** I  $L_3$ -edge XAFS data for I-YBCO. The local structural parameters are obtained by using the structural parameters at Br  $K$ -edge for Br-YBCO.  $S_0^2$  was estimated to be 0.82. Errors in the extracted parameters were estimated from the covariance matrix generated from the fit and should be considered as relative errors.

I $L_3$ -edge XAFS for I-YBCO $_{6+x}$ ( $x \sim 0.27$ )			
Bond	R(Å)	No. of neighbors	$\sigma^{(2)} \times 10^{-3} (\text{Å}^2)$
I-O(4)	$1.80 \pm 0.02$	$0.147 \pm 0.002$	1
I-Ba	$3.507^*$	$1.0^*$	14
I-Cu(1)	$3.71^*$	1.9	3
I-Cu(2)	$4.16^*$	1.0	26
I-Cu in (ICu $^*$ )	$2.49^*$	0.8	51

**Table 6.6** Comparison of I-YBCO with Br-YBCO XAFS data. The XAFS data for Br YBCO were taken from Table 6.1.

COMPARISON OF I $L_3$ -edge for I-YBCO <sub>6.27</sub> WITH Br K-edge FOR Br-YBCO <sub>6.6</sub>					
I-YBCO <sub>6.27</sub> XAFS				Br-YBCO <sub>6.6</sub> XAFS	
Bond	R(Å)	No. of neighbors	$\sigma^{(2)} \times 10^{-3} (\text{Å}^2)$	Bond	R(Å)
I-O(4)	1.80 ± 0.02	0.147 ± 0.002	1	Br-O(4)	1.84
I-Ba	3.507*	1.0*	14	Br-Ba	3.51
I-Cu(1)	3.71*	1.9	3	Br-Cu(1)	3.89
I-Cu(2)	4.16*	1.0	26	Br-Cu(2)	4.16
I-Cu in (ICu*)	2.49*	0.8	51	Br-Cu in (BrCu*)	2.45

## CHAPTER 7

### SUMMARY AND PROPOSED FUTURE WORK

#### 7.1 Summary of the Background of Superconductivity and of Copper Oxide Based Superconductors

Superconductivity was found for the first time at 4 Kelvin in mercury, in 1911 by dutch physicist Heike Kamerlingh Onnes of Leiden University. When he cooled mercury to the temperature of liquid helium which is 4 K (Kelvin), its resistance suddenly disappeared. It was necessary for Onnes to come up with 4 degrees of the coldest temperature that is theoretically attainable to witness the phenomenon of superconductivity.

Few decades later, in 1933 Walter Meissner and Robert Ochsenfeld discovered that a superconducting material will repel a magnetic field. This phenomenon is called Meissner Effect. They found that the expected situation did not in fact occur, but that at their transition temperatures the specimens spontaneously became perfectly diamagnetic, canceling all flux inside, even though they had been cooled in a magnetic field. This experiment was the first one to demonstrate that superconductors are something more than materials which are perfectly conducting, they have an additional property that a merely resistanceless metal would not possess: a metal in the superconducting state never allows a magnetic flux density to exist in its interior. That is to say, inside a superconducting metal we always have  $B=0$ , whereas inside a merely resistanceless metal there may or may not be a flux density, depending on circumstances. When a superconductor is cooled in a weak magnetic field, at the transition temperature persistent currents arise on the surface and circulate so as to cancel the flux density inside, in just the same way as when a magnetic field is applied after the metal has been cooled. This



effect, whereby a superconductor never has a flux density inside even when in an applied magnetic field, is called the *Meissner effect*.

In 1935, Fritz London pointed out that superconductivity is a quantum phenomenon in a macroscopic scale with the lowest energy state separated by a finite interval from the excited states called energy gap and diamagnetism is its fundamental property see. It is also important to mention that, An essential clue came in 1950 when researchers at the National Bureau of Standard and Rutgers University, discovered that the superconducting transition of lead depended on its isotopic mass  $M$ . They showed that, the product of the nuclear mass with the transition temperature is a constant, where the exponent  $\alpha$  of the nuclear mass is about 0.5, for Pb  $\alpha=0.485$ .

In the next few decades few superconducting metals and alloys were discovered, in 1941,1953 Niobium-Nitride and Vanadium-Silicon displayed superconductive properties at 16 K and 17.5 K respectively.

It was only in 1957 when physicists John Bardeen, Leon Cooper, and John Schrieffer (BCS theory), advanced their theory of superconductivity which was widely accepted by the scientific community. The BCS theory explained superconductivity at temperature close to zero for elements and simple alloys.

Superconductors can be divided in two types, type I and type II superconductors. Type I superconductors, is mainly comprised of pure metals and type II superconductors is also comprised of metallic compounds and alloys except for the elements vanadium, technetium and niobium.

The discovery of superconductivity above 10 K in NbC and NbN was a breakthrough. Later on, the A15 compounds with  $T_C$  found up to 20 K in the late 1960s and earlier

1970s, was the result of hard work for almost more than two decades in the search of high temperature superconductors (HTSC).

In the search of HTSC, Bednorz and Muller discovered a  $T_C$  higher than in A15 compounds in the copper oxide based system, they found a transition occurring to the superconducting state in the La-Ba-Cu-O system near 30 K. They established that the  $T_C$  is in the range between 20-40 K for  $La_{2-x}M_xCuO_{4-y}$  with  $M = Ba, Sr, Ca$  and when pressure is applied, the coefficient of temperature is larger and drives the  $T_C$  above 50 K in the  $M = Sr$  based system. In 1987, Wu. *et al.*, [3] found a  $T_C$  above 90 K for the  $YBaCuO_{7-y}$  (123 or YBCO) compound, placing it among the first of the copper oxide compounds to exhibit superconductivity above the temperature of liquid nitrogen (77 K). In this thesis, we will investigate XAFS measurement on halogenated and non halogenated YBCO single crystals to probe the locations of the halogens and to investigate structural distortions about each given element. Michel *et al.*, [4] reported a transition temperature in Bi-Sr-Cu-O (BSCO) with  $T_C = 20$  K, their result led to the discovery of bulk superconductivity at 85 K and an evidence for superconductivity at 110 K in the Bi-Sr-Ca-Cu-O Maeda *et al.*, [5]. Hazen *et al.*, [7] found the Tl-Ba-Cu compound to be a high temperature superconductor, when doped with Ca the  $T_C$  increased up to 100K. The common feature of all copper-oxide based superconductors is that, they all have layers of copper-oxide sheets which are believed to play a very important role in the occurrence of high temperature superconductivity.

In contrast to the Cu-O based superconductors, superconductivity was found in  $Ba_{1-x}K_xBiO_3$  (Ba-K-Bi-O) compound at 30 K, which led several scientists to conclude that the mechanism responsible for superconductivity is still not well understood. Since

few groups have reported to have found the Cu(2)O planes to be responsible for the occurrence of high temperature superconductivity see Chapter 2 for more detailed description of HTSC.

## **7.2 Summary of Doping and Structural Disorder in the YBCO Compound**

Oxygen annealing of insulating YBCO samples have been done in two ways, the first one is annealing under ambient pressure and the second one is high pressure annealing. Noting that high pressure annealing (HPA) has been found to affect the transition temperature than ambient pressure annealing.

Substitutions of 3d elements on the Cu ion site of the YBCO, have been performed, since their ionic and orbital structure are close to those of Cu. No element has been found for doping on the Cu site that either keeps the orthorhombic symmetry or enhances the transition temperature in YBCO (123) compound. This is also true in the case of doping into the Ba site. Several groups have reported replacing Y site with rare earth elements. They showed that only Pr and La were not superconducting when replaced at the Y site, all other rare earth elements did show superconductivity behavior see Chapter 3. Photodoping of YBCO thin film samples with low oxygen by illumination, is found to increase the concentration of carriers (free holes) which leads to similar effects in transport and magnetic properties as would result from increasing the oxygen content of the material.

### 7.3 Summary of Pressure and of Defect Effects on Superconductivity

Pressure measurements have been performed on both type I and type II superconductors. Ishizuka *et al.*, [26] reported the pressure dependence of the transition temperature ( $T_C$ ) of vanadium up to 120 GPa, from their results they found a linear dependence of  $T_C$  as a function of applied pressure. The  $T_C$  of vanadium increased significantly as pressure was increased (Fig. 2, ref. 26). Anomalies in  $T_C$  were observed in niobium, between 5-6 GPa and 60-70 GPa the  $T_C$  increases by 0.7 K in agreement with [26] and decreases by 1 K respectively [27].

Soon after the discovery of superconductivity in the type II YBCO system, pressure measurements were achieved using He gas as pressure medium up to 8 Kbar by [28]. They found the  $T_C$  to change as pressure was increased [26, 27]. Another superconducting material  $\text{La}_{2-x}\text{Sr}_x\text{CuO}_4$  (LSCO) system was studied under pressure. It is known that in the LSCO system, superconductivity, takes place mainly in the orthorhombic phase. Also pressure dependence of  $T_C$  was performed on the newly discovered  $\text{MgB}_2$  superconductor [30], in contrast to [26, 27, 28, 29] they obtained the  $T_C$  to decrease significantly for zero-resistance under pressure up to 1.35 GPa [31].

Experiments have shown on superconducting YBCO thin films, that the transition temperature of these films decreased significantly when their thicknesses were reduced below 100 Å. Such an experiment was introduced by Li *et al.*, [32], they studied a superconducting YBCO thin film deposited on a PrYBCO substrate. They claimed the reason why they have used the PrYBCO as a substrate is that, it has an orthorhombic structure with lattice parameters close to the YBCO system; providing a much better

lattice match than any other substrate to YBCO and also because it is a non superconductor with a very high resistivity at low temperatures.

In plane pressure effect in strained YBCO<sub>7</sub>/La<sub>1.85</sub>Sr<sub>0.15</sub>CuO<sub>4</sub> superlattices on MgO (100) substrate was investigated by Horiuchi *et. al.*, [34], they stacked layers of thin film YBCO on top of the LSCO layers then deposited them on the MgO (100) substrate.

In agreement with [32, 33], they found the crystal structure to change when the layers of the YBCO thin films were varied while the LSCO layers were fixed.

#### **7.4 Summary of Brominated (non-brominated) and Iodinated (non-iodinated) YBCO Single Crystals Using XAFS Spectroscopy**

The XAFS measurements at bromine *K*-edge of the brominated YBCO (Br-YBCO) revealed significantly lower coordination numbers about the bromine atom which unambiguously indicated that *Br does not enter the Cu(1) site in the perfect YBCO lattice*. However, from our extracted interatomic distances from the EXAFS we found good agreement between all four Br-X [X= O(4), Ba, Cu(1), Cu(2), Y] interatomic distances with the ones of the oxygen deficient YBCO. From the lowering of the coordination numbers about the bromine atom in the Br-YBCO, we speculate that *Br occupies the Cu(1) site in Br-O(4)-Ba-Cu<sub>2</sub>(1)Cu(2)-... nano-clusters (nano-fragments)* which yet retain the 3D structure of the original YBCO lattice. Coordination numbers extracted suggest that those nano-clusters are randomly oriented in the brominated crystal. An independent confirmation of this fact came from the absence of polarization dependence performed at two different geometries 45° and 90° for the X-ray Absorption Near Edge Structure (XANES).

Similar to the Br-YBCO, lower coordination numbers were found about the iodine atom as well, which indicates that *I does not enter the Cu(1) site in the perfect YBCO lattice*. However, good agreement between all four I-X [X=O(4), Ba, Cu(1), Cu(2)] interatomic distances the Br-X [X=O(4), Ba, Cu(1), Cu(2)] interatomic distances obtained from our fits suggests that iodine occupies the Cu(1) site in I-O<sub>0.14</sub>(4)-Ba-Cu<sub>1.9</sub>(1)-Cu<sub>1</sub>(0)-...nanoclusters (nanofragments) which yet retain the 3D structure of the original YBCO lattice. The extracted coordination numbers suggest that those nanoclusters are randomly oriented in the iodinated YBCO( $\gamma \sim 0.27$ ) single crystal. We have compared our XAFS results at the Br *K* on the Br-YBCO and at I *L*<sub>3</sub> edges we found similar effects of both halogens on YBCO single crystals.

### 7.5 Future Work

We have performed a complete and detailed XAFS analysis on the brominated (Br-YBCO) and non-brominated (YBCO) single crystals. We also studied using XAFS techniques iodinated (I-YBCO) and non-iodinated (YBCO) single crystals. A systematic XAFS analysis were done at the I *L*<sub>3</sub>-edge on the I-YBCO single crystals looking for the location of the iodine atoms in the system.

I. We are currently working on the c-axis polarized XAFS measurements on both I-YBCO (iodinated) and YBCO (non-iodinated) single crystals with a goal to find phase decompositions that might have taken place during iodination. But our c-axis polarized XAFS data at the Cu *K*-edge on both I-YBCO and YBCO need to be analyzed and is not included in this thesis work

II. We have also chlorinated YBCO (Cl-YBCO) single crystals and did XAFS

measurements on them, further XAFS measurements at the chlorine *K*-edge on the chlorinated (Cl-YBCO) need to be done in order to complete the analysis.

**III.** Recently, we have made bulk LSCO powder samples and eventually we would like to make thin films from them and investigate their structural changes when deposited on different substrates (strain effect on the LSCO system).

**IV.** For further structural investigations in the near future, we will also analyze our high energy synchrotron x-ray diffraction and high energy XAFS measurements on the anti-perovskite  $\text{MgCNi}_3$ .

## REFERENCES

1. L. Solymar and D. Walsh, Lectures on the Electrical Properties of Materials, Clarendon Press, Oxford 1970, (a) H. Kamerlingh Onnes, Akad. Van Wafenschappen (Amsterdam) 8, 113, 818 (1911), (b) W. Meissner and R. Oschenfeld, Naturwissenschaften 21, 787 (1933).
2. Gerald D. Mahan, 2<sup>nd</sup> ed., Many Particle Physics 1990, 1981 Plenum Press, New York.
3. M. K. Wu, J. R. Ashburn, C. J. Torng, P.H. Hor, R. L. Meng, L. Gao, Z. J. Huang, Y. Q. Wang and C. J. Chu, Phys. Rev. B **58**, 908 (1987), (a) Z.Z. Sheng and A. M. Herman, Nature 332, 55 (1988), (b) R.M. Hazen, L.W. Finger, R.J. Angel, C.T. Drewitt, N.L. Ross, C.G. Hadidiacos, P.J. Heaney, D.R. Veblen, Z.Z. Sheng, A.El. Ali and A.M. Herman, Phys. Rev. Lett. 60, 1657 (1988), (c) S.S. Parkin, V.Y. Lee, E.M. Engler, A.I. Nazzal, T.C. Huang, G. Gorman, R. Savoy and R. Beyers. Phys. Rev. Lett. 60, 2539 (1988).
4. C. Michel, M. Hervieu, M. M. Borel, A. Grandin, F. Deslandes, J. Provost and B. Raveau, Z. Phys. B **68**, 421 (1987).
5. H. Maeda, Y. Tanaka, M. Fukutumi and T. Asano, Jpn. J. Appl. Phys. **27**, L 209
6. J. M. Tarascon, Y. LePage, L. H. Greene, B. G. Bagley, P. Barboux, D. M. Hwang, G. W. Hull, W. R. McKinnon and M. Giroud, Phys. Rev. B **38**, 2504 (1988).
7. R. M. Hazen, L. W. Finger, R. J. Angel, C. T. Prewitt, N. L. Ross, C. G. Hadidiacos, P. J. Heaney, D. R. Veblen, Z. Z. Sheng, A. El Ali and A. M. Herman, Phys. Rev. B **60**, 1657 (1988).
8. R. J. Cava, B. Batlogg, J. J. Krajewski, R. C. Farrow, L. W. Rupp Jr., A. E. White, K. T. Short, W. F. Peck Jr. and T. Y. Kometani, Nature **332**, 814 (1998), (a) R. Cava and M. Hazen, Scientific American, June (1988).
9. D. G. Hinks, B. Dabrowski, J. D. Jorgensen, A. W. Mitchell, D. R. Richards, Shiyong Pei and Donglu Shi, Nature **333**, 836 (1988).
10. J. D. Jorgensen, B. W. Veal, A. P. Paulikas, L. J. Nowicki, G. W. Crabtree, H. Claus and W. K. Kwok, Phys. Rev. B **41**, 1863 (1990).
11. W. Shafer, E. Jansen, G. Will, J. Faber Jr. and B. Veal, Mat. Res. Bull., vol. 23, 1439-1445 (1988).
12. R. L. Neiman, J. Giapintzakis and D. M. Ginsberg, Phys. Rev. B **50**, 16028 (1994)




## REFERENCES

(continued)

13. Gang Xiao, F. H. Streitz, A. Garvin, Y. W. Du and C. L. Chien, *Phys. Rev. B* **35**, (1987).
14. T. Siegrist, L. F. Shneemeyer, J. V. Waszczak, N. P. Singh, R. L. Opila, B. Batlogg, L. W. Rupp and D. W. Murphy, *Phys. Rev. B* **36**, 8365 (1987).
15. J. M. Tarascon, W. R. McKinnon, L. H. Greene, G. W. Hull and E. M. Vogel, *Phys. Rev. B* **36**, 226 (1988).
16. A. Veneva, I. Iordanov, L. Toshev, A. Stoyanova-Ivanova and D. Gogova, *Physica C* **308**, 174-184 (1998).
17. H. A. Blackstead, John D. Dow, D. B. Chrisey, J. S. Horwitz, M. A. Black, P. J. McGinn, A. E. Klunzinger and D. B. Pulling, *Phys. Rev. B* **54**, 6122 (1996)
18. Zhigang Zou, Kunihiro Oka, Toshimitsu Ito and Yoshikazu Nishihara, *Jpn. J. Appl. Phys.* **36**, L18-L20 (1997).
19. Toshiyuki Usagawa, Yoshihiro Ishimaru, Jianguo Wen, Tadashi Utagawa, Satoshi Koyama and Youichi Enomoto, *Jpn. J. Appl. Phys.* **36**, L1583-L1586 (1997) Pt2.
20. Zhigang Zou, Jinhua Ye, Kunihiro Oka, and Yoshikazu Nishihara, *Phys. Rev. Lett.* **80**, 1074 (1998).
21. V. I. Kudinov, I. L. Chaplygin, A. I. Kirilyuk, N. M. Kreines, R. Laiho, E. Lahderanta and C. Ayache, *Phys. Rev. B* **47**, 9017 (1992).
22. E. Osquigil, M. Maenhoudt, B. Wuyts, Y. Brynseraede, D. Lederman and Ivan. K. Schuller, *Phys. Rev. B* **49**, 3675 (1994).
23. K. Kawamoto and I. Hirabayashi, *Phys. Rev. B* **49**, 3655 (1994).
24. T. A. Tyson, J. F. Federici, D. Chew, A. R. Bishop, L. Furenlid, W. Savin and W. Wilber, *Physica C* **292**, 163-170 (1997).
25. K. Widder, J. Munzel, M. Goppert, D. Luerben, R. Becker, A. Dinger, H. P. Geserich, C. Klingshirn, M. Klasner, G. Muller-Vogt, J. Geerk and V. M. Burlakov, *Physica C* **300**, 115-124 (1998), a). J.F. Federici and D.M. Bubb, *J. Superconductivity* **14**, 331(2001).
26. M. Ishizuka, M. Iketani and S. Endo, *Phys. Rev. B* **61**, R3823 (2000).

**REFERENCES**  
**(continued)**

27. Victor V. Struzhkin, Yuri A. Timofeev, Russell J. Hemley and Ho-Kwang Mao, *Phys. Rev. Lett.* **79**, 4262 (1997).
28. J. E. Schirber, D. S. Ginley, E. L. Venturini and B. Morosin, *Phys. Rev. B* **35**, 8709 (1987).
29. Toshizo Fujita, Jun'ya Hori, Tatsuo Goko, Naoki kikugawa and Shingo Iwata, *Riken Review* **27**, 75 (2000).
30. Nagamatsu J, Nakagawa N, Muranaka T, Zenitani Y and Akimitsu J, *Nature* **410**, 63 (2001).
31. E. Saito, T. Taknenobou, T. Ito, Y. Iwasa, K. Prassides and T. Arima, *J. Physics* **13**, L267-L270 (2001).
32. Q. Li, X. X. Xi, X. D. Wu, A. Inam, S. Vadlamanati, W. McLean, T. Venkatesan, R. Ramesh, D. M. Hwang, J. A. Martinez and L. Nazar, *Phys. Rev. Lett.* **64**, 3086 (1990).
33. Douglas H. Lowndes, David P. Norton and J. D. Budai, *Phys. Rev. Lett.* **65**, 1160 (1990).
34. Ken Horiuchi, Masaki Kanai, Tomoji Kawai and Schichio Kawai, *Phys. Rev. B*, **45**, 13152 (1992).
35. Reynolds, Serin, Wright and Nesbit, *Phys. Rev.* **78**, 487 (1950).
36. H. Frohlich, *Phys. Rev.* **79**, 845 (1950).
37. N. L. Cooper, *Phys. Rev.* **104**, 1189 (1956).
38. J. Bardeen, L. N. Cooper and J. R. Schrieffer, *Phys. Rev.* **108**, 1175 (1957).
39. R. Balian and N. R. Werthamer, *Phys. Rev.* **131**, 1553 (1963).
40. J. R. Schrieffer, X. G. Wen and S.-C. Zhang, *Phys. Rev. Lett.* **60**, 944 (1988).
41. J. R. Schrieffer, X. G. Wen and S. C. Zhang. *Phys. Rev. B*, **39** 11663 (1989), (a) 
42. Felix Yndurain, *Solid State Communications*, Vol. **81**, 939-942 (1992).
43. Felix Yndurain, *Phys. Rev. B* **51**, 8494 (1995).

**REFERENCES**  
(continued)

44. A. S. Alexandrov and P. E. Kornilovitch, “Frohlich-Coulomb model of high temperature superconductivity and charge segregation in the cuprates”, <http://xxx.lanl.gov/cond-mat/0203291>.
45. D. E. Sayers, F.W. Lytle and E.A. Stern 1970, *Advances in X-ray analysis* vol 13, ed. B.L. Hence, J.B. Newkirk and G.R. Malett (New York Plenum) p. 248.
46. Sayers D. E, Stern E. A and Lytle F. W, 1971 *Phys. Rev. Lett.* **27**, 1204.
47. G.G. Li, F. Bridges and C.H. Booth, *Phys. Rev. B* **52**, 6332 (1995).
48. Luciano Fonda, *J. Phys : Condens. Matter* **4**, 8269 (1992), D.E. Stern and D.E. Sayers, *Phys. Rev. B* **11**, 4836 (1975).
49. (a) Yu. A. Ossipyan, O. V. Zharikov, N. S. Sidorov, V. I. Kulakov, D. N. Mogilyanskii, R. K. Nikoloev, V. Sh. Shekhtman, O. A. Volegova and I. M. Romanenko, *Pis'ma Zh. Eksp. Teor. Fiz.* **48**, 225 (1988) [*JETP Lett.* **48**, 246 (1988)]; (b) Yu. A. Ossipyan, O. V. Zharikov, *Physica C* **162-164**, 79 (1989).
50. H. B. Radousky, R. S. Glass, P. A. Hahn, M. J. Fluss, R. G. Meisenheimer, B.P. Bonner, C. I. Mertzbacher, E. M. Larson, K. D. McKeegan, J.C. O'Brien, J.L. Peng, R.N. Shelton and K.F. McCarty, *Phys. Rev B.* **41**, 11140 (1990).
51. M. Mokhtari, C. Perrin, M. Sergent, E. Furet, J. F. Halet, J. Y. Saillard, E. Ressouche, and P. Burlet, *Solid State Commun.* **93**, 487 (1995).
52. Yu. A. Ossipyan, O. V. Zharikov, V. L. Matukhin and V. N. Anashkin, *Z. Naturforsch. Teil A* **47**, 21 (1992); M. Mokhtari, O. Peña, A. Perrin, and M. Sergent, *Mater. Lett.* **13**, 241 (1992); D. M. Potrepka, M. Balasubramanian, D. B. Fenner, W. A. Hines, and J. I. Budnick, *Appl. Phys. Lett.* **73**, 1137 (1998).
53. All atomic sites are labeled following by J. D. Jorgensen, M. A. Beno, D. G. Hinks, L. Soderholm, K. J. Volin, R. L. Hitterman, J. D. Grace, I. K. Schuller, C. U. Segre, K. Zhang, and M. S. Kleefisch, *Phys. Rev. B* **36**, 3608 (1987).
54. Y. Fukuda, N. Sanada, Y. Suzuki, T. Goto, M. Nagoshi, Y. Syono and M. Tachiki, *Phys. Rev. B* **47**, 418 (1993).
55. M. Mokhtari, C. Perrin, M. Sergent, E. Furet, J. F. Halet, J. Y. Saillard, E. Ressouche, and P. Burlet, *Solid State Commun.* **93**, 487 (1995).

**REFERENCES**  
**(continued)**

56. A. P. Nemudry, Yu. T. Pavlyukhin, N. G. Khainovsky and V. V. Boldyrev, *Superconductivity* **3**, 1215 (1990). / In Russian Edition pages are: 1528-1534.
57. D. M. Potrepka, J. I. Budnick, D. B. Fenner, W. A. Hines, M. Balasubramanian, A. R. Moodenbaugh, *Phys. Rev. B* **60**, 10489 (1999).
58. T. M. Hayes and J. B. Boyce, in *Solid State Physics*, edited by H. Ehrenreich, F. Seitz, and D. Turnbull (Academic, New York, 1982), Vol. 37, p. 173.
59. L. Tröger, D. Arvanitis, K. Barberschke, H. Michaelis, U. Grimm and E. Zschech, *Phys. Rev. B* **46**, 3283 (1992).
60. [http://www-cxro.lbl.gov/optical\\_constants/pert\\_form.html](http://www-cxro.lbl.gov/optical_constants/pert_form.html)
61. E. A. Stern, *Phys. Rev. B* **48**, 9825 (1993).
62. S. I. Zabinsky, J. J. Rehr, A. Ankudinov, R. C. Albers, and M. J. Eller, *Phys. Rev. B* **52**, 2995 (1995).
63. H. Casalta, P. Schleger, P. Harris, B. Lebech, N.H. Andersen, Ruixing Liang, P. Dosanjh and W.N. Hardy, *Physica C* **258**, 321 (1996).
64. S. A. Hodorowicz, E. K. Hodorowicz, and H. A. Eick, *J. of Solid State Chem.* **48**, 351 (1983).
65. Note, that at this point of refinement, the number of fitting parameters does not allow inclusion even a few multiple scattering paths. Besides, as will be apparent from further analysis, the local structure about Br is strongly distorted, reducing the effects of multiple scattering.
66. C. H. Booth, F. Bridges, J. B. Boyce, T. Claeson, B. M. Lairson, R. Liang, and D. A. Bonn, *Phys. Rev. B* **54**, 9542 (1996).
67. J. Mustre de Leon, S. D. Conradson, I. Batistic, A. R. Bishop, I. D. Raistrick, M. C. Aronson and F. H. Garzon, *Phys. Rev. B* **45**, 2447 (1992); E. A. Stern, M. Qian, Y. Yacoby, S. M. Heald and H. Maeda, *Physica C* **209**, 331 (1993).
68. J. D. Sullivan, P. Bordet, M. Marezio, K. Takenaka and S. Uchida, *Phys. Rev. B* **48**, 10638 (1993).
69. J. M. Tranquada, S. M. Heald, A. R. Moodenbaugh, and Y. Xu, *Phys. Rev. B* **38**, 8893 (1988).

## REFERENCES

(continued)

70. S. M. Mukhopadhyay, R. Garcia, and N. Mahadev, *Physica C* **313**, 205 (1999).
71. M. Mokhtari, C. Perrin, O. Pena, A. Perrin and M. Sergent, *Mater. Lett.* **13**, 241-253 (1992).
72. P.P. Nguyen, Z. H. Wang, A.M. Rao, M.S. Dresselhaus, J.S. Moodera, G. Dresselhaus, H.B. Radousky, R.S. Glass, J. Z. Liu. *Phys. Rev. B* **48**, 1148 (1993).
73. See, for example, T. Egami and S. J. L. Billinge in *Physical Properties of High Temperature Superconductors*, edited by D.M. Ginsberg, (World Scientific, Singapore, 1997), Vol. 5
74. A.P. Nemudry, I.I. Gainutdinov, Yu.T. Palyukhin and V.V. Bodyrev, *Physica C* **211**, 375-379 (1993).
75. L. M. Dieng, A. Yu. Ignatov, T. A. Tyson, M. Croft, F. Dogan, C.-Y. Kim, J. C. Woicik and J. Grow, *Phys. Rev. B* **66**, 014508 (2002).
76. W. Schafer, E. Jansen, G. Will, J. Faber, Jr and B. Veal, *Mat. Res. Bull.* **23**, 1439-1445 (1988).
77. P. Shweiss, W. Reichardt, M. Braden, G. Collin, G. Heger, H. Clauss and A. Erb, *Phys. Rev. B* **49**
78. Winnie Wong-Ng, Frank. W. Gayle, Debra L. Kaiser, Steven F. Waltkins and Frank R. Fronczek, *Phys. Rev. B* **41**, 4220 (1990).
79. H. Casalta, P. Schleger, P. Harris, B. Lebech, N.H. Andersen, Ruixing Liang, P. Donsanjh and W. N. Hardy, *Physica C* **258**, 321-330 (1996).
80. J.D. Jorgensen, B.W. Veal, A.P. Paulikas, L.J. Nowicki, G.W. Crabtree, H. Clauss and W.K. Kwok, *Phys. Rev. B* **41**, 1863 (1990).
81. Ke Zhang, G.B. Bunker, G. Zhang, Z.X. Zhao, L.Q. Chen and Y.Z. Huang, *Phys. Rev. B* **37**, 3375 (1988).
82. E.D. Crozier, N. Alberding, K. B. Bauchspiers, A.J. Seary and S. Gyax, *Phys. Rev. B* **36**, 8288 (1987).
83. C.Y. Yang, S.M. Heald, J.M. Tranquada, A.R. Moodenbaugh and Youwen Xu, *Phys. Rev. B* **38**, 6568 (1988).

**REFERENCES**  
**(continued)**

84. J. Mustre de Leon, S.D. Conradson, I. Batistic and R. Bishop, *Phys. Rev. B* **65**, 1675 (1990).
85. P. Sharma, L.E. Rehn, P.M. Baldo and J.Z. Liu, *Phys. Rev. Lett.* **62**, 2869 (1989).
86. L. Gensel, A. Wittlin, M. Bauer, M. Cardona, E. Schonherr and A. Simon, *Phys. Rev. B* **40**, 2170 (1989).
87. J. Mustre de Leon, S.D. Conradson, I. Batistic, A.R. Bishop, I.D. Raistrick, M.C. Aronson and F.H. Garzon, *Phys. Rev. B* **45**, 2447 (1992).
88. C. H. Booth, F. Bridges, J.B. Boyce, T. Cleason, Z. X. Zhao and P. Cervantes, *Phys. Rev. B* **49**, 3432 (1994).
89. C. H. Booth, F. Bridges, J. B. Boyce, T. Cleason, B.M. lairson, R. Liang and D. Bonn, *Phys. Rev. B*, **54**, 9542 (1996).
90. J. H. Han, C. X. Go, and P.K. Lim, *Solid State Communications* **91**, 901-905 (1994).
91. Zhongzua Wu and Francois Farges, *Physica B*, **266** 282-289 (1999).
92. Warren E. Pickett, "Electronic Structure of the High Temperature Oxide Superconductors", *Rev. Mod. Phys.* **61**, 433 (1989).
93. S.W. Tozer, A.W. Kleisasser, T. Penny, D. Kaiser and F. Hotzberg, *Phys. Rev. Lett.* **59**, 1768 (1987).
94. Howard A. Blackstead and John D. Dow, *Phys. Rev. B* **51**, 11830 (1995).
95. R. Cava, *Scientific American*, June (1990).
96. M.A. Beno, L. Soderholm, D.W. Capone, D.G. Hinks, J.D. Jorgensen, J.D. Grace, Ivan. K. Schuller, C.U. Segre and K. Zhang, *Appl. Phys. Lett.* **51**, 57 (1987).
97. P.A. Lee and G. Beni, *Phys. Rev. B*, **15**, 2862 (1976).
98. J.J. Rehr, R.C. Albers and S.I Zabinsky, *Phys. Rev. B* **69**, 3397 (1992), (a) J.J. Rehr and R.C. Albers, *Phys. Rev. B* **41**, 8139 (1990).
99. X-ray Absorption, D.C. Koningsberger and R. Prins, eds; Willey (1988).

**REFERENCES**  
**(continued)**

100. M. Newville, P. Livins, Y. Yacoby, J.J. Rehr and E.A. Stern, Phys. Rev. B **47**, 14126 (1993).
101. J.W. Cook and D.E. Sayers, J. Appl. Phys. **52**, 5024 (1981).
102. B.K. Teo, EXAFS: Basic Principles and Data Analysis (Springer-Verlag, Berlin (1986).
103. P. Lee and M.B. Comisarow, Appl. Spectrosc. **43**, 599-604 (1989).
104. A. Kuzmin, EXAFS Data Analysis Software Package, Version 5.1 (1999).